Master of Science Thesis

On the turbulent drag reduction of a dimpled surface under a pressure gradient

Y.H.J. van Weersch

November 8, 2017

Aerodynamics

Faculty of Aerospace Engineering

TU Delft

Delft University of Technology

On the turbulent drag reduction of a dimpled surface under a pressure gradient

Master of Science Thesis

For obtaining the degree of Master of Science in Aerospace Engineering
at Delft University of Technology

Y.H.J. van Weersch

November 8, 2017

Faculty of Aerospace Engineering · Delft University of Technology

Delft University of Technology

DELFT UNIVERSITY OF TECHNOLOGY
DEPARTMENT OF AERODYNAMICS

The undersigned hereby certify that they have read and recommend to the Faculty of Aerospace Engineering for acceptance the thesis entitled **"On the turbulent drag reduction of a dimpled surface under a pressure gradient"** by **Y.H.J. van Weersch** in fulfillment of the requirements for the degree of **Master of Science**.

Dated: November 8, 2017

Supervisors:

dr.ir. B.W. van Oudheusden

dr.ir. F.J.J. Schrijer

prof.dr.ir. L.L.M. Veldhuis

Reader:

dr. S.J. Hulshoff

Acknowledgements

This thesis marks the apotheosis of six years of studying aerospace engineering and the end of eleven months of laborious effort on the subject of turbulent drag reduction. Turbulence remains one of the biggest unresolved problems in physics, but it has not stopped people in attempts to control it. It was a great challenge to take part in it and I sincerely hope my work is useful for the many soldiers that will take on the behemoth of turbulence in their future strives.

I would especially like to thank the lab technicians of the aerodynamics department, Peter Duyndam, Dennis Bruikman, Frits Donker Duyvis, Stefan Bernardy and Nico van Beek, for their extensive practical knowledge (and comical relief) in helping me to perform my experiments. I would also like to thank my supervisors Bas van Oudheusden, Ferry Schrijer and Leo Veldhuis, leviathans of aerodynamics, for their suggestions and our discussions on performing experiments. As a basement denizen I was lucky to be around people with interesting backgrounds and great sense of humor. I will miss the many jokes shared with Qais, Sumit, Roberto, Lluis, Werner, Sumedh with an H, Jordi, Arti, Ka Hin, Arun, Jaydeep, and many others. I wish you great fortune in the future. I can of course not forget to name the awesome guys of the Geerstreet gang at the homefront in Heerlen, including Nils, Benedikt, Tom, Guus, Timothy, Dirk, Tim, Kevin, Heinz, and Max, who helped me discharge during the weekends.

For the end, I would like to return to the beginning. I performed my first year in aerospace engineering in the Dutch-speaking segment, and on a more personal note I would like to return to my own language.

Door de jaren heen heb ik het geluk gehad dat ik omringd ben door mijn beste vrienden Jean-Paul van Bommel, Nick Voogt, Lorenzo Vlieks en Mark Frank die er in goede en slechte tijden waren, met wie ik veel onvergetelijke verhalen deel en, ongetwijfeld, nog ga meemaken. Maar er zijn twee personen die ik het meest dankbaar ben, en dat zijn mijn lieve ouders, *Jos* en *Anja*. Ik bedank mijn lieve moeder, die voor mij bijna iedere zondag vroeg opstond om voor de komende week eten te koken, en altijd de lekkerste dingen in huis haalde als ik terugkwam uit Delft. Ik bedank mijn lieve vader, die mij altijd trouw van station Heerlen kwam halen naar de warme plek die ik mijn thuis mag noemen en, uiteraard, voor de vele ritjes naar Klimmen. Ik had niets beters kunnen wensen dan jullie.

And now my watch has ended.

Abstract

Dimples are spherical indentations applied at a surface that have been shown in previous experimental investigations to yield a drag reduction within a turbulent boundary layer. Dimpled surfaces have inherent advantages over traditional flow control techniques like oscillating walls, that require heavy active systems to be installed, and riblets that have proven effective in real-flight conditions but pose maintenance problems. Potentially drag-reducing dimples on the other hand do not require heavy actuating systems and are not restrictive on maintenance as they are shallow and thus less prone to deterioration. The aforementioned traditional flow control techniques show changes to their turbulent properties, like a reduced Reynolds shear stress, reduced turbulent intensity and an upwards shift of the logarithmic layer leading to a lower skin-friction coefficient. Dimpled surfaces will encounter varying pressure gradients in applications like airfoils, and thus the effect of both a favorable and adverse pressure gradient is explored.

An experimental investigation is performed in which the effect of the pressure gradient and the Reynolds number is investigated on the drag-reducing potential of a dimpled surface. A novel experimental set-up is devised in which the pressure gradient is adjusted by means of a planar diffuser top wall which allows the flow to accelerate or decelerate. A newly-designed drag balance which makes us of flexible flexures is used along with a load cell to quantify the drag of the total test plate surface directly in a direct force measurement campaign. To investigate if the drag reduction is attained by manipulation of the turbulent properties, use is made of the particle image velocimetry technique and the hot-wire anemometry technique. With these techniques the turbulent boundary layer is quantified at an upstream and downstream location between two dimples to check for the same changes in turbulent properties as have been observed for drag-reduced turbulent boundary layers.

After confirming a good repeatability of the drag balance, a drag reduction is observed from the direct force measurements for the dimpled surface in the zero pressure gradient configuration. In correspondence with previous drag-reducing dimples a preliminary drag increase is observed followed up by an increasing drag reduction with increasing Reynolds number, yielding a drag reduction of 0.8% at the maximum considered Reynolds number. This drag reduction is however not observed from investigation of the boundary layer properties, as no considerable changes are observed in the turbulent properties. For the favorable pressure gradient a drag reduction is observed from the upwards shift of the logarithmic layer, reduction in turbulence intensity and Reynolds shear stress. This drag reduction is also found from the DFM campaign, however with a large data spread and no confirmed repeatability in the favorable pressure gradient configuration. The increase in laminarization parameter K and the absence of a clear logarithmic layer shift for the ZPG case point into the direction of a beneficial effect of the dimple on relaminarization properties. Finally, the adverse pressure gradient case showed an increase in both Reynolds shear stress and turbulence intensity. No upwards shift is detected in the boundary layer profile. It must be noted that the smaller amount of measurement points due to the growth of the wake region lead to reduced fitting accuracy. From the DFM campaign a drag reduction was observed for the adverse pressure gradient cases, but no repeatability is confirmed and an unconventional force distribution is observed with increasing Reynolds number.

Contents

List of Figures

List of Tables

List of Symbols

Abbreviations

APG	Adverse Pressure Gradient
CTA	Constant Temperature Anemometry
DFM	Direct Force Measurements
DNS	Direct Numerical Simulation
FBD	Free Body Diagram
FPG	Favorable Pressure Gradient
HWA	Hot-Wire Anemometry
MAPG	Mild Adverse Pressure Gradient
MFPG	Mild Favorable Pressure Gradient
OJF	Open Jet Facility
PIV	Particle Image Velocimetry
RMS	Root-mean-square
RMSE	Root-mean-square error
SAPG	Strong Adverse Pressure Gradient
SFPG	Strong Favorable Pressure Gradient
TBL	Turbulent boundary layer
ZPG	Zero Pressure Gradient

Latin symbols

a	Overheat ratio	$[-]$
b_f	Flexure width	$[m]$
c	Chord length	$[m]$
d	Dimple depth	$[m]$
d	diameter	$[m]$
d_o	Distance from lense to FOV	$[m]$
e_{th}	Thermal energy	$[J]$
f	Frequency	$[Hz]$
f_{nat}	Natural frequency	$[Hz]$
i	Occurrence	$[-]$
k	Stiffness	$[N/m]$
m	Mass	$[kg]$
p	Pressure	$[N/m^2]$
q	Dynamic pressure	$[N/m^2]$
r	Dimple edge curvature radius	$[m]$
s_1	Upstream flexure distance	$[m]$
s_2	Downstream flexure distance	$[m]$
t	Welch's t-statistic	$[-]$
t_f	Flexure thickness	$[m]$
u, v	Velocity in streamwise and wall-normal direction	$[m/s]$
u', v'	Instantaneous velocity fluctuation	$[m/s]$

u^*	Friction velocity	$[m/s]$
u^+	Streamwise velocity divided by friction velocity	$[-]$
u_{rms}, v_{rms}	Root-mean square velocity	$[m/s]$
x, y	Coordinate in streamwise and wall-normal direction	$[m]$
y^+	Dimensionless wall-normal coordinate	$[-]$
y_t	Integration limit for skin-friction integration	$[m]$
A_{exp}	Exposure area	$[m^2]$
B	Turbulent wall law intercept constant	$[-]$
C_D	Drag coefficient	$[-]$
C_f	Skin-friction coefficient	$[-]$
C_l	2D lift coefficient	$[-]$
C_p	Pressure coefficient	$[-]$
D	Dimple diameter	$[N]$
E	Young's modulus	$[N/m^2]$
E	Voltage	$[V]$
F	Force	$[N]$
F_D	Effective drag force	$[N]$
H	Boundary layer shape factor	$[-]$
H_1	Heads entrainment parameter	$[-]$
I	Electrical current	$[A]$
I_z	Moment of inertia	$[m^4]$
K	Acceleration/relaminarization parameter	$[-]$
K	Buckling coefficient	$[-]$
L_f	Flexure length	$[m]$
L_x	Streamwise spacing	$[m]$
L_z	Spanwise spacing	$[m]$
N	Number of samples	$[-]$
Nu	Nusselt number	$[-]$
P	Probability	$[-]$
R	Electrical resistance	$[\Omega]$
R	Resolution	$[px/m]$
Re_c	Chord-based Reynolds number	$[-]$
Re_D	Dimple-based Reynolds number	$[-]$
S	Surface area	$[m^2]$
T	Temperature	$[°C]$
U_∞	Upstream velocity	$[m/s]$
U_e	Freestream velocity	$[m/s]$

Greek symbols

α	Thermal expansion coefficient	$[K^{-1}]$
δ_{99}	Boundary layer thickness at u(y) = 0.99U_e	$[m]$
δ^*	Displacement thickness	$[m]$
ϵ	Uncertainty	$[-]$
η	Flexure efficiency	$[-]$
θ	Momentum thickness	$[m]$
κ	Kármán constant	$[-]$
μ	Dynamic viscosity	$[kg \cdot m^{-1}s^{-1}]$
ν	Kinematic viscosity	$[m^2/s]$

ρ	Density	$[\mathrm{kg/m^3}]$
σ	Sample variance	$[-]$
τ_w	Wall shear stress	$[\mathrm{N/m^2}]$
φ	Planar diffuser angle	$[^\circ]$
Δ	Difference	$[-]$
$\Delta\mathrm{B}$	Wall intercept change	$[-]$
$\Delta\mathrm{C_D}$	Drag coefficient difference relative to flat plate	$[-]$
$\Delta\mathrm{C_f}$	Skin-friction drag difference relative to flat plate	$[-]$
$\Delta\mathrm{P}$	Probability difference	$[-]$

Chapter 1

Introduction

When an object traverses through a fluid a thin boundary layer is created between the object surface and the freestream. When the upstream Reynolds number becomes high enough the laminar boundary layer is supplanted by a turbulent boundary layer in which the skin-friction is higher due to mass and momentum mixing by chaotic swirls or eddies. When the Reynolds number becomes significantly high enough, as occurs in typical real-life applications, it becomes increasingly hard to prevent the advent of a turbulent boundary layer. Looking at the aerospace engineering industry in more detail, it is described by Fischer and Ash (1974) that the drag envelope of an aircraft consists 45% out of skin-friction drag, 35% for a supersonic aircraft and 25% for a hypersonic aircraft. The skin-friction is thus a profound contribution to the overall drag coefficient. The drag coefficient of an object is directly related to the amount of energy required to propel it forward. In real-life application this energy is supplied by means of propellant of varying chemical compositions, that in turn engender further weight and performance penalties on the object that needs to be propelled. Other than these design properties that are affected, the purchase of propellant needs to be accounted for and is an important expense for industry.

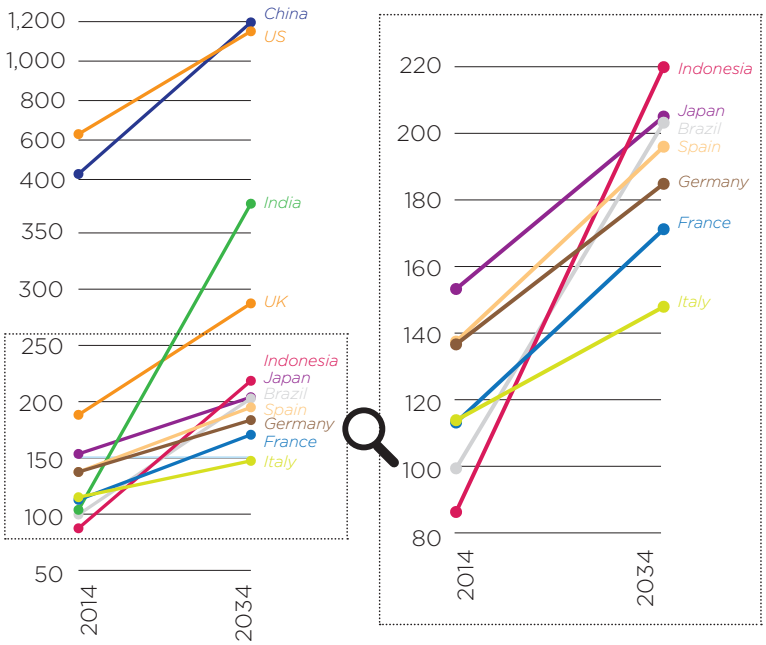

FIGURE 1.1: Expected rise in passenger numbers between 2014 and 2034 by the International Air Transport Association (2016).

In their annual report, the International Air Transport Association (IATA) predicts a significant increase in passenger numbers between 2014 to 2034. Markets in Asia are rapidly emerging, but traditional markets like Europe and the United States are also still growing.

With increasing passenger numbers airliners are obliged to buy new airplanes to ferry all these passengers. With increasing numbers of airplanes there is also an increase in fuel cost. It is reported by International Air Transport Association (2016) that in 2015 fuel costs consisted on average 27% of an airliners budget: a significant portion. Even a 1% decrease of fuel costs could save hundreds of millions of dollars throughout the airliner industry. Reductions in drag could yield significant savings in the airliner industry, but the applications of drag reduction can also be utilized for cars, boats and stationary objects like pipelines.

There is quite some diversity in the mechanisms for flow control of the boundary layer that are used in an attempt to decrease the skin-friction drag. The drag-reducing effect of riblets is well documented, and oscillating walls and compliant coatings have also led to skin-friction reductions in direct numerical simulations and experimental studies. They are however not applied throughout the industry and often troubled by logistical problems. For example, an aircraft fitted with riblets was described by Szodruch (1991) to yield a 2% drag reduction for an Airbus A320 fitted for 70% with riblets, but operators noted dirt contamination of the riblets annulling their effect and riblets simply falling off, but also reported that riblets hinder the application of paint schemes to the aircraft [Spalart and McLean (2011)]. A possible solution that does not require excessive surface alteration is the *dimpled surface*.

1.1 History of dimples

Dimples are spheroids subtracted from a flat surface area, indentations of varying geometrical parameters that are used in attempts to reduce the turbulent skin-friction drag. A golf ball comes to mind when discussing spherical surface indentations. The mechanism is however different. The dimples on a golf ball triggers the transition of a laminar to a turbulent boundary layer at the cost of *increased* skin-friction, but a decrease of the pressure drag due to a smaller wake leading to an overall drag reduction. The dimple that is discussed in this study is however used to *decrease* the skin-friction drag of a boundary layer that is already fully turbulent.

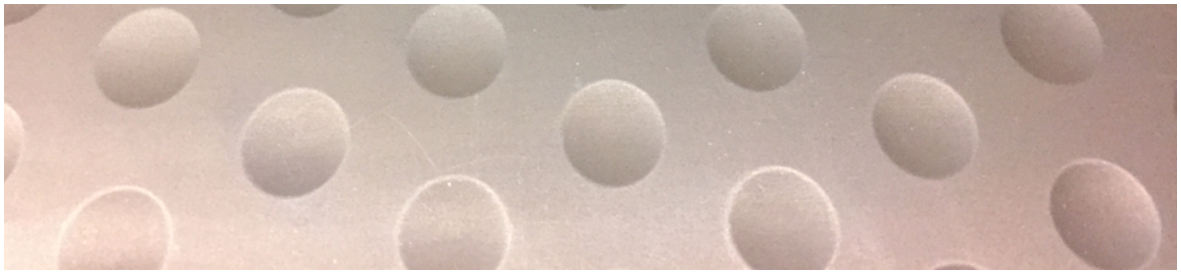

FIGURE 1.2: A dimpled surface.

The drag-reducing effect has been first described by Kiknadze et al. (1984), who found a drag-reducing effect of a dimple in a heat exchanger in a nuclear reactor in the Soviet Union. Since then research has been performed all over the world, with several institutions pushing the subject more than others. Drag reductions by dimpled surfaces have been investigated scrupulously by the National University of Singapore (NUS) by Tay et al. (2015) and at Delft University of Technology (DUT) by Vervoort (2007), Van Nesselrooij (2015) and Van Campenhout (2016). At DUT Van Nesselrooij (2015) a drag reduction was observed of up to 4% for a dimple configuration together with an increasing drag reduction trend with increasing Reynolds number. To study this Reynolds number trend further Van Campenhout (2016) increased the effective upstream velocity by adding a ramp to converge the test section and

achieve higher velocties. Van Campenhout (2016) was however unsuccessful in finding a drag reduction like Van Nesselrooij (2015) but did quantify the existence of a surface oscillation. This wave is proposed by both Tay et al. (2015) and Van Campenhout (2016) to be the drag-reducing mechanism, analogous to the oscillating wall. Whereas the existence of a wave is proven, it is still unknown how the drag reduction is in fact achieved. If it is caused by affecting turbulent coherent structures close to the surface of the wave it is of paramount interest to research this region with more effort. Previous investigations have also only considered channel flows and zero pressure gradient configuration of a dimpled surface. As aircraft (and cars, boats, etc.) have large surface areas subjected to both adverse and favorable pressure gradients during cruise, it is also wanted to inquire if a possible drag-reducing effect is also present on a dimpled surface subjected to varying pressure gradients.

1.2 Research aim

The aforementioned leads to the formulation of the following two main research questions:

- How is the skin-friction reduction in a dimpled surface affected by the pressure gradient and the Reynolds number?
- Does a dimpled surface cause a skin friction reduction by a change in the turbulent properties?

These two research questions are combined in the research objective, that is *to better understand the skin friction drag-reducing mechanism of a dimpled plate against a flat plate for a ZPG, FPG and APG for varying Reynolds numbers by quantifying the turbulent boundary layer in the near-wall region on a dimpled plate between two dimples by means of particle image velocimetry (PIV) and hot-wire anemometry (HWA) measurements and performing direct force measurements (DFM).*

This objective can be split into the following sub-objectives:

Design a novel set-up to perform measurements In order to perform measurements a new set-up is required that can change the tunnel geometry to induce a pressure gradient.

Quantify the turbulent boundary layer in the near-wall region The literature points to the near-wall region for the drag reduction. It is thus required to examine and quantify the turbulent statistics near the wall.

Measure the skin friction reduction over the entire test plate Whereas the near-wall region is a detail of the flow field, measurements in which the effect of the entire geometry is studied will give a total view of the drag reduction.

Explore the effects of both an adverse and favourable pressure gradient The pressure gradient is proposed to have an effect on the drag reduction and thus its effect needs to be examined in detail.

Quantify the effect of the Reynolds number Due to the increasing drag reduction observed in previous experiments, the effect of the Reynolds number on the flow needs further research.

1.3 Outline

This thesis attempts to increase to contribute to the existing knowledge on turbulent drag reductions by a dimpled plate. This report will first present a state of the art on the current knowledge on turbulent boundary layers, the structure within it and current flow control methods (including dimples) attempted to influence it in Chapter 2. Special focus is provided for how the turbulent boundary layer behaves when subjected to a pressure gradient. This study investigates the effect of a dimple on the turbulent drag of a surface both in a total sense, as well as a local sense. The different measurement techniques used for these purposes are described in Chapter 3 for the total drag quantification and particle image velocimetry and hot-wire anemometry for the flow quantification, together with a description of the novel experimental set-up. The results of all three measurement techniques are given in Chapter 4 to assess the effect of the dimple on the drag properties under varying Reynolds number and pressure gradient configurations. Finally the conclusion on the results and recommendations for further research are presented in Chapter 5.

Chapter 2

Theoretical background

In this chapter a short literature survey is presented into the subjects of boundary layer theory, existing drag-reducing mechanisms, and the previous numerical and experimental investigation into the dimpled surfaces.

2.1 Turbulent boundary layers

The fundamentals of boundary layer theory are presented first next to the current state-of-the-art in respect to the structure of a turbulent boundary layer. First a general description of the boundary layer terminology is given in Section 2.1.1, while Section 2.1.2 focuses on the boundary layer terminology. Finally the important turbulent coherent structures and the effect of a pressure gradient are described in Section 2.1.3.

2.1.1 Boundary layer terminology

In this section the general boundary layer terminology is explained by the use of the schematic boundary layer profile in Figure 2.1.

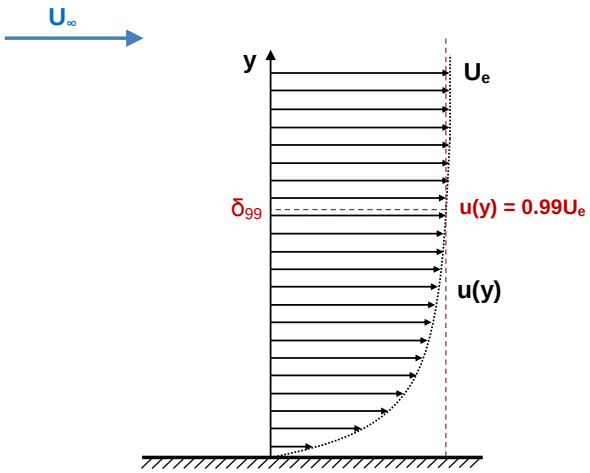

FIGURE 2.1: Schematic boundary layer.

In Figure 2.1 U_∞ is defined as the upstream inlet velocity, whereas U_e is the local freestream velocity. The boundary layer thickness δ_{99} is defined as the wall-normal coordinate where the streamwise velocity is 99% of the freestream velocity U_e at the very top of the boundary layer at that specific location.

$$\delta_{99} = y_{u/U_e=0.99} \tag{2.1}$$

There exist different length scales other than δ_{99} for which the boundary layer can be analyzed and they are conveniently listed by White (2006). The displacement thickness δ^* is the

wall-normal translation that a surface has to move to yield a solution equal to the inviscid solution. The displacement thickness is defined by Equation 2.2.

$$\delta^* = \int_0^\infty \left(1 - \frac{u}{U_e}\right) \mathrm{d}y \tag{2.2}$$

The distance with which the boundary layer has to be displaced parallel to itself to account for the reduction in momentum is called the momentum thickness θ, and is defined by Equation 2.3.

$$\theta = \int_0^\infty \frac{u}{U_e}\left(1 - \frac{u}{U_e}\right) \mathrm{d}y \tag{2.3}$$

The ratio between the displacement thickness and the momentum thickness is called the shape factor H. It is given by Equation 2.4.

$$H = \frac{\delta^*}{\theta} \tag{2.4}$$

The shape factor is a measure of the 'fullness' of the boundary layer. Boundary layers nearing separation (with an 'empty' velocity profile) will have higher shape factors than boundary layers that are not (and thus have 'full' velocity profiles). The laminar boundary layer has a shape factor of 2.59, while turbulent (ZPG) boundary layers have shape factors around 1.3 as reported by Pope (2000).

Another non-dimensional parameter is the skin-friction coefficient. The friction velocity u^* is measure of the wall shear stress τ_w at the wall location:

$$C_f = \frac{\tau_w}{\frac{1}{2}\rho U_\infty^2} \tag{2.5}$$

where the wall shear stress is defined with the velocity gradient at the wall location:

$$\tau_w = \mu \left.\frac{\partial u}{\partial y}\right|_{y=0} \tag{2.6}$$

From this it is possible a define a useful quantity called the friction velocity u^*:

$$u_\tau = \sqrt{\frac{\tau_w}{\rho}} = U_e\sqrt{\frac{C_f}{2}} \tag{2.7}$$

The relation between the different length scales inside the boundary layer was combined into the integral relation by Von Karman [White (2006)]. This integral relation (Equation 2.8) is not a fundamental relation but a useful correlation tool to assess boundary layer growth.

$$\frac{C_f}{2} = \frac{\tau_w}{\rho U^2} = \frac{\mathrm{d}\theta}{\mathrm{d}x} + (2+H)\frac{\theta}{U_e}\frac{\mathrm{d}U_e}{\mathrm{d}x} \tag{2.8}$$

For a ZPG ($\mathrm{dU_e/\,dx} = 0$) the skin-friction coefficient is reduced to the spatial derivative of the momentum thickness. When the boundary layer is subjected to a pressure gradient ($\mathrm{dU_e/\,dx} \neq 0$) it can be observed from Equation 2.8 that the skin-friction no longer is dependent on only just the spatial distribution of momentum thickness. Head (1960) combined additional empiric relations to allow for the computation of the boundary layer when an external velocity is applied. Next to Equation 2.8 the additional empiric entrainment relation were

defined:

$$\frac{E}{u_e} = \frac{\mathrm{d}}{\mathrm{d}x}\left(u_e \theta H_1\right) = 0.0306\left(H_1 - 3\right)^{-0.6169} \tag{2.9}$$

$$\frac{\mathrm{d}H_1}{\mathrm{d}x} = -H_1\left(\frac{1}{u_e}\frac{\mathrm{d}u_e}{\mathrm{d}x} + \frac{1}{\theta}\frac{\mathrm{d}\theta}{\mathrm{d}x}\right) + \frac{0.0306}{\theta}\left(H_1 - 3\right)^{-0.6169} \tag{2.10}$$

$$H_1 = \begin{cases} 3.3 + 0.8234(H - 1.1)^{-1.287}, & H < 1.6 \\ 3.3 + 1.5501(H - 0.6778)^{-3.064}, & H > 1.6 \end{cases}$$

$$H_1 = \frac{\delta_{99} - \delta^*}{\theta} \tag{2.11}$$

The correlation of Ludwieg and Tillmann (1949) is used as a relation to determine the skin-friction coefficient:

$$C_f = 0.246 \cdot 10^{-0.678H} \mathrm{Re}_\theta^{-0.268} \tag{2.12}$$

These additional closure relations can be numerically implemented to compute the boundary layer development for an accelerating or decelerating flow. To compute the pressure coefficient for an inviscid flow can be expressed as a direct relation between the local freestream velocity and the upstream inlet velocity.

$$C_p(x) = \frac{p(x) - p_\infty}{\frac{1}{2}\rho U_\infty^2} = 1 - \left[\frac{U_e(x)}{U_\infty}\right]^2 \tag{2.13}$$

2.1.2 Turbulent boundary layer theory

In a turbulent boundary layer the flow is unsteady and chaotic, and many swirls or eddies can be observed. To describe the turbulent boundary layer the velocity can be decomposed into a mean velocity and its instantaneous fluctuation:

$$u = \overline{u} + u' \qquad\qquad v = \overline{v} + v' \tag{2.14}$$

The shear stress for the turbulent boundary layer τ is defined by Equation 2.15.

$$\tau = -\rho\overline{u'v'} + \mu\frac{\partial \overline{u}}{\partial y} \tag{2.15}$$

In Equation 2.15 a new term arises due to the turbulent nature of the boundary layer. The term $\rho\overline{\mathrm{u'v'}}$ is referred to as the *Reynolds shear stress*. Due to the no-slip condition the velocity at the wall location is zero-valued, and as a result the instantaneous velocity fluctuation as well. The wall shear stress τ_w for a turbulent flow can then be described purely by the viscous stress:

$$\tau_\mathrm{w} \equiv \tau(y = 0) = \mu \left.\frac{\partial \overline{u}}{\partial y}\right|_{y=0} \tag{2.16}$$

White (2006) describes that the mean velocity and its coordinate can be non-dimensionalized into *wall-units* by the friction velocity u^* and the kinematic viscosity ν:

$$y^+ = \frac{y u_\tau}{\nu} \qquad\qquad u^+ = \frac{\overline{u}}{u_\tau} \tag{2.17}$$

Based on the wall units three distinct regions can be observed inside the TBL. The *viscous sublayer* ($\mathrm{y}^+ < 5$) in which the linear relation $\mathrm{y}^+ = \mathrm{u}^+$ holds, the *buffer layer* ($5 < \mathrm{y}^+ < 30$) and the *overlap layer* ($30 < \mathrm{y}^+ < 350$), see Figure 2.2.

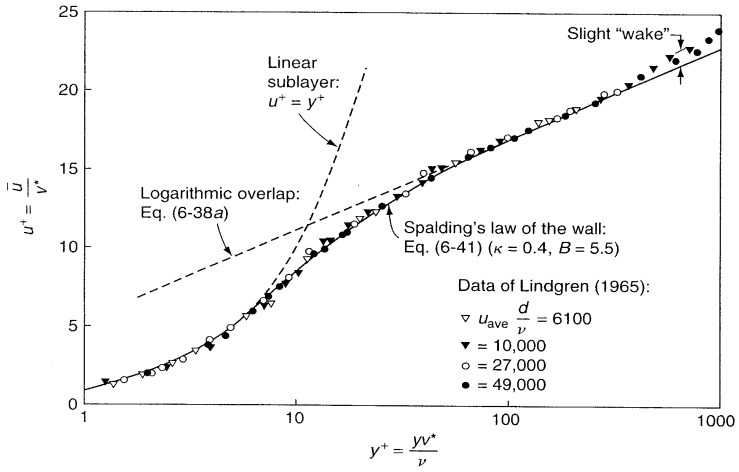

FIGURE 2.2: The non-dimensionalized turbulent boundary layer containing the viscous sublayer, buffer layer, logarithmic layer and wake component compiled by White (2006).

The overlap layer is a straight line when plotted on a logarithmic axis, and thus it is also referred to as the *logarithmic layer*. The logarithmic layer can be described with Equation 2.18:

$$u^+ = \frac{1}{\kappa} \ln y^+ + B \tag{2.18}$$

Spalding (1961) unified these three layers into a single implicit expression:

$$y^+ = u^+ + e^{-\kappa B}\left[e^{\kappa u^+} - 1 - \kappa u^+ - \frac{(\kappa u^+)^2}{2} - \frac{(\kappa u^+)^3}{6}\right] \tag{2.19}$$

for which the near-universal constants $\kappa \approx 0.41$ and B ≈ 5.0 are used. Since the skin-friction coefficient is captured in Spalding's Law of the Wall, it is possible to fit an experimental velocity profile to the Law of the Wall, the so-called *Clauser method*. Klebanoff (1955) examined turbulence intensities of the turbulent boundary layer by investigating the root-mean-square velocity of the streamwise-, spanwise- and wall-normal velocities. Klebanoff (1955) observed that close to the wall ($y/\delta < 0.01$) a turbulence intensity peak exists, with values as high as 10% of the freestream velocity (see Figure 2.3).

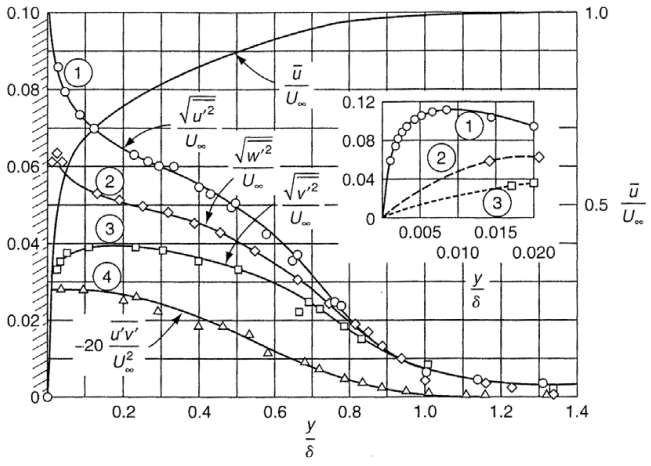

FIGURE 2.3: Root-mean-square velocity fluctuations and mean turbulent velocity profile by Klebanoff (1955).

It is furthermore observed that the wall-normal fluctuation is extra damped near the wall and has its peak at ($y/\delta \approx 0.2$). The streamwise and wall-normal velocity fluctuations together form the Reynolds stress (see Equation 2.15).

2.1.3 Turbulent coherent structures

In an attempt to seek order within apparent chaos and explain phenomena observed in the turbulent boundary layer, since 1960 efforts have increased to dissect the turbulent wall-bounded flows into elementary coherent structures [Pope (2000)]. In this section a review of several of these coherent structures is given.

Sweeps and ejections. Kline et al. (1967) performed the one of the first flow visualizations in a water channel flow where they detected the presence of near-wall ($y^+ < 10$) low-speed streaks and their subsequent lift-up, oscillation and *bursting*. They named this uplifting and violent break-up of the streak *ejection*, and proposed this to be one of the sources of near-wall turbulent production. These streaks are observed near quasi-streamwise vortices, and opposing the upwards movement there is also a corresponding downward impingement of fluid towards the wall, which is referred to as *sweep* by Corino and Brodkey (1969). Kasagi and Fukagata (2006) describe these impingement regions as high regions of turbulence production and contributions to the Reynolds stress, and propose that suppression of these events should be the primary objective of skin-friction drag control.

Wallace (2016) describes quadrant analysis as a useful tool in the detection of these sweep and ejection events, which sorts the instantaneous fluctuations along the instantaneous fluctuation axes (see Figure 2.4).

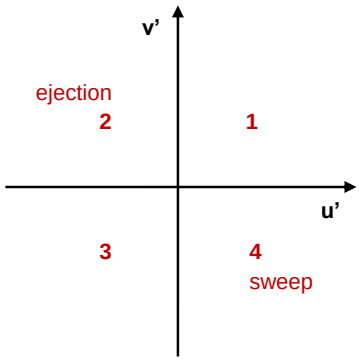

FIGURE 2.4: Quadrant definition for the instantaneous velocity fluctuations.

Ejections are identified as Q2 events (u′ < 0, v′ > 0) and sweep events as Q4 events (u′ > 0, v′ < 0). To quantify the contribution of the Reynolds stress to the turbulent skin-friction, Mehdi et al. (2014) performed a threefold integration on the Reynolds-averaged Navier-Stokes equation similar as Fukagata et al. (2002) did. In this expression the skin-friction coefficient is determined up to a height y_t inside the turbulent boundary layer, such that the skin-friction coefficient can be compared also if the boundary layer thickness is unknown or if the boundary layer is not fully captured with flow measurement techniques.

$$C_f = \frac{4\nu}{y_t^2 U_\infty^2}\int_0^{y_t} \overline{u}\,\mathrm{d}y - \frac{4}{y_t^2 U_\infty^2}\int_0^{y_t} (y_t - y)\overline{u'v'}\,\mathrm{d}y - \frac{2}{y_t^2 U_\infty^2}\int_0^{y_t} (y_t - y)^2 \frac{\partial \tau/\rho}{\partial y}\,\mathrm{d}y \tag{2.20}$$

Equation 2.20 shows that negative quadrant contributions close to the wall of Q2 and Q4 relatively lead to the largest skin-friction contributions.

Quasi-streamwise vortices. Bakewell and Lumley (1967) identified pairs of counter-rotating vortices in the the near-wall region ($y^+ < 100$) and found that they were slightly tilted from the streamwise direction and are therefore referred to as *quasi-streamwise vortices*. Dennis (2015) describes the symbiosis between low-speed and high-speed (see Figure 2.5) streaks existing between the counter-rotating vortices and that there is no consensus if the counter-rotating vortices cause the low-speed streaks or vice-versa.

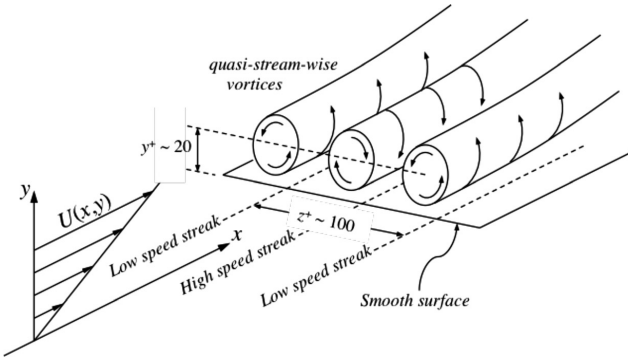

FIGURE 2.5: Schematic view of the near-wall turbulent structures inside the buffer layer [Perlin et al. (2016)].

Kasagi and Fukagata (2006) describe that sweep and ejections are inherently connected to these quasi-streamwise vortices, where the vortex motion of the quasi-streamwise vortex impinges flow downwards to the wall and moves flow upwards in an ejection event.

Hairpin vortices. Theodorsen (1951) was the first to propose a vortical structure model inside the turbulent boundary layer of a 'horseshoe' vortex. In this model the heads of the vortex are inclined downstream at 45° creating a symmetric arch vortex. Head and Bandyopadhyay (1981) investigated the zero pressure gradient turbulent boundary layer and found arch-type vortical structures inclined at angles to the wall of 40° to 50°. For larger Reynolds numbers they found that the arch-type vortices were thinner and protruded through a large part of the boundary layer, naming them *hairpin* vortices instead of horseshoe vortices. They introduced the notion that as a hairpin leaves the surface, it leaves favorable conditions for the creation of a new hairpin vortex.

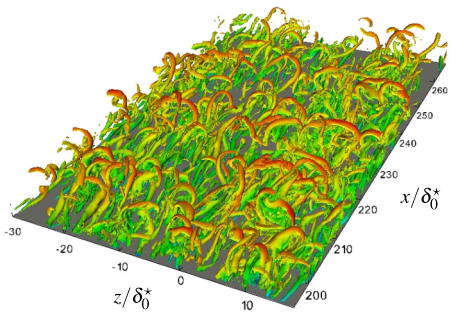

FIGURE 2.6: Visualized 'hairpin forest' for Re_θ = 370-445 by Eitel-Amor et al. (2015).

These hairpin vortical structures have been observed in both DNS studies [Eitel-Amor et al. (2015)] as well as experimental studies [Elsinga et al. (2007)]. Adrian et al. (2000) found that the boundary layer is densely populated by hairpin vortices and different deformations ('cane', 'horseshoe', 'omega'-shaped) in 'packets'. They pose that the hairpin packets originate from near the wall from a disturbance that creates an area of low momentum at the wall, which is induced between the legs.

Effect of pressure gradient. Investigations into coherent turbulent motion in a turbulent boundary layer subjected to a pressure gradient have primarily focused on low Reynolds number DNS studies and experimental studies using hot-wire probes.

Krogstad and Skare (1995) performed an experimental analysis of a turbulent boundary layer under a strong adverse pressure gradient and reported that the Q2 motions are diminished near the wall while the Q1 and Q4 motions are strongly increased. The same decrease in Q2 motions in the near-wall region is also reported by Drozdz and Elsner (2011) and Lee and Sung (2009). The latter furthermore describe that under an adverse pressure gradient turbulent production is moved to higher layers in the boundary layer, and by larger angle inclinations of the hairpin vortex packets. The result of this is that near the wall ($y^+ < 50$) the vortical activity is decreased, as is observed in Figure 2.7. This decrease in vortical activity is also found by Maciel et al. (2017) in a large defect turbulent boundary layer subjected to a strong pressure gradient.

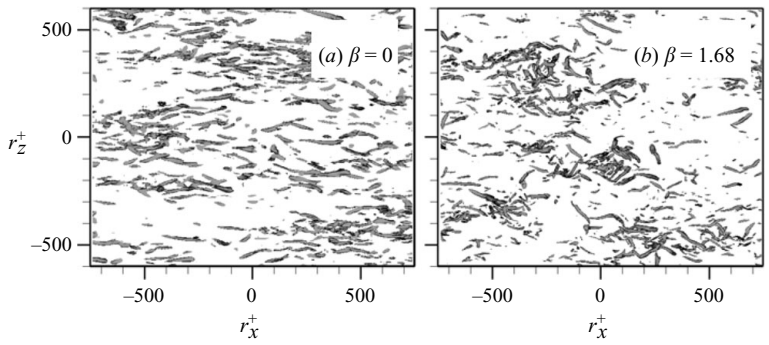

FIGURE 2.7: Decrease of vortical structures in the near wall region ($y^+ < 50$) observed by Lee and Sung (2009) when an APG is applied.

The investigation into the effect of both an adverse and favorable pressure gradient is combined in the experimental investigation of Dróżdż and Uruba (2014). They investigated a turbulent boundary layer at several stations inside a converging-diverging channel where a favorable pressure gradient induced by the converging part is followed up by an adverse pressure gradient in the expanding part. They found that the absolute magnitude of the turbulent intensity peak in Figure 2.8 is increased for a favorable pressure gradient while it is decreased for an adverse pressure gradient, followed up by the advent of a second peak at a higher location (as was also reported by Lee and Sung (2009)).

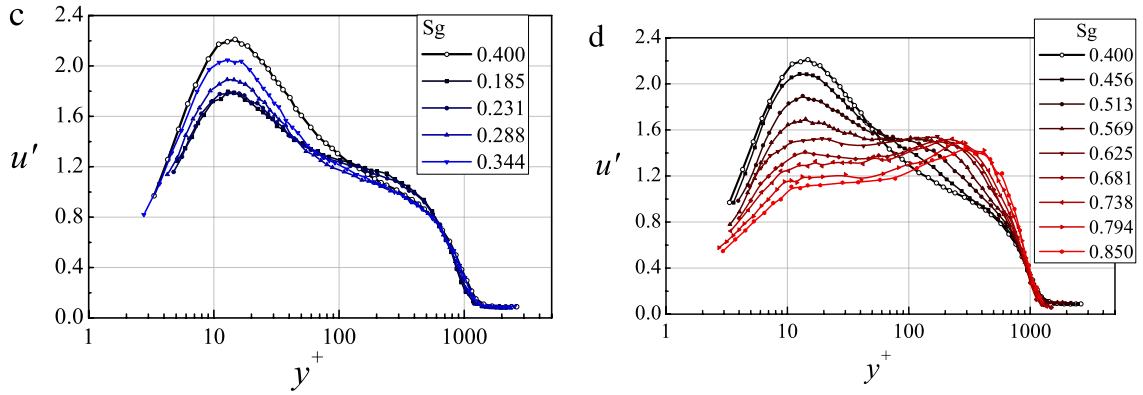

(A) FPG (B) APG

FIGURE 2.8: Turbulent fluctuations for a converging-diverging channel by Drozdz et al. (2015) versus the corresponding dimensionless distance Sg = x_s/L, where L is the length of the test section (L = 1067 mm). Sg < 0.4 indicates the converging part of the set-up, whereas Sg > 0.4 indicates the diverging part.

It was found by Narasimha and Sreenivasan (1973) that under a favorable pressure gradient the turbulent boundary layer may reset into a quasi-laminar state, in a so-called *relaminarization*. They found that if in sufficiently large favorable pressure gradients the acceleration parameter K (Equation 2.21) rises to 3.5×10^{-6} and above, turbulent activity starts to freeze in the boundary layer. Mukund et al. (2006) found that the logarithmic layer is shifted upwards during relaminarization. They describe three stages in the relaminarization effort: an initial stage in which the flow is subjected to a favorable pressure gradient (with a resulting increase of C_f and decrease of H), a second relaminarizing stage where the law of the wall breaks down and a third and final stage where H increases and C_f decreases towards laminar values.

$$K = \frac{\nu}{U_e^2(x)} \frac{\mathrm{d}U_e(x)}{\mathrm{d}x} \tag{2.21}$$

The onset of relaminarization is not found to appear instantly by Sreenivasan (1981), but progresses when the boundary layer is sustained under such a favorable pressure gradient long enough for a large enough K.

2.2 Turbulent drag-reduction methods

Next to dimpled surfaces, there methods have been methods devised to reduce the skin-friction in a turbulent boundary layer. Among these are the riblet surface and the oscillating wall. In this section a concise overview of the methods is given and how the flow control leads to a drag reduction.

2.2.1 Logarithmic layer shift

In early flow measurement techniques the two-dimensional properties of a turbulent boundary layer are often not captured, such that the Reynolds shear stress can not be determined. The skin-friction integration technique defined by Fukagata et al. (2002) and expanded upon by Mehdi et al. (2014) is thus not applicable. An often used method in determining C_f is by measuring the logarithmic part of the turbulent boundary layer. The Clauser method is often used, in which the logarithmic part of the boundary layer is fitted to the expression of the turbulent boundary layer by Spalding (1961).

The turbulent boundary layer is affected by the application of a drag-reducing mechanism, and the expression with the standard wall-intercept B is no longer valid. For wall roughness it is reported by White (2006) that the viscous sublayer breaks up, with a downwards shift of the logarithmic layer with a resulting skin-friction increase. Gatti (2016) devised an expression in which the reduction of the skin-friction by a shift in the logarithmic layer was explicitly shown. In this expression the defect law of Equation 2.22 and the law of the wall of Equation 2.18 are combined by Gatti (2016) yielding Equation 2.23.

$$U_c^+ - u^+ = -\frac{1}{\kappa}\ln\left(\frac{y}{h}\right) + B_1 \tag{2.22}$$

$$\sqrt{\frac{2}{C_f}} = \frac{1}{\kappa}\ln \mathrm{Re}_\tau + B + B_1 - \frac{1}{\kappa} \tag{2.23}$$

where B_1 is a flow-dependent constant that is not equal to B. For the flow-controlled case, the skin-friction reduction can be expressed as a function of the wall shift ΔB using this relation. The skin-friction is captured in Re_τ (hu_τ/ν for channel half-height h), thus the skin-friction is extracted from Re_τ, yielding $\mathrm{Re_h}$ ($\mathrm{hu_e}/\nu$) based on channel height and upstream velocity only:

$$\sqrt{\frac{2}{C_f}} - \frac{1}{\kappa}\ln\sqrt{\frac{C_f}{2}} = \frac{1}{\kappa}\ln \mathrm{Re_h} + B + B_1 - \frac{1}{\kappa} \tag{2.24}$$

Gatti (2016) assumes the differences in $\mathrm{B_1}$ and κ to be unaffected by the flow control for a channel flow. When a drag-reduced flow and an uncontrolled flow (with subscript 0) are then considered, the change in skin-friction due to a shift in the wall intercept can then be defined when the same upstream Re_h is considered:

$$\sqrt{\frac{2}{C_f}} - \frac{1}{\kappa}\ln\sqrt{\frac{C_f}{2}} - \left(\sqrt{\frac{2}{C_{f,0}}} - \frac{1}{\kappa}\ln\sqrt{\frac{C_{f,0}}{2}}\right) = B_0 - B = \Delta B \tag{2.25}$$

The skin-friction changes can now be examined for the same upstream velocities. From Equation 2.25 it is observed that positive values for ΔB (upwards shifts of the logarithmic layer) lead to skin-friction reductions.

2.2.2 Riblets

Riblets are a drag-reducing method in which small grooves are applied to an otherwise flat surface and are inspired by shark-skin (see Figure 2.9). Choi (1989) postulates that the grooves restrict the movement of quasi-streamwise vortices with a resulting decrease in bursting activities near the wall. In applications riblets have been shown to have drawbacks as laborious efforts to apply them and degradation due to wear and dirt, annuling their effectiveness.

(A) (B)

FIGURE 2.9: Shark-skin (A) and riblet (B) geometry by Dean and Bhushan (2010).

Choi (1989) performed an experimental investigation on the effect of smooth and riblet wall surfaces using hot-wire anemometry. The drag reduction was determined by fitting the velocity profile with the law of the wall. For the riblet surface the a reduction in skin-friction of 3% was found. The near-wall turbulence intensity peak was found was found to be reduced by 10% for the riblet surface (Figure 2.10a). As a result it is also observed that the mean profile is shifted upwards (Figure 2.10b).

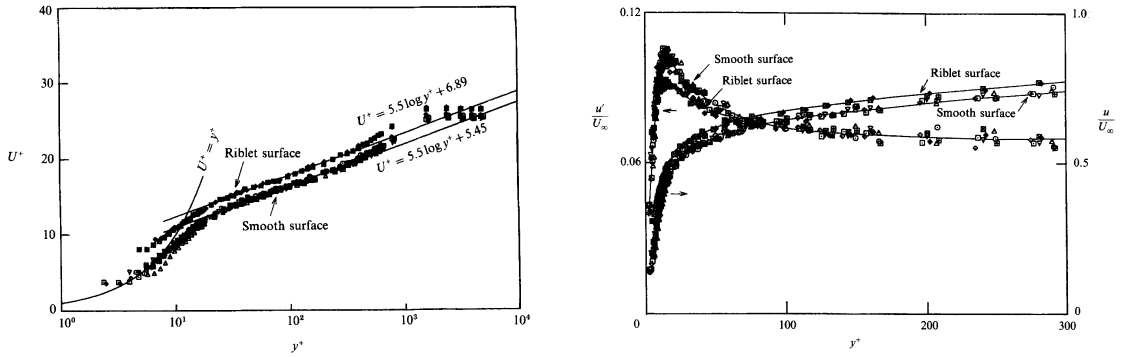

(A) Mean TBL velocity profile in wall units.

(B) Turbulent intensity and mean flow.

FIGURE 2.10: TBL properties for a smooth and riblet surface by Choi (1989).

Upwards shifts of the mean velocity profile and a decrease of turbulence statistics above triangular riblets were found by Choi et al. (1993) to lead to a 6% skin-friction reduction in a DNS study. Reynolds shear stress producing events were reported to be reduced in the riblet configuration, with a quadrant analysis pointing out the increase of positive Reynolds shear stress (Q1 and Q3) and the reduction of negative shear stress (Q2 and Q4). The same reduction in positive shear stress events is also reported by Sasamori et al. (2014), who investigated the drag reduction of a three-dimensional sinusoidal riblet surface in a channel flow supplemented by a PIV investigation. They found that the Q1 and Q3 events remain relatively unchanged, but reported reductions of Q2 and Q4 in both the buffer and the logarithmic layer. A maximum drag reduction of 11.7% was found, and the turbulence intensities were found to be smaller for the riblets.

Adverse pressure gradient. As in applications an adverse pressure is often encountered, a special interest is taken into the effectiveness of riblets in an adverse pressure gradient. Nieuwstadt et al. (1993) investigated riblets under such an adverse pressure gradient. Using a diverging straight upper wall to impose a pressure gradient, a drag balance and hot-wire anemometry to measure the skin-friction over a flat- and riblet surface, a drag reduction of 7% was found for moderate adverse pressure gradients. In a follow-up study, Debisschop and Nieuwstadt (1996) used the same experimental set-up to investigate drag reductions under higher pressure gradients and found a maximum drag reduction of 13%. Just as for zero pressure gradients a shift in the logarithmic layer was found, accompanied by a reduction of the turbulence intensity (see Figure 2.11). Turbulence properties in the outer layer were found to be unaffected by the riblet.

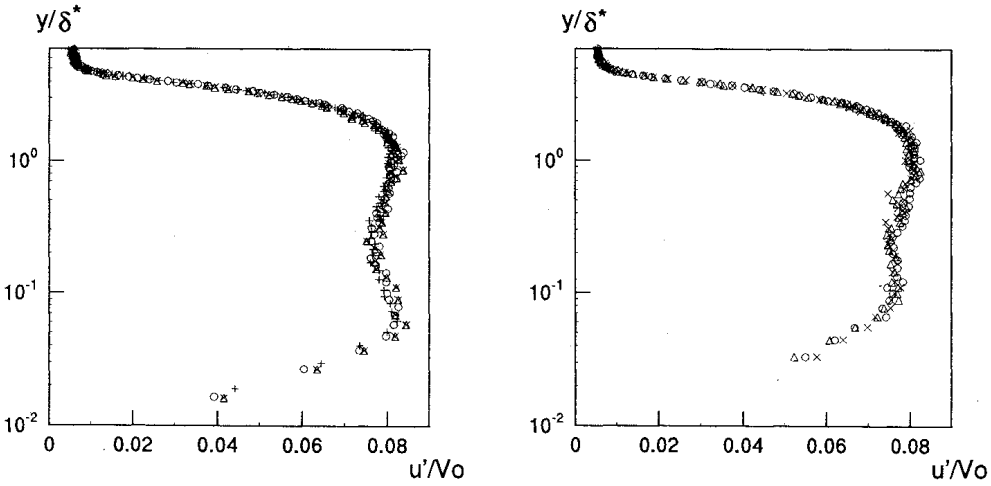

(A) Flat surface. (B) Riblet surface

FIGURE 2.11: Turbulence intensity for U_∞ = 15 m/s for H = 1.56 by Debisschop and Nieuwstadt (1996).

More recently, Klumpp et al. (2010) found a drag reduction in a DNS study using a riblet surface in an adverse pressure gradient boundary layer. A drag reduction of 6-7% was found for the adverse pressure gradient compared to 4-5% for the same riblets in a zero pressure gradient configuration. The results of the aforementioned authors show that the skin-friction reduction for a riblet surface seems to persevere under the application of an adverse pressure gradient.

2.2.3 Wall oscillations

Compared to the passive riblet, the actively oscillating walls are an *active* flow control mechanism to reduce the turbulent skin-friction drag. Relatively large drag reductions up to 45% have been reported by Choi and Clayton (2001) and up to 45% by Jung et al. (1992). Drawbacks of the oscillating wall are the large energy inputs for the moving system, annulling much of the energy saved by its actual application. Moving systems also impose weight penalties when they are applied. Due to the large reported drag reductions, they are however still investigated numerously.

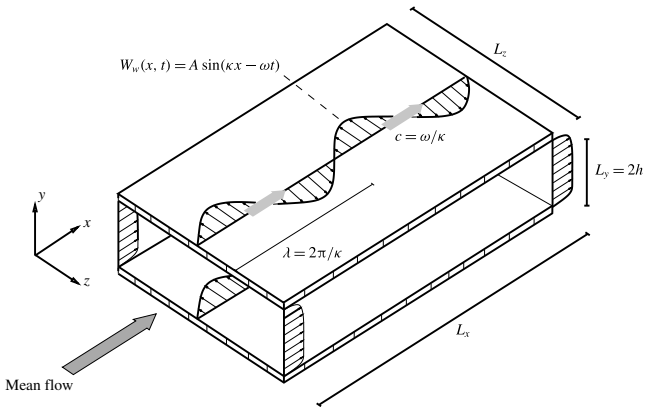

FIGURE 2.12: Oscillating wall schematics for a turbulent channel flow by Gatti (2016).

Choi et al. (1994) explored flow control concepts for a turbulent channel flow by application of streamwise-, spanwise and wall-normal flow control in a numerical study. For the spanwise flow control an upwards shift in the logarithmic layer and a decrease of turbulence intensity and Reynolds stress (mainly Q2 and Q4) throughout the boundary layer was found. This was confirmed by Kim and Lee (2017), who found a decrease in Reynolds stress for Q2 and Q4 events for an oscillating wall in a numerical study (Figure 2.13).

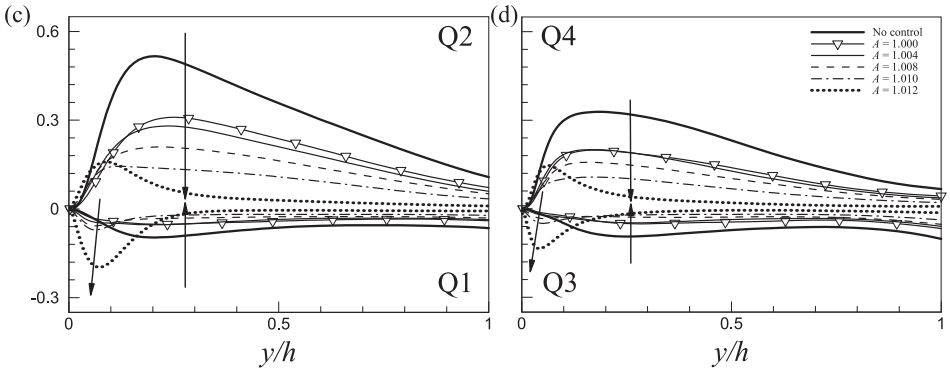

FIGURE 2.13: Reynolds shear stress quadrant contributions normalized by u_τ^2 for different oscillation amplitudes by Kim and Lee (2017).

Jung et al. (1992) investigated the response of wall-flow turbulence to high frequency oscillations of a channel wall using DNS. Skin-friction reductions of 10% were found, with a maximum drag reduction of 40%. They posed that this maximum drag reduction was achieved by a suppression of the bursting process, and the accompanying decreasing Reynolds stress (-40%) and turbulent intensities (-14% for u', -30% for v'). The mean velocity profiles showed that the logarithmic part of the velocity profile was shifted upwards, analogous the previously discussed riblets. These reported shifts were found to be even more profound when the oscillating frequencies were varied in a study by Choi and Clayton (2001) (Figure 2.14a). They performed an experimental wind-tunnel study in which drag reductions up to 45% were found for a spanwise-oscillating wall. In correspondence to Choi et al. (1994) and Jung et al. (1992) the turbulence intensity was decreased in the near-wall region (Figure 2.14b) and they proposed a conceptual model in which the Stokes layer and its corresponding spanwise vorticity impedes the near-wall burst activity associated with high turbulence production peak.

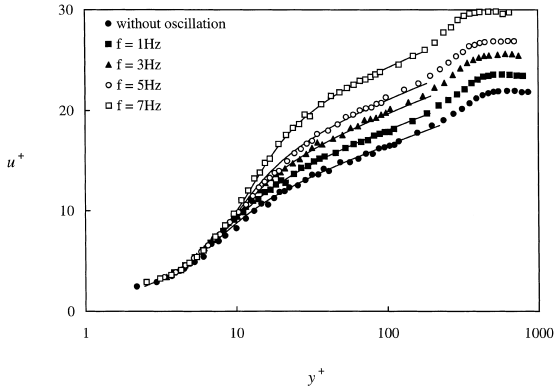

(A) Mean TBL velocity profile in wall units.

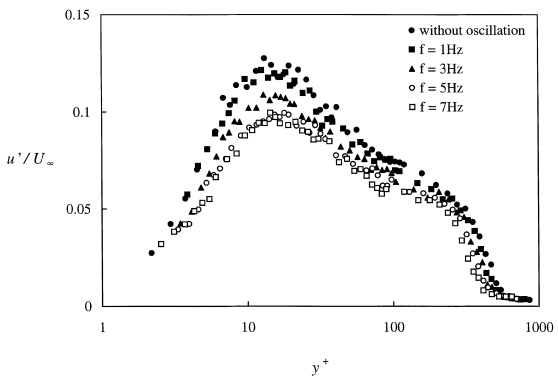

(B) Turbulent intensity.

FIGURE 2.14: Turbulent boundary layer properties for different oscillating frequencies by Choi and Clayton (2001).

Proposed mechanism. Choi et al. (1998) describes that a thin layer of shear flow is formed due viscous diffusion of the wall due to the surface oscillating: the so-called previously mentioned *Stokes layer*. The vortex sheets created by the Stokes layer are convected throughout the boundary layer, as Choi et al. (1998) found by performing flow visualization. In Figure 2.15 a conceptual model is shown in which they propose that the spanwise vorticity is tilted during the upward and downward motion, yielding a net spanwise vorticity Ω_z located at the end of the buffer layer that reduces the velocity in the buffer layer and increases the velocity in the logarithmic layer, yielding an effective shift in the logarithmic layer.

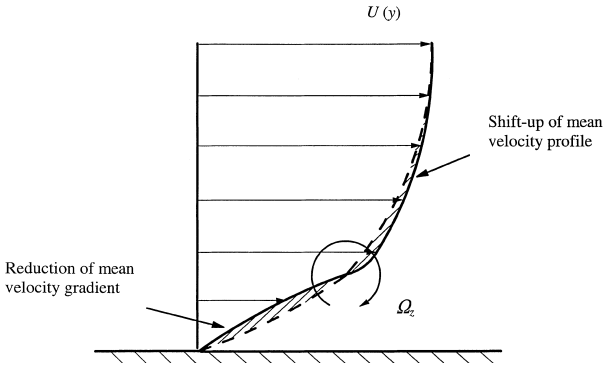

FIGURE 2.15: Conceptual model for a drag reduction by an oscillating wall by Choi et al. (1998). The upwards shift of the velocity profile is explained by a vorticity Ω_z induced by a Stokes layer.

In a DNS study Yakeno et al. (2014) investigated the modification of turbulent coherent structures due to the alternating Stokes layer of a wall oscillation. They decomposed the different contributions of the quadrant events to the skin-friction drag by applying the FIK identity by Fukagata et al. (2002) to integrate the Reynolds shear stress. They investigated the modification of the quasi-streamwise vortices by the spanwise oscillations and found two primary mechanisms:

1. *Suppression of a ejection (Q2) event* occurs when the spanwise shear opposes the rotation of the quasi-streamwise vortex.

2. A quasi-streamwise vortex is tilted slightly in the streamwise direction when the spanwise shear coincides with the rotation of the quasi-streamwise vortex, resulting in a *suppresion of a sweep (Q4) events*.

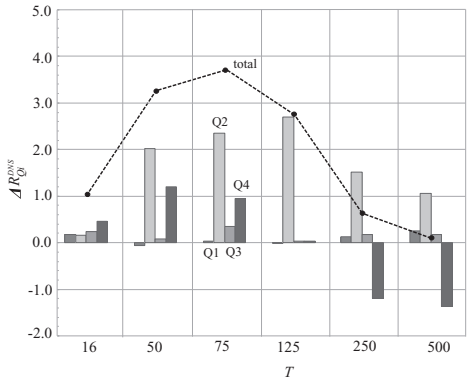

FIGURE 2.16: Quadrant contributions to the bulk mean velocity based on the FIK identity by Yakeno et al. (2014). Uncontrolled (non-oscillating) value is subtracted. Positive contributions of ΔR_{Qi}^{DNS} indicate decreased Reynolds stresses compared to the uncontrolled case.

The suppression of the Q2 and Q4 event leads to a smaller turbulent skin-friction coefficient as they contribute positively to the skin-friction coefficient as Reynolds shear stresses. It is observed in Figure 2.16 that at T > 75 the drag reducing effect of sweep suppression is diminished. Akin to Yakeno et al. (2014), Kim and Lee (2017) showed that the streamwise vortices are severely inhibited when spanwise flow control is applied. When the amplitude becomes too large the suppression of new vortex formation is no longer happening and turbulent activity is reinstigated (Figure 2.17), similar as found by Yakeno et al. (2014), indicating a clear optimum for a drag reductiom.

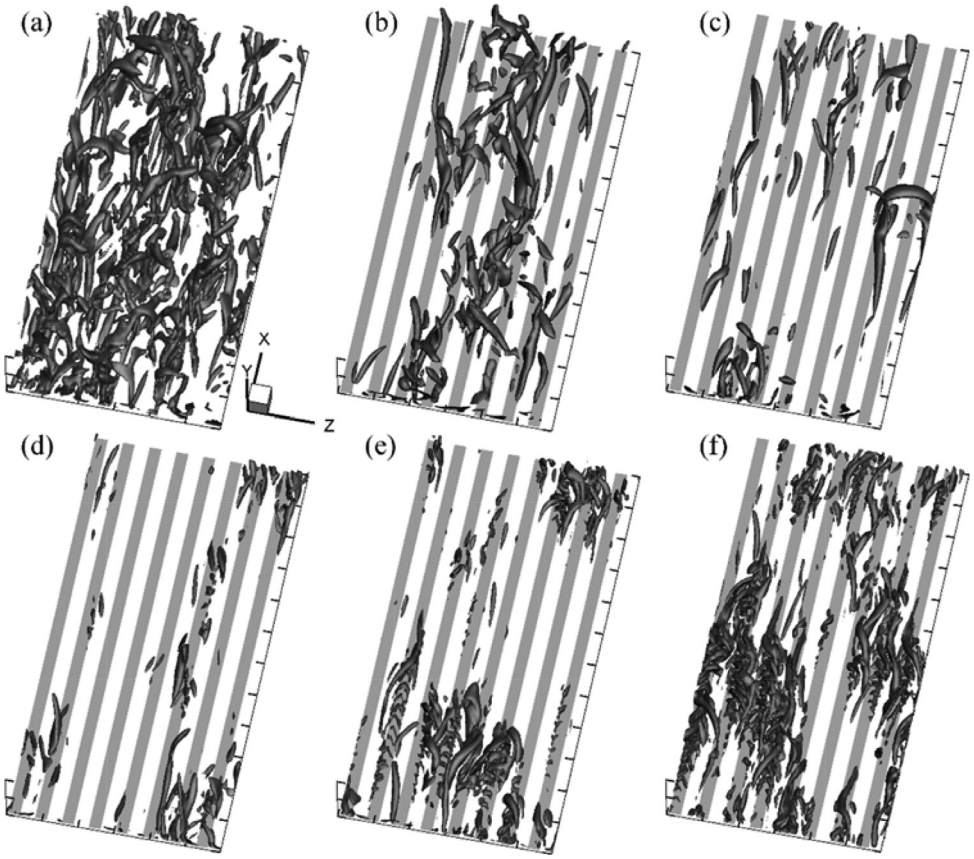

FIGURE 2.17: Vortical streamwise structures in the near-wall region for increasing amplitude of the wall oscillation by Kim and Lee (2017). (a) shows the no-control case. A clear optimum for the reduction of vortical structures is seen for the amplitude in (d). Increasing amplitude further increases vortical structures.

2.2.4 Compliant coatings

Another passive drag-reducing method based on the animal kingdom (dolphins, in this case) is by the application of a compliant coating to a surface. Such a compliant coating allows the deformation of the wall by the shear stresses yielding a reduced turbulence intensity [Duncan (1986)] and drag reductions up to 50% have been reported by Kramer (1960). In the attempt to recreate the large drag reductions reported by Kramer (1960), several experimental investigations have been performed. Choi et al. (1997) performed a validation experiment of the experiment by Kulik et al. (1991), who found a skin-friction drag reduction when a compliant coating (silicone rubber) was applied in a turbulent boundary layer. From the two coatings they tested they found a skin-friction drag reduction of 7%. They

reported an upwards shift of the logarithmic layer and a decrease of turbulent intensity for a drag-reducing compliant coating.

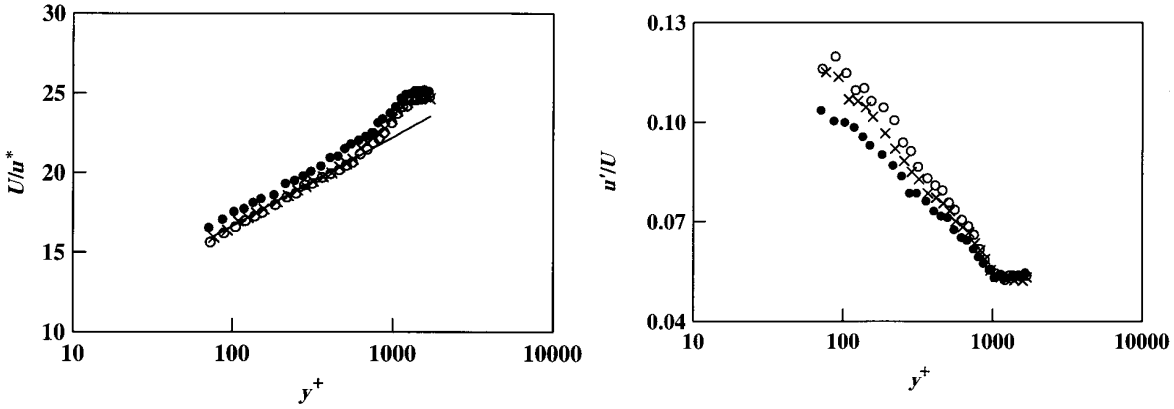

(A) Mean TBL velocity profile in wall units.

(B) Turbulent intensity and mean flow.

FIGURE 2.18: Turbulent boundary layer properties for a rigid (×), drag-reducing coating (•), and drag-increasing coating (○) surface for U_∞ = 4 m/s by Choi et al. (1997).

2.2.5 Combined and other methods

Another way in which skin-friction was found to be decreased is by applying a geometrical sinusoidal deformation to a wall. Kendall (1970) reported that the total skin-friction could be as much as 25% lower compared to a flat surface for such a wavy wall. Hamed et al. (2015) found a decrease in Reynolds stresses and turbulent kinetic energy for a geometry in which two wavy walls were superimposed (creating several 'mountain valleys'). Ghebali et al. (2017) looked at a boundary layer over wavy wall with a 45% tilt to the streamwise axis in an experimental study. They found an upwards shift of the logarithmic layer, a turbulent intensity reduction and a reduction of the Reynolds shear stress reduction throughout the boundary layer, resulting in a total drag reduction of 0.5%. Gad-el Hak (2006) provides the explanation that regions of convex and concave curvature cause the occurrence of a pressure gradient, in which the boundary layer is relaminarized when it enters a favorable region. The effectiveness of active and passive turbulent drag reduction methods also lead to attempts to combine the drag reducing properties of each to yield a higher drag reduction. Roggenkamp et al. (2015) combined the use of wavy walls with a spanwise transversal surface wave in an experimental PIV and μ-PTV study and found an optimal skin-friction drag reduction of 3.4%. They found an accompanying upwards shift in the logarithmic layer and a reduction of the Reynolds peak stress, however increasing Reynolds number led to an insignificant drag reduction or even a drag increase.

2.3 Drag reduction by dimples

With the framework for skin-friction drag reduction layer in the previous sections, in this section the dimpled surface is investigated further. Compared to riblets, dimples are relatively easy to maintain and do not require profound changes to the surface of a vehicle. Compared to oscillating walls dimples do not require a heavy power-consuming mechanism to induce oscillation.

The first data on a perceived drag reduction by a dimpled surface was publicized by Kiknadze et al. (1984). They discovered the positive effect of a dimpled surface on the drag during a heat transfer problem inside a nuclear plant. In later work they named the method 'Tornado-Like Technology' (TLT), due to the perceived existence of a strong vortex inside the dimple responsible for the drag reduction. No consensus has been achieved on the actual drag-reducing mechanisms, although several theories have been proposed.

2.3.1 Overview

Other than Kiknadze et al. (1984) several authors and research institution have been investigating the subject ever since. One institution that has found a drag reduction for a dimpled surface is the National University of Singapore (NUS). The first investigation by Mitsudharmadi et al. (2009) studied the effect of dimple depth on the flow topology in a blow-down low-speed wind tunnel. A second investigation by Tay (2011) found the first drag reduction in a channel flow with dimples for different coverage ratios by measuring the pressure drop over the dimples. Tay (2011) found that for both coverage ratios considered the drag decreased with increasing Reynolds number, yielding a maximum drag reduction of 2% at the maximum considered Reynolds number. Most recently Tay et al. (2015) found drag reductions up to 3% with increasing Reynolds number for a dimpled surface and found regions where the flow was pulled in and pushed out of the sides of the dimple, resulting in a converging-diverging flow topology. Tay et al. (2015) proposed that the interaction between dimples with this converging-diverging flow topology could have the same drag reducing effect analogous to the one found for the oscillating wall.

At Delft University of Technology (DUT), Vervoort (2007) performed both a numerical and experimental investigation into flows over dimpled surfaces using direct force measurements with a load cell and found drag reductions up to 20%. Several years later Van Nesselrooij (2015) performed another experimental investigation into dimples using direct force measurements and found a drag reduction up to 4% only for the shallow dimples in a staggered dimple pattern. For a staggered shallow dimple the same drag reducing trend with Reynolds number was observed as Tay et al. (2015) did. Independently of Tay et al. (2015) the analogy to an oscillating wall was also proposed by Van Nesselrooij (2015). In an attempt to achieve higher Reynolds numbers Van Campenhout (2016) added an inlet ramp to accelerate the flow such that higher upstream velocities were achieved above the dimpled surface that had the same properties as the one of Van Nesselrooij (2015). Van Campenhout (2016) did however not find any drag reduction, but quantified a surface wave with oil flow visualization. Van Campenhout (2016) proposed that the absence of a drag reduction was caused by the favorable pressure gradient of the inlet ramp, thereby impeding the turbulent structures that led to a drag reduction.

The drag reduction by a dimpled surface is not ubiquitous. B. Zhao et al. (2004) performed a flow visualization study on flow structures inside just two dimples inside a channel flow. By measuring the friction factor over the channel no measurable drag difference was found. Lashkov and Samoilova (2002) determined the skin-friction of a surface with sharp-edged dimples at various depths for a coverage ratio of 32%. They performed their experiments in a flow facility with speeds from 10 m/s to 100 m/s. Two dimple design based on the design of Kiknadze et al. (1984) and additional one defined by themselves were utilized. All of these configurations yielded a drag increase up to 50% with increasing Reynolds number. Lienhart et al. (2008) performed another experimental investigation and a complementary DNS study over an array of dimples. They answered no to the question whether their dimpled surface led to a drag reduction. For a velocity of 6 m/s a skin-friction reduction of

0.38% was found, whereas an increase of 2% for 12 m/s. These values are however within statistical uncertainty found during their experiment.

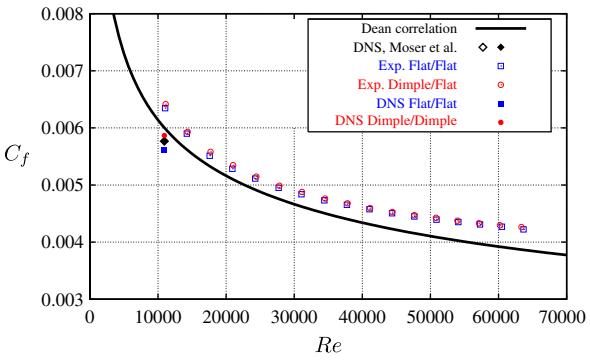

FIGURE 2.19: Skin-friction coefficient C_f versus streamwise Reynolds number Re by Lienhart et al. (2008).

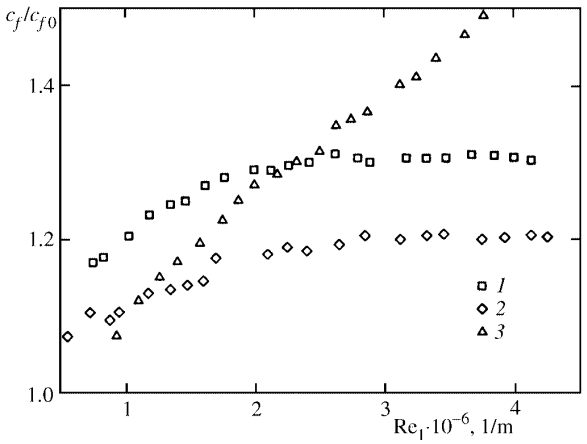

FIGURE 2.20: Skin-friction ratio compared to flat plate ($c_f/c_{f,0}$) for increasing upstream unit Reynolds number Re_1 (U_∞/ν) by Lashkov and Samoilova (2002).

The most recent research from the original authors by Leontiev et al. (2017) investigated the effect of several staggered dimples of different geometrical configurations. Using a floating head drag balance the skin-friction was determined for velocities from 25 m/s to 125 m/s in a subsonic windtunnel.

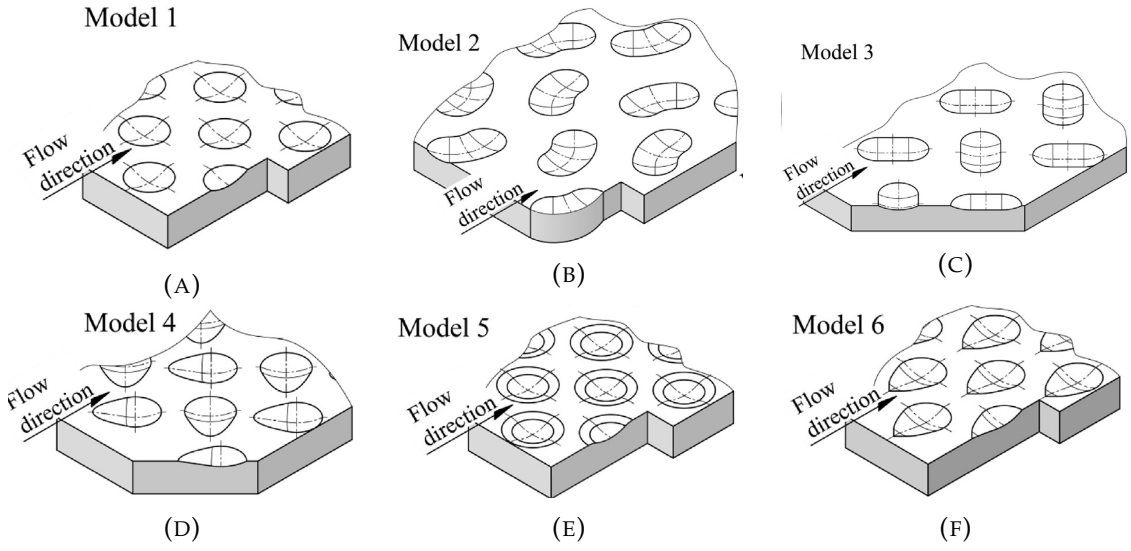

FIGURE 2.21: Dimple geometries considered by Leontiev et al. (2017).

From Figure 2.22 it is observed that all configurations defined in Figure 2.22 ultimately lead to a drag increase when the flow velocity is increased. Only for the round-edged dimple configuration of Model 5 a small drag reduction is observed in the low Reynolds number regime.

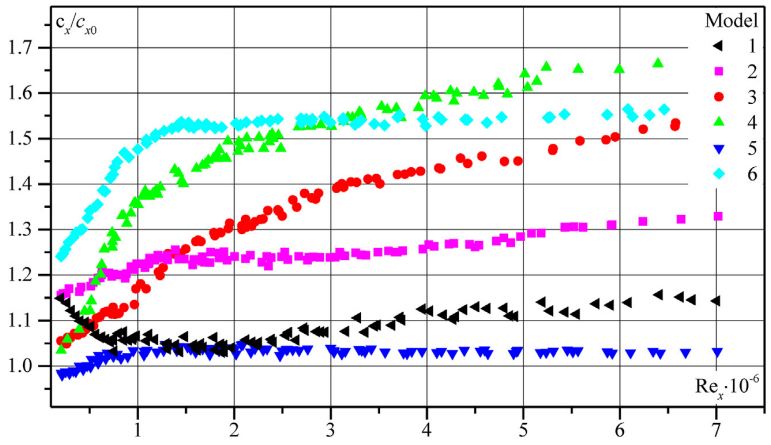

FIGURE 2.22: Drag ratio c_x compared to flat plate $c_{x,0}$ as a function of Reynolds number based on (constant) boundary layer development length and upstream velocity by Leontiev et al. (2017).

2.3.2 Effect of geometry

The geometry of a dimpled surface can be described by the cross-sectional properties of the dimple itself, and the pattern in which the dimples are oriented. The dimple cross-sectional properties can be defined by the diameter D, edge radius r and the depth d, see Figure 2.23.

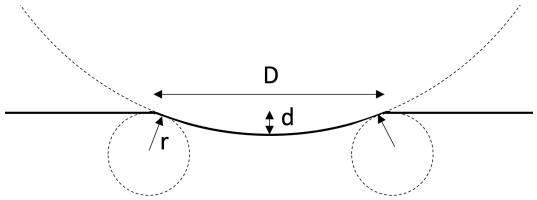

FIGURE 2.23: Dimple cross-sectional properties by Van Nesselrooij (2015).

Depth. Various investigations have been performed into the effect of dimple depth on the drag behavior and the flow topology. Mitsudharmadi et al. (2009) varied the d/D-ratio from 4% to 12% in a rounded-edged dimple geometry in a staggered pattern at a fixed free-stream velocity of 5.5 m/s in a channel flow. The wall-shear stress was found to increase up to 40% for all d/D ratios (see Figure 2.24). Burgess and Ligrani (2004) varied the d/D ratio at 10%, 20% and 30% in an experimental investigation, and measured the friction factor loss over a dimpled plate in a channel. They observe that the values of d/D higher than 10% generally increase skin-friction with Reynolds number, while they stay relatively constant for d/D = 10%, although still with a skin-friction increase. This beneficial effect of a small d/D-ratio was found by Van Nesselrooij (2015), who observed a drag reduction for d/D = 2.5%. Drag reductions where also found for d/D = 5%.

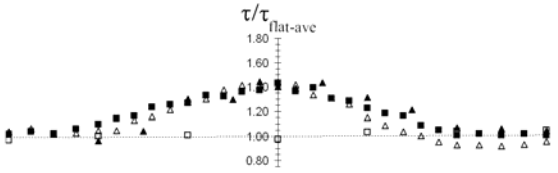

FIGURE 2.24: Spanwise variation (z/D) of wall shear stress ratio compared to the flat plate case for varying depth ratios by by Mitsudharmadi et al. (2009).

When varying the depth of the dimple the flow topology changes as well. Tay et al. (2014) showed the effect of dimple depth on the flow structures in the dimple using dye streaks. In Figure 2.25 the effect of the dimple depth is shown by Tay et al. (2014). For small depths ($d/D < 10\%$) it is observed that the flow follows a converging-diffuser topology for both the round and sharp edged dimple. For depths higher than $d/D = 10\%$, the flow organizes into two symmetric counter rotating vortices for the sharp edged dimple. For a deep rounded edge, the flow organizes into a single tornado-like vortex, as reported in the work of Kiknadze et al. (2012a)

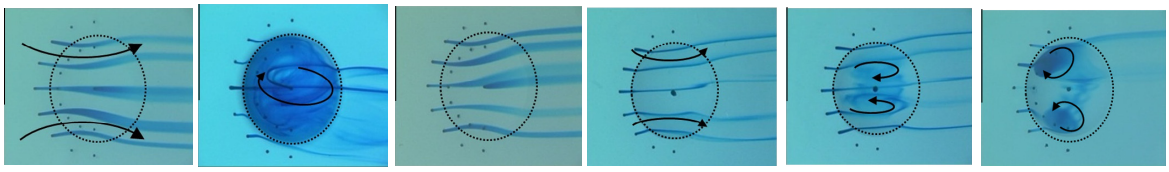

(A) $d/D = 5\%$. (B) $d/D = 50\%$. (C) $d/D = 5\%$. (D) $d/D = 10\%$. (E) $d/D = 15\%$. (F) $d/D = 20\%$.

FIGURE 2.25: Flow topology affected by dimple depth by Tay et al. (2014). Dimples in (A) and (B) are round edged, (C) to (F) sharp edged.

Edge radius. From the previous section it was observed that in the studies by Lashkov and Samoilova (2002) and Burgess and Ligrani (2004) no drag reduction was found. Both studies applied a sharp edged dimple which were both ineffective in reducing the dag. Terekhov et al. (1993) described that the resistance of a dimple with smooth edges is about half as great as for the sharp edged dimples, and delays the formation of vortical structures inside the dimple. Zhou et al. (2016) performed an experimental investigation to quantify the characteristics of the turbulent boundary layer inside of the dimple on a dimpled array in a staggered pattern. The dimples in their investigation had a sharp edge and a d/D-ratio of 0.2. They found that the friction factor over a dimpled plate is 30%-80% higher than for a flat plate, with an increasing friction factor for increasing Reynolds number. Finally, it is observed from Figure 2.22 by Leontiev et al. (2017) that the round-edged dimple led to a lower skin-friction coefficient than the sharp-edged dimple (model 1 and 5 from Figure 2.21 respectively), although both configurations ultimately led to a drag increase.

Pattern and coverage ratio. When a dimple array is considered in a study, generally two main patterns are observed: flow-aligned or staggered (see Figure 2.26). The ratio between the dimple-cover area and the actual area is the coverage ratio S.

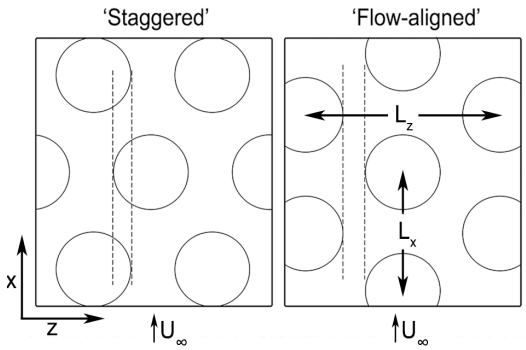

FIGURE 2.26: Definition of streamwise and spanwise spacing and difference of a staggered and flow-aligned pattern by Van Campenhout (2016).

An interesting case is when the same dimple geometry is utilized while the pattern is switched from flow-aligned to staggered. For the same dimple geometry, Van Nesselrooij (2015) shows that the drag reduction effect of a dimpled surface was annulled by rotating the geometry into a flow-aligned pattern. A staggered dimple pattern was further found to yield drag reductions by Vervoort (2007), Tay (2011) and Tay et al. (2015). Using an actuated dimpled surface, in which dimples could be activated at will, Van Campenhout (2016) tested patterns with increased spanwise and streamwise spacing, patterns in which a wavy surface was simulated and two surfaces in which the dimples were placed in a streamwise oscillatory manner. For all these patterns Van Campenhout (2016) did not find a drag-reduction.

Next to the orientation the pattern is also defined by the coverage ratio, which describes what part of the surface is covered by dimples. For low coverage ratios the spanwise and streamwise spacing L_z and L_x will be higher than for a low coverage ratio. In his experiments Van Nesselrooij (2015) observed the beneficial effect for a low coverage ratio. Tay et al. (2015) observed a drag reduction for both a high (90%) and low (40%) coverage ratio (see Figure 2.27).

2.3.3 Effect of Reynolds number

Several studies have been performed in which the upstream Reynolds number is prone to variation. Both Van Nesselrooij (2015) and Tay et al. (2015) performed experimental investigations over a dimpled array, both using a staggered shallow round-edged dimple array (Figure 2.27). Both investigations show a drag increase in the low Reynolds number regime, with a downward trend with Reynolds number. It was already proposed by Vervoort (2007) and shown by Lienhart et al. (2008) that the dimple shape causes a higher pressure drag due to its shape compared to a flat plate. Both Tay et al. (2015) and Van Nesselrooij (2015) propose that the skin-friction reduction overtakes the pressure drag for increasing Reynolds numbers.

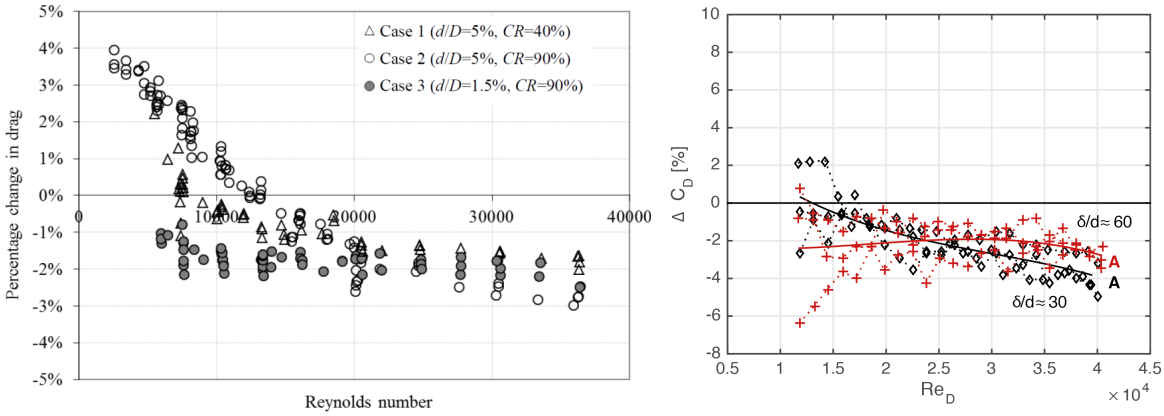

(A) Tay et al. (2015). (B) Van Campenhout et al. (2016).

FIGURE 2.27: Drag reduction with increasing dimple diameter-based Reynolds number.

Once again it must be noted that this trend is not ubiquitous. Lashkov and Samoilova (2002) increased the velocity up to 100 m/s in a wind-tunnel experiment, and found drag increases up to 50% for increasing unit Reynolds numbers (Figure 2.20). Van Campenhout (2016) increased the Reynolds number range over the same geometry as Van Nesselrooij (2015), but found no drag reduction with increasing Reynolds number. Finally, the experimental work provided by Leontiev et al. (2017) showed an increase in skin-friction when changing

the upstream velocity from 25 m/s to 125 m/s for all the different dimple configurations considered.

2.3.4 Proposed working principles

Throughout the time that experimental and numerical investigations have been performed into the drag reduction by a dimpled surface, there is still no scientific consensus on how the drag reduction in achieved. In this section the commonly reported theories are discussed.

Tornado-Like Technology. The original explanation as given by Kiknadze et al. (2012b) states that inside the dimple self-organizing secondary tornado-like jets are established, that induce a counteracting shear against the drag force leading to an overall drag decrease. These proposed vortices have been observed by Isaev et al. (2005) and Tay et al. (2014), but their direct link to a drag reduction is still not present due to lack of details in respect to the experiments. This theory is also proposed by Vervoort (2007), evidenced by simulations (Figure 2.29), who says that the vortex causes reduced wall shear stress in the upstream part of the dimple and a small increase of the pressure drag in the downstream part of the dimple, yielding an effective drag reduction.

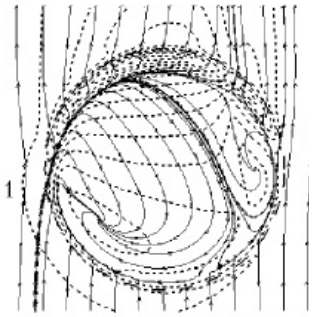

FIGURE 2.28: Isolines of pressure by Isaev et al. (2005).

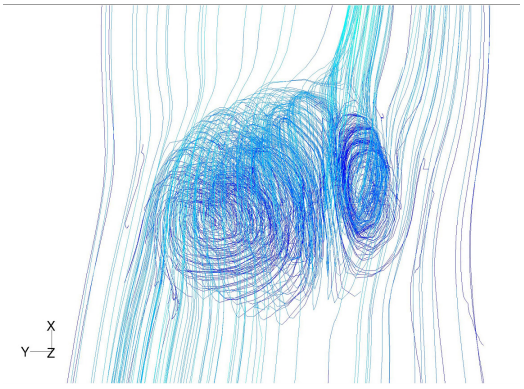

FIGURE 2.29: Pathlines over a dimple by Vervoort (2007).

Relaminarization. It was described in Section 2.1.3 that under a certain acceleration parameter K the turbulent boundary layer returns to a quasi-laminar state. In respect to a dimple, it can be argued that analogous to a wavy wall, drag reductions are attained when the turbulent boundary layer is relaminarized in the downstream part of the dimple. The working mechanism is then explained by Gad-el Hak (2006) as that the balance between the resulting pressure drag and the skin-friction drag leads to an overall drag reduction by a net balance of these two forces.

Spanwise shear. Another proposal for the drag-reducing mechanism is postulated by Van Nesselrooij (2015) and Van Campenhout (2016) at DUT and by Tay et al. (2015), and states that analogous to drag reductions for oscillating walls, spanwise shear is the reason for the drag reduction. Tay et al. (2015) backs this theory with the formation of spanwise velocity bands and the converging-diverging flow topology (Figure 2.30) observed by Tay et al. (2014).

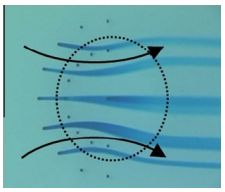

FIGURE 2.30: Converging-diverging flow topology observed with dye-streaks by Tay et al. (2014).

This theory states that the converging-diverging flow topology has a drag-reducing effect analogous to the drag-reducing effect found for the oscillating wall. It is proposed that the interaction between dimples causes regions of spanwise oscillations, forming a Stokes layer that inhibits turbulent coherent structures. Van Campenhout (2016) quantified the flow over a dimpled surface by means of Particle Image Surface Flow visualization (PISFV) and detected a spanwise wave alternating between the dimples. No drag reduction was found however, which Van Campenhout (2016) argued to be caused by the suppression of Q2 and Q4 events by the favorable pressure gradient applied by the ramp preceding the test plate in the experimental set-up.

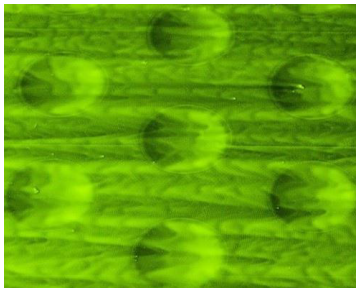

FIGURE 2.31: Surface oil flow visualization by Van Campenhout (2016).

Chapter 3

Methodology

In this chapter the methodology surrounding the experimental procedure is revealed and justified. Three experimental methods are discussed in sequence, which are direct force measurements (DFM), particle image velocimetry (PIV) and hot-wire anemometry (HWA). Before these are discussed in detail, first the experimental set-up and the aerodynamic design based on a boundary layer simulation, are spelled out in Section 3.1.

3.1 Experimental design

Before any experiment can be performed a theoretical and physical framework are required. In this section a theoretical framework is given by the aerodynamic design and the resulting test matrix in Section 3.1.2 while a physical framework which makes up the experimental set-up is given in Section 3.1.1. This physical framework needs some initial deliberation which is provided in a moment's notice.

The test plate geometr of Table 3.1 is used in the experiment. This geometry contains all the beneficial geometrical properties for drag reductions described in Section 2.3.2 and is the plate configuration where a maximum drag reduction of 4% was found. In this configuration the dimples are placed in a staggered pattern. This is also the geometry for which Van Campenhout (2016) found no drag reduction. Due to this contrast it is a natural choice for a dimpled plate configuration in this experimental research.

TABLE 3.1: Drag-reducing dimple geometry in mm by Van Nesselrooij (2015) (see Figure 2.23 and 2.26 for definition of parameters).

D	**d**	**r**	$\mathbf{L}_x$	$\mathbf{L}_z$
20	0.5	10	57.2	33

The test plate in the same order of dimension as the previous experiments at DUT, and contains 21 rows of dimples with 11 dimples each row, totalling 231 dimples. In order to perform direct force measurements the test plate must be decoupled from the test section. To this end a gap of 2 mm is created between the test section and the test plate by constraining the plate width to 396 mm (whereas the test section has a width of 400 mm). The geometry is shown in Figure 3.1 and has a surface area S = 0.25 m^2. The same plate dimensions (without the dimples) is also used to create a flat plate for comparison.

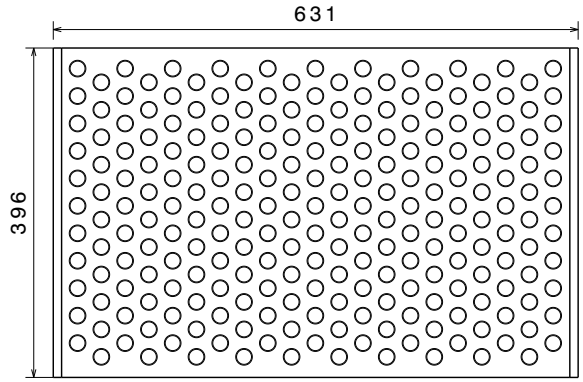

FIGURE 3.1: Test plate dimensions in mm.

Since the interest of this research is to identify the effect of a pressure gradient, a means must be found to apply a pressure gradient. Whereas an airfoil has pressure gradients due to the presence of curvature, a straight test plate has by no means an internal mechanism to create a pressure gradient. A pressure gradient exists due to the acceleration and deceleration of the flow. Bearing in mind the mass-conservation relation, which states that (assuming density to be constant) that area times velocity remains constant, indicating that a changing cross-sectional area can induce acceleration and deceleration. This implies that a pressure gradient can also be applied by changing the exterior area (keeping the bottom geometry flat). In a similar fashion to Starke et al. (1999) and Van der Hoeven (2013) and in riblet drag reduction research by Debisschop and Nieuwstadt (1996) it is chosen to use a planar diffuser to apply a pressure gradient on the test plate, defined purely by its deflection angle φ (see Figure 3.2). Having several fixed locations to attach it, the plane diffuser has the advantage that pressure gradients can be easily adjusted and reproduced and is also easily manufactured. A schematic set-up is presented in Figure 3.2.

This set-up is then attached to the flow facility. The flow facility at hand is the W-tunnel at Delft University of Technology. This tunnel is driven by a single fan, which can be controlled by setting the RPM. The W-tunnel fan instead accelerates the flow along a straight path through a nozzle. A 0.4 $\times$ 0.4 m nozzle is chosen to have have an upstream velocity range up to U_∞ = 34 m/s. To allow the boundary layer to develop an additional extension of 810 mm is added before the test section. A carborundum strip of 20 mm is added at the end of the W-tunnel (x = -975 mm) contraction to ensure a turbulent flow at the start of the test plate.

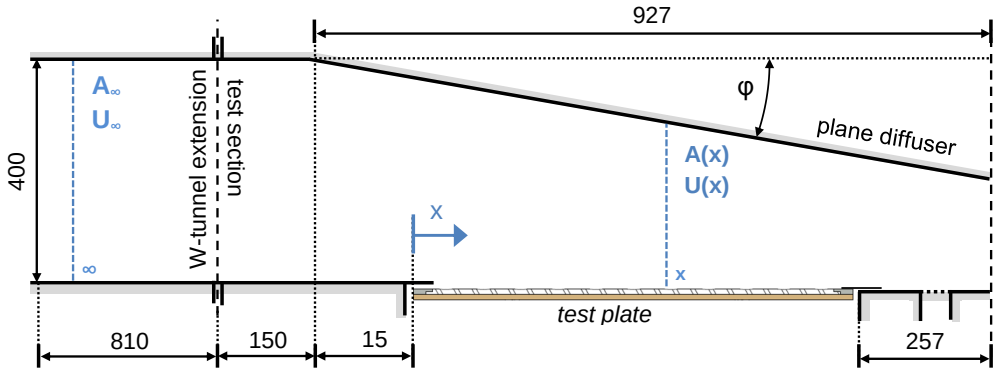

FIGURE 3.2: Schematic representation of a planar diffuser.

3.1.1 Experimental set-up

A schematic set-up of the test-section was shown in Figure 3.2 which in this section will be refined for experimental suitability. The test section has to go through three different experimental techniques, namely DFM, PIV and HWA. All these have their different general requirements that have to be taken into account. The DFM campaign uses a flexure-based drag balance, of which the details will be elaborated upon in more detail in Section 3.2.3. This balance requires the test plate to be completely detached from the test section, such that the drag force is not thwarted by friction with the wall. As a result spacing gaps are required at the front, back and the sides. The PIV measurements require *optical* access to the test plate. To accommodate this requirement the test section is primarily made of Plexiglas. The HWA measurements require *physical* access. To this end a sealable gap is created downstream behind the test plate such that the HWA apparatus can be inserted to the test section. To allow for a straightforward changing of the plates, a sliding system is devised in which the plate can be easily inserted and removed from the test section without the use of bolts. To allow this sliding to occur, a door is created by which the test-section can be opened. The set-up and its important attributes are shown in Figure 3.3.

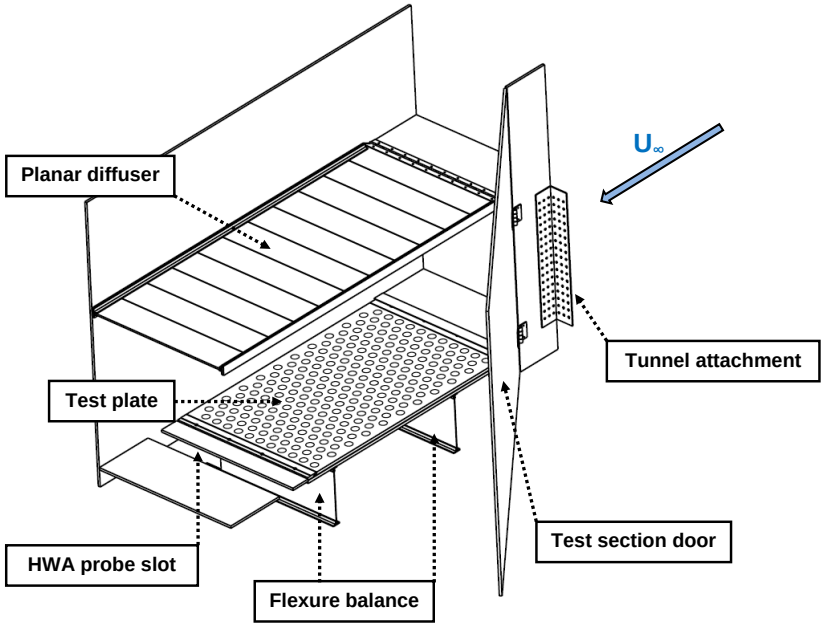

FIGURE 3.3: Schematic test section

In the aerodynamic model of the boundary layer it is assumed that the velocity changes only in the streamwise direction. In reality the wall-normal velocity distribution will not be constant at a fixed streamwise position. Since the boundary layer at the top diffuser wall is inclined more sharply in respect to the W-tunnel extension compared to the test plate, it is more likely to separate at the top wall. To tackle this slots are added in the top wall, in similar fashion to Van der Hoeven (2013) and Starke et al. (1999). These slots allow for natural boundary layer suction due to larger pressure inside the test section due to an APG, thus allowing the boundary layer to have a 'fresher' start when traversing a slot. When required a screen is added in the back to create a larger pressure inside the test section. In order to have a on-the-site approach and to allow for quick changing it is chosen to divide the top wall in 10 sliding plates instead of using one fixed configuration. Using this in combination with tufts to check for flow separation (Figure A.4) it is then possible to maintain attached flow at the top wall. A schematic view of the top wall is given in Figure 3.4.

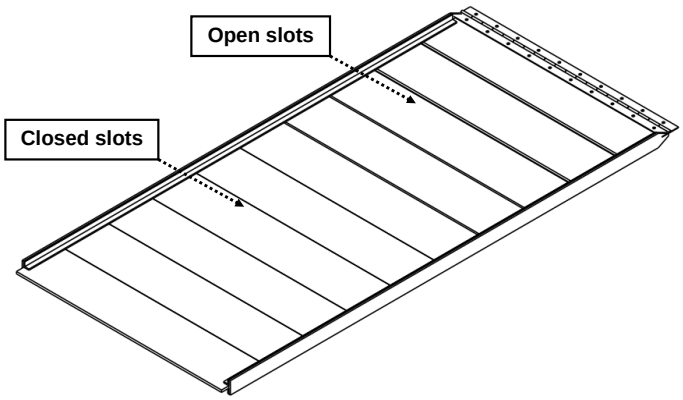

FIGURE 3.4: Diffuser wall with slots.

The pressure gradient and the pressure coefficient are connected to the change in freestream velocity (see Equation 2.13). Placing large pressure probes into the flow to measure the static pressure at multiple streamwise locations would introduce large flow disturbances when intricate differences in drag need to be captured. In order to monitor the pressure gradient 16 pressure taps are added on the anchored side wall, see Figure A.5. They are placed 30 mm above the surface, as to measure the pressure just above the boundary layer. Then two rows of 8 pressure taps are added with a spacing of 90 mm in the streamwise direction and a wall-normal spacing of 80 mm between the two rows, where the first pressure tap starts at x = 15 mm, just before the test-section transitions to the test plate. Pictures of the test-section including the pressure taps are given in Appendix A.

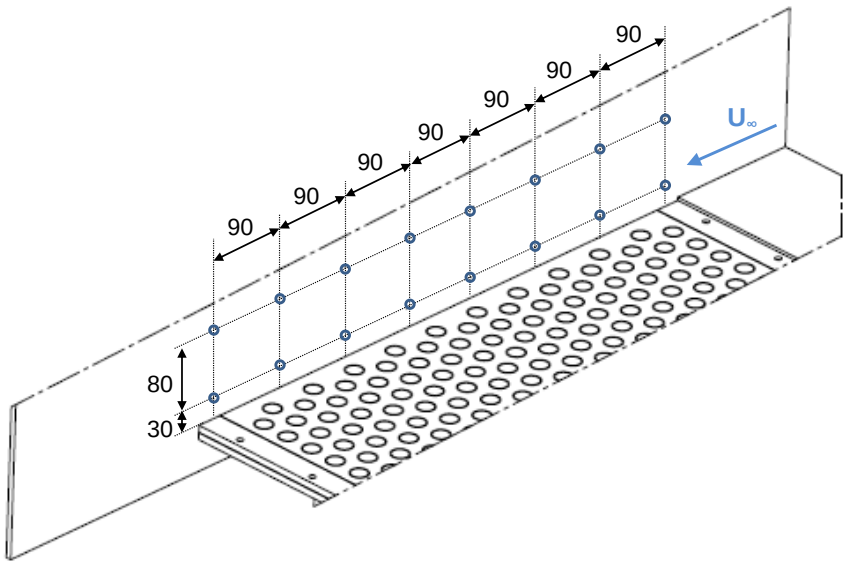

FIGURE 3.5: Pressure taps on the rigid wall.

3.1.2 Aerodynamic design

In order to have a first order estimate of how the boundary layer behaves and to find proper cases to perform the experiments in this section an aerodynamic design of the experiment is elaborated upon. Determining the initial diffuser angles φ for the experiment is dependent on the flow conditions that are wanted at the flat plate section. To this end an aerodynamic model of the boundary layer in the test section is devised. Traditional empirical relations that are used to compute turbulent boundary layer development under a ZPG are no longer

valid when a pressure gradient is applied. The method of Head (1960) is an excellent candidate to calculate turbulent boundary layer development under a pressure gradient. This method uses the Von Karman integral momentum relation, the skin-friction correlation of Ludwieg and Tillmann (1949) and entrainment closure relations to numerically compute the boundary layer development. In these expressions the external velocity and its derivative are required, which can be modeled with the mass conservation relation when the plane diffuser angle φ is known. With the velocity distribution known, an initial boundary layer development is calculated. The boundary layer growth influences the velocity distributions by decreasing the effective cross-sectional area and thus five iterations are performed until the development is converged. It must be noted that the model is purely one-dimensional, and thus assumes the same turbulent boundary layer development on the plane diffuser as the test plate, as well as uniform conditions at each section. It does also not account for mass transfer through the gaps that are required for the DFM set-up (further discussed in Section 3.1.1). More information about the architecture of the algorithm is given in Appendix B.

Other than the ZPG cases FPGs and APGs are naturally of interest. To not grab the experimental pressure gradients from thin air, a reference airfoil case is considered to have an initial feeling of the values found over an airfoil. A NACA 2415 airfoil is chosen, flying at 250 m/s (Mach 0.85 at 11 km altitude) at C_l = 0.7 with a chord length equal to the test plate length (c = 0.631 m). Using XFOIL the pressure coefficients and the shape factor are computed over the airfoil surface. They are shown in Figure 3.7a and 3.7b.

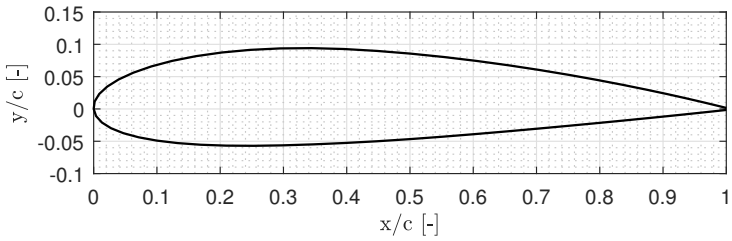

FIGURE 3.6: NACA 2415 airfoil.

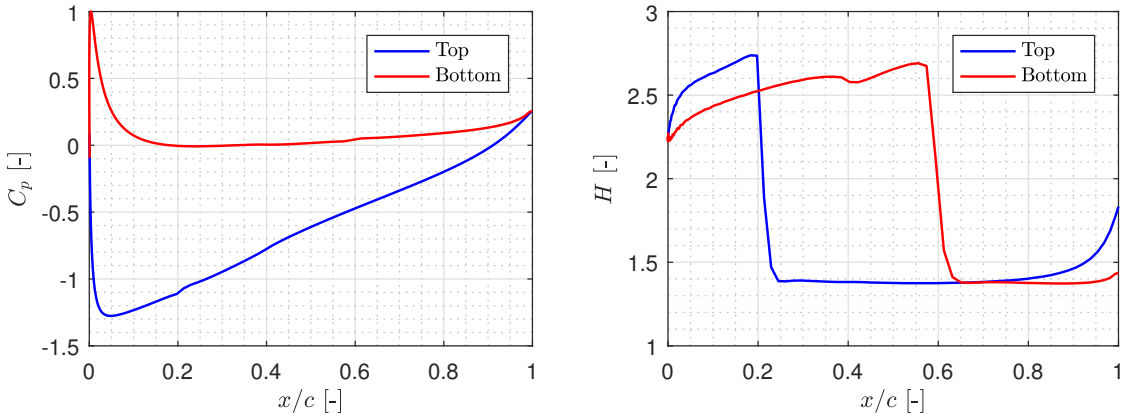

(A) Pressure coefficient

(B) Shape factor.

FIGURE 3.7: Flow properties around a NACA 2415 at C_l = 0.7 at Re_c = 1.11 × 10^7.

No forced transition is applied, such that a turbulent boundary layer starts at x/c = 0.2 on the top side and at x/c = 0.6 on the bottom side (observed from the sudden downward shift of the shape factor in Figure 3.7b). Focusing on the top side, a region of shape factors is

observed in which the shape factor stays around the ZPG value of 1.31. Between x/c = 0.7 and x/c = 1.0 the shape factor increases up to 1.83, indicating the effect of the pressure recovery (adverse gradient) at the rearward part of the airfoil. A C_l = 0.7 is chosen to resemble cruise conditions. As a result no boundary layer shape factors approaching separation (H = 3.0, as by White (2006)) are observed. Shape factors approaching separation generally occur when the airfoil is at high angles of attack and the boundary layer is nearing separation, but these are not the design conditions for which a drag reduction mechanism is optimized. It is furthermore observed from Figure 3.7a that a minimum C_p of about -1.26 is observed at x/c = 0.05 on the top side of the airfoil related to the largest velocity found on the airfoil. The shape factor and the pressure coefficient and their values found for this typical case will be the main aiming targets of the aerodynamic design. For the application of a FPG it is decided to constrain the final exit area to half of the initial inlet area. This is done to maintain the integrity of the test section and to force the bulk of the flow to leave through the end area instead of the side gaps.

The algorithm extracts the turbulent boundary layer properties at two specific locations, one at an upstream location at x = 0.150 m and one at x = 0.520 m, corresponding to the planned PIV and HWA measurement areas of the experimental campaign. After several user iterations the cases a test matrix was synthesized that suited the conditions found on the NACA airfoil, given in Table 4.7

TABLE 3.2: Simulated boundary layer development for a strong adverse and strong favorable pressure gradient and a zero pressure gradient.

			UPSTREAM (X = 150 MM)				DOWNSTREAM (X = 520 MM)			
$\mathbf{U_\infty}$ [m/s]	$\mathbf{Re_D}$ [10^4]	φ [°]	$\mathbf{U_e}$ [m/s]	δ_{99} [mm]	$\mathbf{C_p}$ [−]	**H** [−]	$\mathbf{U_e}$ [m/s]	δ_{99} [mm]	$\mathbf{C_p}$ [−]	**H** [−]
7	1.86	-13	7.7	28.0	-0.22	1.27	10.4	23.4	-1.20	1.24
15	3.99	-13	16.6	24.2	-0.22	1.27	22.3	20.5	-1.20	1.23
15	3.99	0	15.1	27.4	-0.01	1.31	15.3	32.4	-0.04	1.34
30	7.97	0	30.1	24.0	-0.01	1.31	30.5	28.9	-0.04	1.33
15	3.99	10	14.1	30.0	0.11	1.35	12.4	44.7	0.31	1.51
30	7.97	10	28.2	26.3	0.11	1.35	24.8	39.6	0.32	1.49

A negative deflection φ indicates a converging test-section. From Table 4.7 a strong favorable pressure gradient (SFPG) φ = -13° and a strong adverse pressure gradient (SAPG) for φ = 10° can be observed. The ZPG and SAPG cases are computed at 15 m/s and 30 m/s to examine the upstream Reynolds number effect. The SFPG is constrained to lower velocities, as the test section starts to bulge at increasing upstream velocities from 15 m/s.

Expected behavior is observed from Table 4.7. The shape factor decreases for the SFPG and increases for the SAPG, the boundary layer thickness decreases for a SFPG and increases for a SAPG, and the freestream velocity increases for a SFPG and decreases for a SAPG. For the ZPG case there is a slight acceleration of the flow due to the effective shape of the test section by the turbulent boundary layer thickness. The deflection angle for the SFPG case is chosen as to constrain the test section to half of its original area. A minimum C_p of -1.2 is found for this deflection, analogous to the peak pressure coefficient found for the NACA airfoil in Figure 3.7a. For the SAPG design case the shape factor does not approach separation values, but has a close value to the rearward part of the NACA airfoil observed in Figure 3.7b. It is furthermore observed that at the upstream position the changes to the turbulent boundary layer are not as profound as towards the end. These cases are then defined as the limiting

cases for the pressure gradients. Additionally two intermediate cases are discussed for the DFM campaign in Section 3.2 (the mild adverse and mild favorable pressure gradient) that have their deflection at half the limiting cases.

3.1.3 Nomenclature

Before transferring to the experimental descriptions, a note must be made about the nomenclature that is used to describe different flow cases. Throughout this report different configurations of velocity, pressure gradient, geometry and measurement location are given. Instead of using the full description of the case a straightforward abbreviation is used. For the direct force measurements, in which cases are repeated multiple times, this abbreviation exists out of the geometry:

- **[F]** flat plate,
- **[D]** dimpled plate,

pressure gradient:

- **[F2]]** strong favorable pressure gradient,
- **[F1]** mild favorable pressure gradient,
- **[Z]** zero pressure gradient,
- **[A1]** mild adverse pressure gradient,
- **[A2]** strong adverse pressure gradient,

followed by the occurrence N: the N'th measurement of that geometry and pressure gradient. *FZ1* then means a flat plate at a ZPG measured for the first time while *DF23* indicates a dimpled plate at a strong favorable pressure gradient measured for the third time. For the repeatability experiments, in which a ZPG case is considered and no dimpled plate is used, the additional prefix R[epeatibility] or [inter]C[hanged] is added. *RZ3* then indicates the third time that a ZPG flat plate is tested without opening the door (more explanation on the 'interchanged' definition of the repeatability cases is given in Section 3.2.5).

3.2 Direct force measurements

In this section an approach is described in which the entire drag coefficient of a test plate is measured by means of direct measurement of the drag force with a new flexure-based drag balance, where both the upstream Reynolds number and the pressure gradient are changed. Compared to a local measurement using PIV or HWA this gives an immediate direct measurement of the drag force and the effect of a dimpled surface. On of the primary aims during the experiment is to provide *consistency* to the experiment, as to exclude external interference on drag behavior other than the dimples. This section shall focus on the drag balance that is designed for the experiment and an experimental procedure that aims to provide the wanted consistency, but first a general description of the test set-up and its requirements are given.

3.2.1 General set-up

In Figure 3.9 the physical manifestation of the schematic blueprint in Figure 3.3 is shown. Since very small differences in drag are to be measured it is of paramount importance that the set-up is not changing during the experimental runs. Great care is taken to make sure that the set-up is as invariable as possible. To achieve this the different parts of the set-up are rigidly clamped to prevent movement due to outward disturbances. The drag balance is rigidly clamped to an X-beam base. The load cell is attached to a separate X-beam base, such that the load cell and drag balance are not in contact with one another other than at the interface between the test plate and the load cell. The load cell has a fixed position, and during the experiment detachment between the load cell and test plate is achieved by moving the test plate forward (due to flexibility of the drag balance) and subsequently anchoring the test plate. The clamping does not allow the drag balance displacement when the test plate is replaced, thus preventing potential misalignment of the force sensor between experiments that could occur when plates are being changed. The test section is clamped at the outlet to a heavy support structure, furthermore constraining movement. As the Plexiglas walls themselves are not very stiff additional stiffening is required in order to prevent bulging of the side walls during the experiment at larger velocities. With these structural efforts it is attempted to make the set-up as invariable as possible. The set-up is shown in Figure 3.9, from which it is furthermore observed that the test section is shielded by black screens to reduce disturbance from the outside environment.

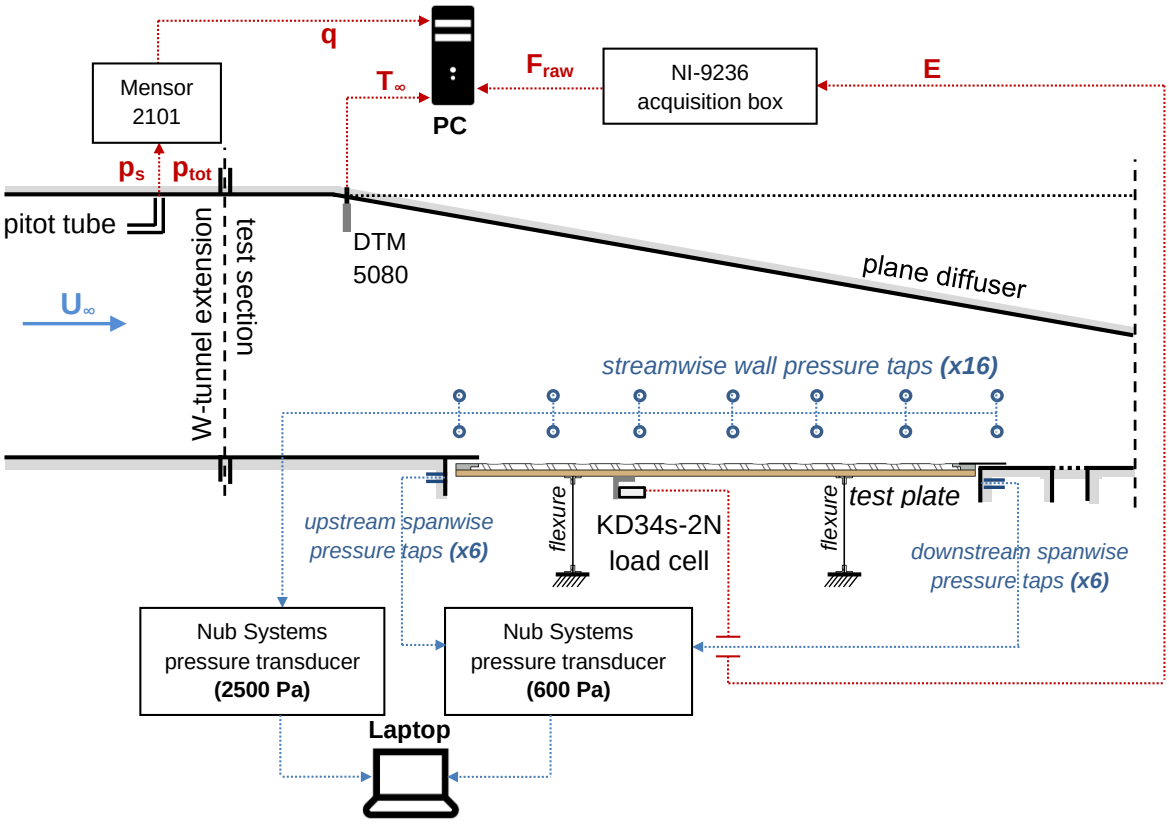

FIGURE 3.8: Schematic view of the measurement apparatus and the experimental set-up.

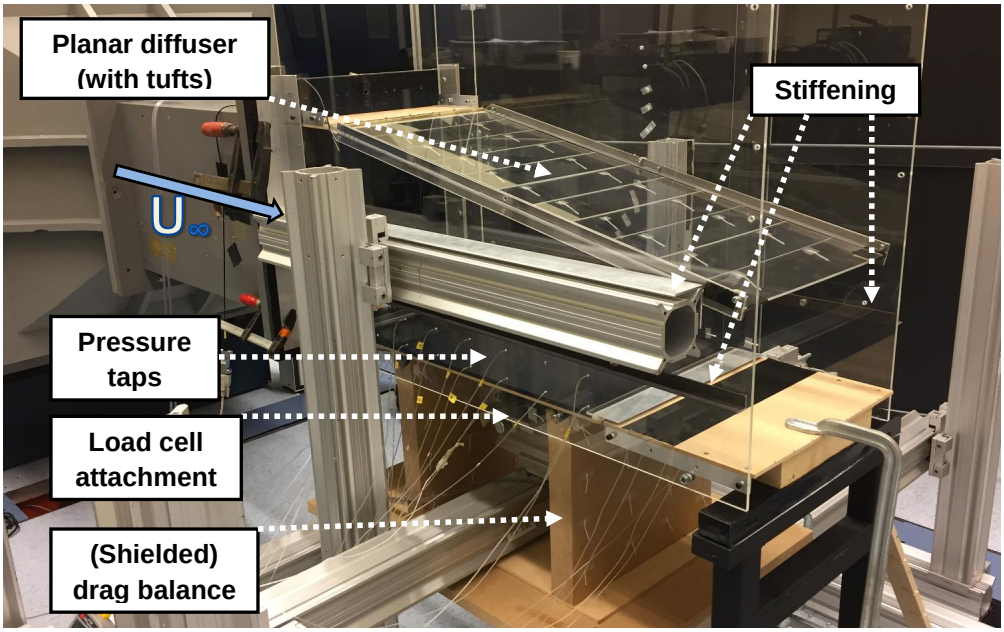

FIGURE 3.9: Experimental set-up in SFPG configuration. Screens placed near the entrance of the wind-tunnel hall to prevent disturbances.

A newly-designed drag balance based on flexures is used to measure the drag (which will be discussed in Section 3.2.3 in more detail). As the test plate is decoupled from the test section, flow is able to escape through the side gaps. To have a qualitative notion of how much flow enters or leaves the test-section when the wind-tunnel is operational, tufts are placed in streamwise direction just above the test plate surface. To prevent the occurrence of indeterminable components in the force signal due to flow impingement of this escaping flow on the flexures, the flexures are shielded. Tufts are furthermore added to this shielding to qualitatively study the flow below the test plate. As the test plate is decoupled from the test section the flow is smoothly guided from the test section to the test plate by means of a thin plastic strip at the test plate interface with the test section to avoid early separation due to a step (see Figure 3.10).

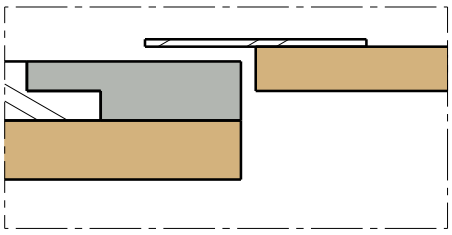

FIGURE 3.10: Upstream interface between the test plate and the test section. Inlet flow coming from the right. Thin plastic strip (not shown) at the leading edge is applied here to avoid early separation due to a step.

The load cell makes contact with the test plate through a small but rigid rod underneath the test plate (Figure 3.12). In order to prevent moments inside the force sensor due to misalignment of the frontal surface with the rod, a small bolt is added to the force sensor to make sure the raw measured force F_{raw} is distributed through the centerline of the force sensor (see Figure 3.11).

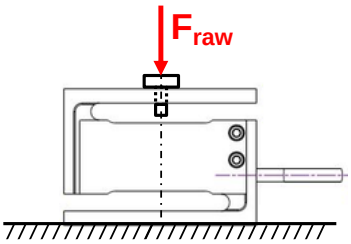

FIGURE 3.11: Force application to the load cell via a small bolt.

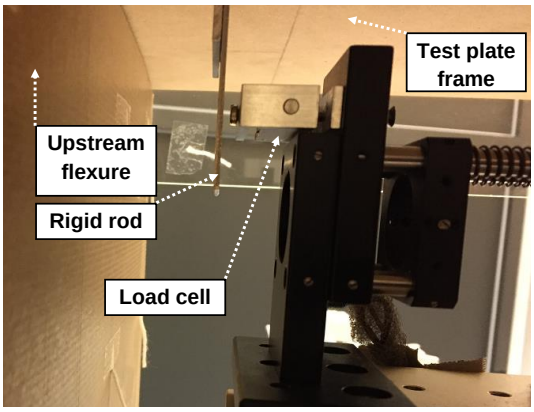

FIGURE 3.12: Rod-sensor interface underneath the test plate while in anchored 'resting' position.

The only movable part of the test section is then the section door, that needs to be opened in between experiments to change test plates. To check if this has any influence on the drag measurements, repeatability experiments are performed which are the focus of Section 4.2.5. Between experiments the force sensor is also allowed to 'rest'. This is mainly done to account for drift that was observed in the previous experiments of Van Campenhout (2016) and Van Nesselrooij (2015) after prolonged loading, but also to not overload the sensor when the plates are being changed. During resting the test plate is moved in upstream position (away from the force sensor, see Figure 3.12) and anchored to the test section wall by means of a pin. Another advantage of this is that the pre-loading force for each measurement run should be equal, thus further improving consistency.

As a pressure gradient is established over the plate, pressure differences start to arise at the start and the end of the plate. To quantify the effect of the pressure gradient on the measured raw force, the static pressure is also measured at the upstream and downstream gaps by means of pressure taps just before and behind the test plate beneath the flow domain. At each gap six pressure taps are placed with equal spanwise spacing.

3.2.2 Equipment

Other than the drag balance and the test-section other off-the-shelf hardware is required during the experiment. A sensitive force sensor is required to measure the force acting on the plate, as well as measuring apparatus to measure ambient and flow conditions during the experiment. An overview is presented in this section. In LABVIEW a program is available to the measured variables are digitalized into text files that can be further studied and processed.

Ruska 6200. The ambient pressure in the wind-tunnel room is read by the Ruska 6200 series. The Ruska 6200 has a stated accuracy of $\pm 0.01\%$ and a range of 0 to 1.31 bar. The Ruska 6200 is not digitally connected to the LABVIEW program, and thus the ambient pressure must be manually inserted into the LABVIEW program before each measurement run.

DTM 5080. The temperature of the flow is directly measured by the insertion of the DTM 5080 temperature sensor through a small gap at the top of the test section. The DTM 5080 by LKM Electronic has a stated accuracy of ± 0.02 degrees Celcius. Together with the dynamic pressure it is sampled at a 10 Hz frequency.

Mensor 2101. The atmospheric values measured from the ambient pressure and temperature sensors is coupled with the dynamic pressure measured by the Mensor 2101 to yield the flow velocity. The Mensor 2101 uses one port to measure the total pressure and one port to measure the local static pressure, both measured by means of a pitot tube. The difference between these is then the dynamic pressure. Using a LABVIEW program the the dynamic pressure is acquired together with the temperature at a sampling rate of 10 Hz. The Mensor 2101 has a stated accuracy of $\pm 0.03\%$ and is recently calibrated at the time of the start of the experiment.

KD34s-2N load cell The load cell used in this experimental investigation is the KD34s-2N load cell by ME-Meßsysteme (Figure 3.13). It is made of an aluminum alloy and has a mass of 30 g. The stated accuracy is 0.1% It has a nominal load of 2N, which when applied creates a 0.25 mm displacement inside the system, from which a force sensor stiffness k_c of 8,000 N/m can be deduced when a linear relation between force and deformation is assumed. The sampling frequency of the raw force F_{raw} can be adjusted in the LABVIEW program, and a sampling frequency of 10 KHz is chosen to capture a good range for performing an analysis of the frequency domain. The force sensor is connected to a National Instruments 9236 acquisition box which converts the voltage of the load cell into data files.

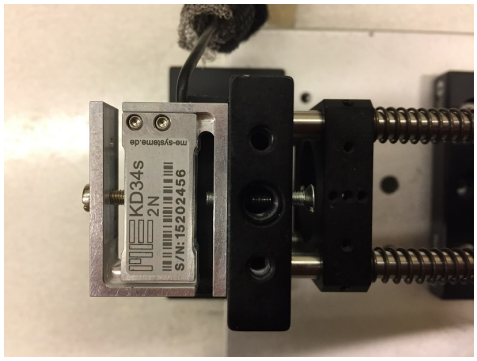

FIGURE 3.13: Top view of the KD34s-2N force sensor.

Nub Systems pressure transducer The static pressures are digitalized by a Nub Systems pressure transducer (Figure 3.14). This transducer is availabe in three ranges, 600 Pa, 2500 Pa and 6000 Pa. For the gap pressures small values are expected and thus the 600 Pa version is used for the upstream and downstream gaps. For the pressure gradients over the test plate larger values are expected, and thus the 2500 Pa version is used. The transducer is connected to a control unit which in turn is connected to a computer and subsequently read by a LABVIEW program. The pressure is measured at a sampling frequency of 2 KHz.

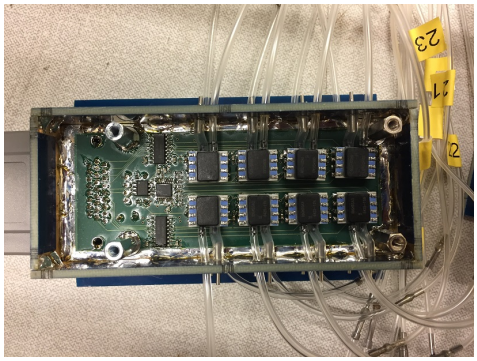

FIGURE 3.14: Opened Nub Systems pressure transducer with all the pressure transducer ports observable. Pressure adapters are used to transfer from a smaller tube to a larger tube.

3.2.3 Drag balance

In order to quantify the drag coefficient for both the flat and dimpled plate under different pressure gradients it is wanted to capture the drag force of the plate and accurately measure it with a force sensor (load cell). A novel *flexure*-based drag balance is presented in this section. A flexure is a thin plate that allows free movement in the streamwise direction but which still carries the weight of the plate. When the bending stiffness of the flexures is small compared to the load cell, most of the force in streamwise direction is captured by the force sensor. The advantage of a flexure-based drag balance it that is relatively simple. It requires no power supply, components are easily interchanged, and it does not require additional equipment like compressors that air bearings do require. Since the flexures are clamped, they have only one degree of freedom of movement. Since such a drag balance was not in existence for the current purpose, a new design was made for the current experiment. For an initial design the drag balance (Figure 3.15a) is simplified into a mass-spring system with two springs (Figure 3.15b): a spring that represents the load cell and a spring that represents the flexures.

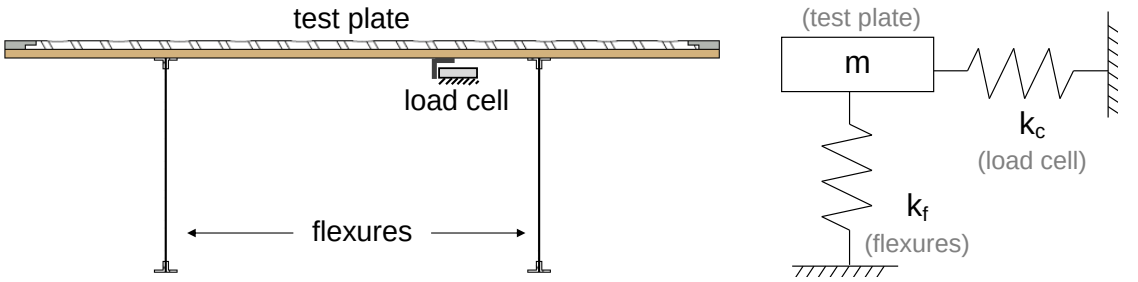

(A) Schematic side view. (B) Mass-spring representation.

FIGURE 3.15: Drag balance design.

Assuming a linear spring relation, the relation between an applied force and the displacement is given by Equation 3.1:

$$F = -kx \tag{3.1}$$

All springs are placed in parallel, meaning that the individual stiffness of two flexures can be summed up. In Figure 3.15b k_f represents the equivalent stiffness of the two flexure plates that carry the plate. From the specifications of the load cell it was derived that the maximum displacement of the force sensor is 0.25 mm at the nominal load. The stiffness k_c can then be computed to be 8,000 N/m, assuming a linear relationship between the load

and the displacement. This stiffness can not be altered, but the stiffness of the flexures is a choice of design. When a force is applied in the streamwise direction to the mass-spring system it is divided over both springs according to their stiffness. Since a flexure is naturally not capable of creating a voltage which can be read into a computer, it is of interest to have most of the force absorbed by the load cell. To this end a relatively high flexure efficiency η is wanted.

$$\eta = \frac{F_c}{F_{total}} = \frac{k_c}{k_c + k_f} \tag{3.2}$$

For practical and stability reasons it is wanted that the test plate moves back to an equilibrium position when an applied load is removed. To achieve this the flexures are clamped both at the base and the head by L-profiles and bolts. Would this not be the case, the test plate would collapse to one side during handling and transport, and could possibly overload the force sensor during the experiment. To compute the stiffness of a clamped beam standard beam theory is used. To account for the clamping on both sides of the beam, the flexure stiffness is approximated by Equation 3.3, where a factor of 12 is used to account for the clamping. For a high flexure efficiency it is observed from Equation 3.2 the stiffness should be very low ($k_f \rightarrow 0$), but this will lead to failure due to buckling when a small load is applied. For the computation of the critical buckling force Equation 3.4 is used, where K = 1.2 is used to account for the clamping.

$$k = \frac{12EI_z}{L^3} \tag{3.3}$$

$$F_{crit} = \frac{\pi^2 EI_z}{(KL)^2} \tag{3.4}$$

Two main loads are identified that act on the flexure system: the mass of the test plate and the pressure force that exists due to the application of a pressure gradient. To get this pressure force the pressure gradient (computed by the algorithm described in Section 3.1) is integrated over the test plate. This force is then included in the static equilibrium to compute the forces in the flexures. This pressure gradient will induce a force at a location that is downstream relative to the center of gravity. For an increasing pressure over the plate the buckling constraint becomes increasingly important. After performing several iterations the design parameters of Table 3.3 were determined to be suitable to prevent buckling while also allowing for a maximum efficiency η. More information on the static equilibrium analysis that was used to determine the forces in the flexures is presented in Appendix B.

TABLE 3.3: Flexure design parameters.

Parameter	**Symbol**	**Value**	**Unit**
Flexure stiffness	k_f	598	N/m
Load cell stiffness	k_c	8,000	N/m
Equivalent stiffness	k_{eq}	8,598	N/m
Flexure thickness	t_f	1	mm
Flexure length	L_f	0.35	m
Flexure width	b_f	0.35	m
Upstream flexure distance	s_1	0.18	m
Downstream flexure distance	s_2	0.58	m
Flexure efficiency	η	0.93	-
Buckling ratio	F_2/F_{crit}	0.95	-

A computed efficiency of 93% then means that 93% of the applied force is captured by the force sensor. Using a calibration wheel and a set of small weights below 200 g the set-up is calibrated to check if the same efficiency is represented in the force signal. The calibration wheel uses knife edges such that internal friction is reduced, such that the gravity force of the weights is efficiently transferred to the flexure system. From the calibration plot in Figure 3.16 it is then observed that the drag balance returns 92% of the force of the weights into the load cell, close to the computed value of 93%.

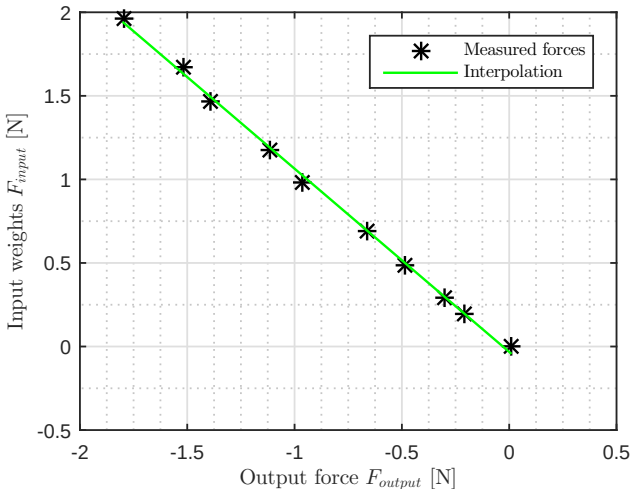

FIGURE 3.16: Flexure system calibration. Note that the signal returns negative values for compression.

3.2.4 Data corrections

As the pressure is changing when a pressure gradient is applied to the test section, this creates a pressure difference between the leading edge and trailing edge that is not part of the skin-friction force. This pressure force needs to be determined using the pressure taps and subtracted from the raw measured force. Other than the pressure force corrections, an additional study is performed to determine the other proper corrections to the force signal. For this the set-up flexure balance was moved to the Open Jet Facility (OJF) air-conditioned control room (Figure 3.18). Using the air-conditioning it is attempted to model the change of the ambient temperature throughout the day in the wind-tunnel and its effect on the force signal. Instead of an aerodynamic loading, calibration weights were used in combination with the knife-edge calibration wheel described in Section 3.2.3. Instead of maintaining the time planning of the measurement plan, the force signal is measured for some time before and after the start and end of the timing presented in the measurement plan. To ensure a consistent replication of the actual experiment, the same time cycles of 30 s intervals and 10 s measurement time were maintained. The raw measured force signal for one of these measurements is shown in Figure 3.17.

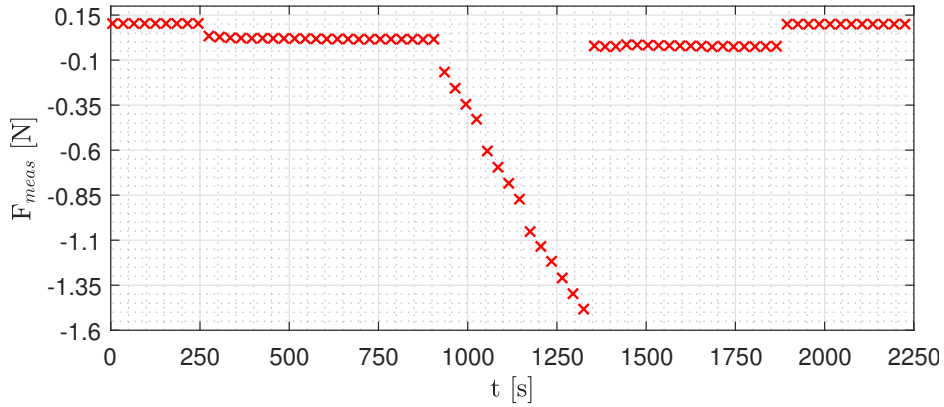

FIGURE 3.17: Full run during sensitivity study. Raw measured force shown, which is negative for compression.

Five distinct regions are observed: a pre-load cell attachment phase, post-load cell attachment phase, loading phase, pre-load cell detachment phase and a post-load cell detachment phase. Five temperature distributions are considered in this study to simulate the change in temperature observed throughout the day during the actual experiment. It is observed from Figure 3.19a that the air-conditioning system does not keep a constant temperature, but each subsequent temperature distribution is higher than the previous distributions. The raw measured forces are observed in Figure 3.19b. They do not have the same force magnitude, indicating that there is an effect on either the experimental set-up or the force sensor, possibly due to temperature differences. This presumed temperature dependency is discussed in further detail in Section 3.2.6.

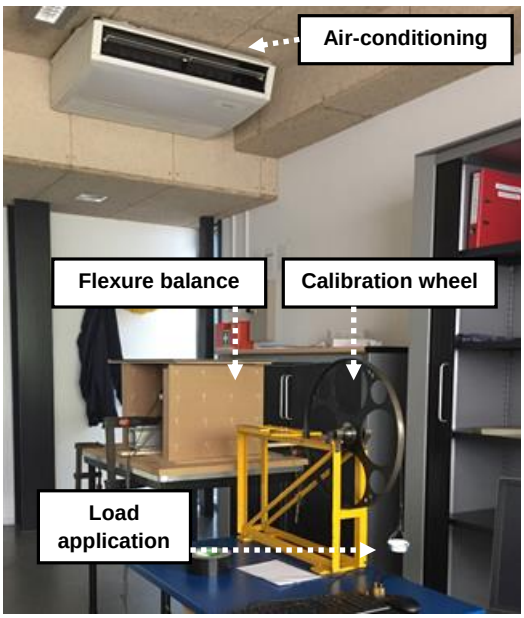

FIGURE 3.18: Flexure balance set-up in the OJF control room.

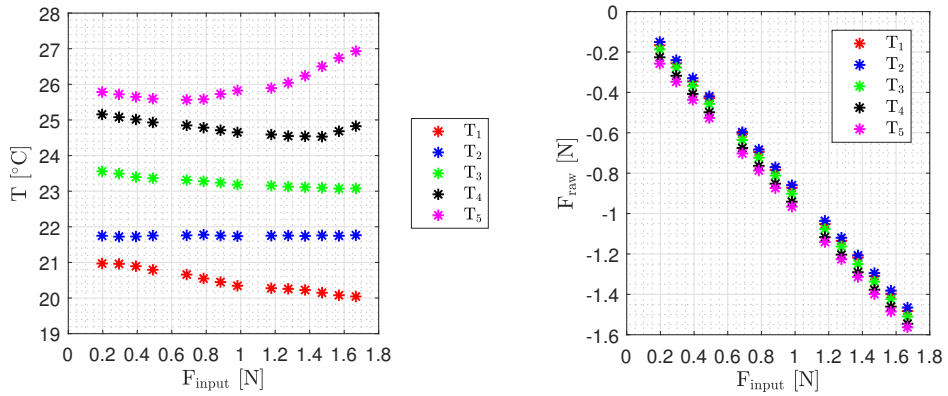

(A) Temperature distributions. (B) Force distributions.

FIGURE 3.19: Parameters tracked during the temperature sensitivity study.

During the experiment the aerodynamic forces applied to the load cell are not known. In this study the 'aerodynamic forces' are known, as they are the calibration weights. As the exact load of the weights is known, the results are used to determine the required force signal corrections to arrive at the same measured values.

Null-force. The first correction was utilized by both Van Nesselrooij (2015) and Van Campenhout (2016), who observed the a shift in null-force between the start and the end of the loading. To combat this they applied a force correction in which the force signal at a step i is corrected by adding the measured null force shift ΔF scaled by the force measured that step divided by the largest force measured in the calibration.

$$F_i = F_i - \frac{F_i}{F_{max}} \Delta F_0 \tag{3.5}$$

Although this seems a physically justified correction, from Figure 3.5 it can be observed that towards the higher steps inside the calibration the force signals start to diverge. That is why this correction is not used for the DFM campaign.

Temperature. As temperature is changing throughout the experiment, it is also attempted to apply a temperature correction with Equation 3.6. In this correction a procedure analogous to Equation 3.5 is chosen, but instead using scaling based on the force of each step, the null force is scaled by the temperature change at each measurement step normalized by the total temperature change ΔT between the start and end of the weight-loading period.

$$F_i = F_i - \frac{T_i - T_0}{\Delta T} \Delta F_0 \tag{3.6}$$

Looking at Figure 3.20c it is observed that just as for the null force correction the forces start to diverge towards the end of the calibration steps. Therefore, this correction is discarded for the DFM campaign.

Subtraction of initial force. As the first value before the load application is the 0 g case, the initial loading at the end of the value before the first loading is subtracted from the force signal such that the resulting force represents the actual loading. For the different temperature cases the effect of this is shown in Figure 3.20b. Compared to both the null-force corrections and the temperature corrections this shows the best representation of the calibration weights that are used. Due to this fact the initial force subtraction is the correction that is applied for

DFM campaign.

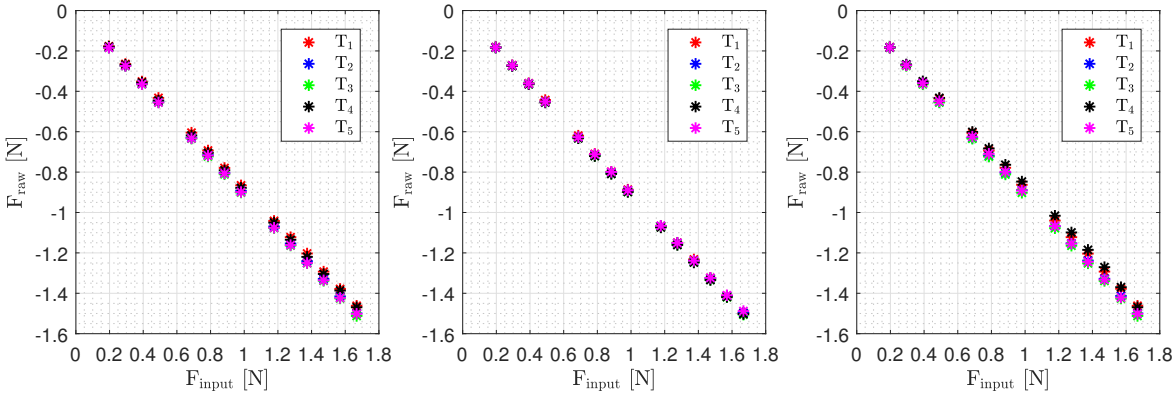

(A) Calibration with null-force shift correction. (B) Calibration with value before first loading subtracted. (C) Calibration with temperature correction.

FIGURE 3.20: The effect of different force corrections.

Pressure. Another force correction needs to be applied that is not related to the sensitivity analysis above. The load cell measures a raw force F_{raw}. This raw force is not the skin-friction force, that is of interest in this study, but also contains a pressure component that exists due to pressure differences in the streamwise direction. The pressure measurements thus have a twofold goal. First of all they are used to quantify the pressure gradient over the test plate but the pressure taps between the upstream and downstream gaps are used to distill the skin-friction force by subtracting the pressure force difference ΔF_p that exists at these upstream and downstream gaps. The pressure force on each side is computed by the summation of each measured pressure multiplied by the area on the test plate which it acts, which is mathematically expressed as:

$$F_p = \sum_{i=1}^{6} p_i A_i \tag{3.7}$$

There are six pressure taps at both the upstream and downstream gap (as shown in Figure A.6a and A.6b). Using the pressures measured at the downstream and upstream gap and the area of the front and rear part of the test plate, the effective pressure force difference ΔF_p can be computed and subtracted from the the raw force F_{raw} to yield an effective drag force F_D. The pressure force calculation for one side is shown schematically in Figure 3.21.

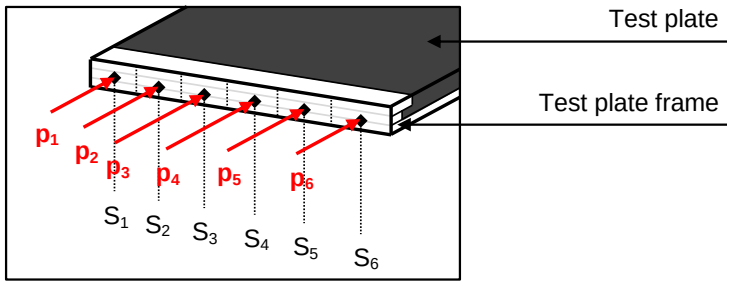

FIGURE 3.21: Calculation of F_p on the test plate upstream/downstream edge from multiple pressures p_i and areas S_i. Pressures represented by arrows.

3.2.5 Measurement plan

It is wanted to have a high-quality experiment by increasing consistency and repeatability. Next to the measures taken to ensure the invariability of the set-up, a consistent measurement plan is used. One pressure gradient case is considered each day, such that possible movement from the adjusting of the planar diffuser does not influence subsequent measurements. The first two days are used to setup the wind-tunnel, performing the calibration procedure and defining the velocity as a function of RPM. The latter is done to quickly change the wind-tunnel velocity during the measurement runs. This table is shown in Appendix C.

The general approach of the measurement runs is the *sandwich* principle and follows previous best practices. This approach means that the drag performance of a dimpled plate is compared to the previous and subsequent flat plate measurement, creating a measurement schedule where the flat plate and the dimpled plate are interchanged. Using the sandwich principle it is attempted to cancel out possible differences in temperature, pressure and the set-up that arise throughout the day. differences The drag differences for each sandwiched case is then averaged to yield an average drag change ΔC_D. This schedule is then given in Table 3.4.

TABLE 3.4: Measurement schedule. Off-days and first two days are omitted.

	DAY							
Goal	Repeat. 1	Repeat. 2	ZPG	SFPG	SAPG	MFPG	MAPG	Vibrations
RUN	**Day 3**	**Day 4**	**Day 5**	**Day 6**	**Day 7**	**Day 8**	**Day 9**	**Day 10**
1	RFZ1	CFZ1	FZ1	FF21	FA21	FF11	FA11	VZ1
2	RFZ2	CFZ2	FZ2	FF22	FA22	FF12	FA12	VF2
3	RFZ3	CFZ3	DZ1	DF21	DA21	DF11	DA11	VA2
4	RFZ4	CFZ4	FZ3	FF23	FA23	FF13	FA13	VF1
5	RFZ5	CFZ5	DZ2	DF22	DA22	DF12	DA12	VA1
6	RFZ6	CFZ6	FZ4	FF24	FA24	FF14	FA14	
7	RFZ7	CFZ7	DZ3	DF23	DA23	DF13	DA13	
8	RFZ8	CFZ8	FZ5	FF25	FA25	FF15	FA15	
9	RFZ9	CFZ9	DZ4					
10			FZ6					

As the sandwiching of plates requires the opening of the set-up door, the first two days of actual measuring (days 3 and 4 in Table 3.4) are composed of repeating the flat plate measurements in the ZPG configuration. The first day it is examined what the effect is on the drag behavior when the flat plate measurements are performed without opening the door, thus making no changes to the test section. The second day the flat plate is taken out, and then put back in again, and thus the effect of opening the door is examined. For the first day the prefix R- is used, and for the second day when interchanging the plate the prefix C-. In this way the effect of the only non-invariable part of the set-up is quantified. Then the first measurement of the dimpled plate is performed for the ZPG, followed by the SFPG, SAPG, and two intermediate pressure gradients at half the deflection angle of the strong pressure gradients: the *mild FPG* for which φ = -6.5° (MFPG) and *mild APG* for which φ = 5° (MAPG). Each pressure gradient is measured each day. Each day is furthermore initiated with a prerun to 'awake' the force sensor after a night of rest. It is furthermore observed from Table 3.4 that a total of three dimpled plates are tested each day, with the exception of the ZPG case

where logistics allowed to measure four dimpled plates.

FIGURE 3.22: Pin in anchored position. The setup is held in a forward position preventing contact with the load cell.

Each measurement cycle takes exactly one hour. During the measurement cycle use is made of a checklist to ensure consistency of each cycle. Using a stopwatch the time is reset at the start of each measurement run. In the first 25 minutes the test plate is replaced, while the pin is attached to anchor the test plate and to prevent overloading of the force sensor. After 25 minutes the pin (Figure 3.22) is removed, allowing the force sensor to move against the rod underneath the test plate. Then a period follows in which the logistical tasks as measuring the ambient conditions and updating the file names are performed. At the 33 minute mark the LABVIEW algorithm is toggled to start saving results. Instead of a continuous signal, a timer is set on the LABVIEW program that measures the velocity and the load cell simultaneously at 30 s intervals for a duration of 10 s. The wind tunnel is started at 35 minutes and 40 seconds, before which it has read 5 consecutive null-force measurements without any aerodynamic loading. As previous investigations by Van Nesselrooij (2015) have shown the low Reynolds number regimes to have a large root-mean-square deviations, the velocities under 10 m/s are not measured for the DFM campaign. During the run the wind-tunnel is set as soon as the previous measurement has ended, allowing for 20 s of adapting the upstream velocity. Then a measurement of 10 s takes place of the drag force, when the freestream velocity has set. After a full wind-tunnel run the null-force is measured for another 10 consecutive times. The pin is attached at 55 minutes, allowing the force sensor to rest a consistent 30 minutes between each measurement run. The checklist contains additional tasks like set-up integrity checks and is given for the ZPG case in Appendix D.

3.2.6 Temperature sensitivity

When the set-up is moved against the set-up a drift in the force signal is observed while no external load is applied. In this section it is investigated if this drift has its origin in the set-up or the force sensor. For the drift analysis of the set-up the same set-up is used as depicted in Figure 3.18. The force is measured continuously and averaged for each 15 s for approximately an hour. After toggling the measurement the set-up is moved against the load cell at 3 minutes and the drift is subsequently measured for 30 minutes. A total of six temperature and force distributions are captured and show in Figure 3.23a.

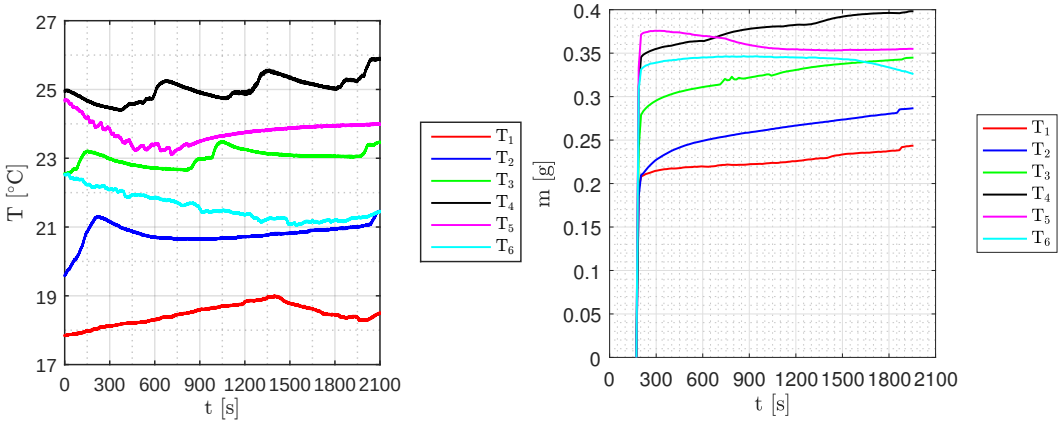

(A) Calibration with null-force shift correction.

(B) Calibration with value before first loading subtracted.

FIGURE 3.23: Experimental set-up drift.

After the drag balance moves against the load cell it is observed that a drift starts to appear, indicating that an increasing load is applied to the load cell. This load appears to be temperature dependent, as increasing the temperature also increases the load perceived by the load cell. In order to locate a probable source for the thermal expansion of the set-up when it makes contact with the load cell the thermal expansion due to a temperature difference ΔT is considered:

$$\frac{\Delta L}{L_0} = \alpha \Delta T \tag{3.8}$$

To determine a probable length scale of a segment of the test set-up, the test set-up is assumed to be a rod of characteristic length L_0, see Figure 3.24. A change in temperature ΔT results in a thermal expansion, which then creates an extra force ΔF measured by the load cell. As the stiffness of the load cell is known, as well as the temperature and force change from Figure 3.23, the characteristic length can be determined for a first-order estimate.

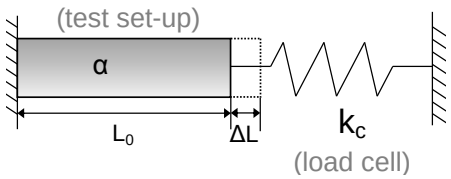

FIGURE 3.24: Thermal expansion and the load cell.

Rewriting the spring-displacement equation in to Equation 3.8 then yields Equation 3.9. The thermal expansion coefficient $\alpha = 23 \times 10^{-6}$ m/(m·K) for aluminum is used, as most materials in the balance are made of aluminum.

$$L_0 = \frac{\Delta F}{\alpha k_c \Delta T} \tag{3.9}$$

The thermal expansion is determined at two time instants at t = 800 s and t = 1500 s for all six measured temperature- and force distribution. For six distributions this then leads to 10 lengths L_0. Averaging all found results leads to an average L_0 = 0.21 m. This is a physical distance that however can not be attributed to any distance in the set-up.

The final temperature sensitivity experiment is performed by applying a weight to the load cell itself without any experimental set-up coming in between. Just as for the set-up drift the

weight is applied for 30 minutes. Two weights of 10g and 50g were used. The temperature was regulated by setting the air-conditioning to both its minimum and maximum level. The temperature distributions for both this low and high temperature are given in Figure 3.25.

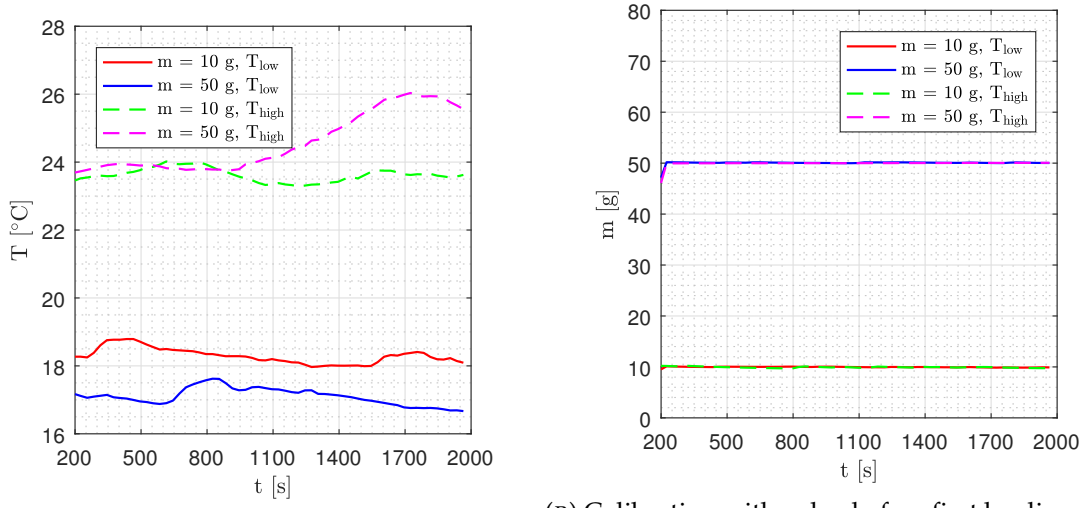

(A) Calibration with null-force shift correction.

(B) Calibration with value before first loading subtracted.

FIGURE 3.25: Load cell drift.

There is an offset between the the two temperature distributions for both the high temperature T_{high} and the low temperature T_{low} considered in this comparison, since the temperature can not be uniformly regulated in the room. In Figure 3.25b the raw force is converted into a mass value by dividing by the gravitational constant to check if the force accurately represents the masses that are applied to the load cell. Compared to the drift analysis of the drag balance set-up it can be found that there is no drift as a function of time, and no effect of temperature. The effect of both a high and low temperature does not have a noticeable effect on the values measured by the load cell. This leads to the conclusion that the drift is caused by the expansion of the experimental set-up.

3.3 Particle image velocimetry

The second research question attains to the possible cause of drag reduction by a dimpled surface. Whereas the DFM campaign quantifies if such a drag reduction exists, it does not point into the direction of a cause. To this end a PIV campaign is performed to acquire quantitative information of the flow in the vicinity of the wall. From literature it is known that drag reducing methods have several similar characteristics: an upwards shift of the logarithmic layer, a decrease in Reynolds shear stress and a decrease of turbulence intensity. Combined with the HWA campaign discussed in Section 3.4, the PIV campaign is used to see if the same drag-reducing behavior is represented in the turbulent boundary layer boundary layer characteristics of a dimpled surface.

3.3.1 Experimental set-up

PIV is a non-intrusive measurement technique. Particles are injected into the flow and using a light source the particles are illuminated. The particles are then captured at the start and end of a short interval by an image acquisition system. The images are then processed

using a cross-correlation algorithm, where the displacement of the particles between the two snapshots and the pulse time separation are then used to construct the velocity field. This is schematically shown in Figure 3.26.

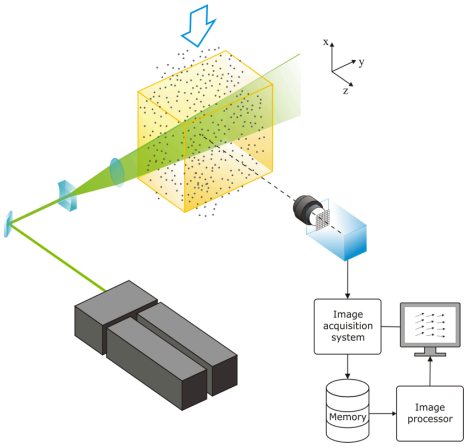

FIGURE 3.26: Schematic set-up of an exemplary PIV measurement system by Scarano (2013).

Several forms of PIV are available depending on the velocity components that need to be captured. Observing Equation 2.5 it can be concluded that the streamwise skin-friction distribution is only dependent on the streamwise velocity u and the wall-normal velocity v. To capture these velocity components *planar* PIV is chosen to be suitable to investigate the required turbulent boundary layer properties.

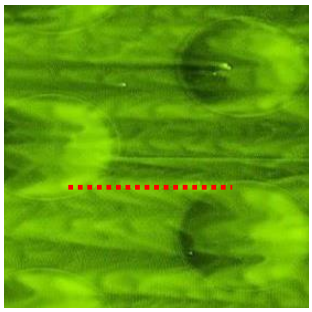

FIGURE 3.27: Location of maximum shear identified by Van Campenhout (2016) in oil flow visualization.

In previous research it is postulated that the drag reduction by a dimple is caused by the same turbulent structure inhibiting mechanism as for the oscillating wall. Van Campenhout (2016) and Tay et al. (2015) showed that this wave has it highest spanwise velocity between the dimples (Figure 3.27). As this is the region where the highest spanwise velocity is induced, this region is targeted in the PIV campaign. As the skin-friction coefficient generally decreases in the downstream direction it is of interest to see if the drag reduction is primarily attained in the upstream or downstream portion of the test plate. To this end two field of views are considered near the wall, one at x = 150 mm and one at x = 520 mm measured from the leading edge. This location then corresponds to the location of the oscillation between the fourth and fifth dimple row and between the fourth and fifth row before the trailing edge.

The pressure gradient cases described in Section 3.1.2 are considered to determine the PIV experimental settings, as they are conveniently computed at the wanted measurement locations between the dimples. As a ZPG or APG boundary layer is expected to grow an additional field of view is added to capture the full boundary layer at x = 520 mm, which overlaps with FOV 2 to allow coupling of both FOVs. At the same time this field of view can be used as a check that the flow is actually accelerating or decelerating. The aerodynamic algorithm computes the freestream velocity at each station (the maximum velocity in the turbulent boundary layer) which is used to compute the expected Δt camera pulse separation for each FOV and pressure gradient such that a maximum 10 pixel displacement is found for the particles (Table 3.6). Three FOVs can be identified, which are schematically shown in Figure 3.28 and tabulated in Table 3.5.

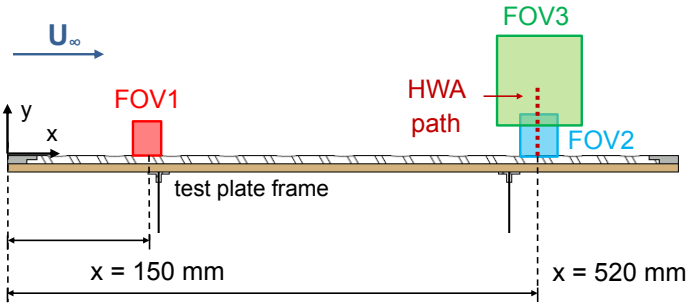

FIGURE 3.28: Location of FOVs and the HWA path on the test plate.

TABLE 3.5: Planar PIV configuration for the experiment.

FOV [-]	**Camera** [-]	**x** [mm]	**A** [mm×mm]	**f** [mm]	**M** [-]	$\mathbf{d}_o$ [m]
1	LaVision Imager Intense	150	22.5×30	105	0.36	0.40
2	PCO Sensicam	520	25×33	105	0.39	0.37
3	LaVision Imager Intense	520	83×110	60	0.11	0.62

TABLE 3.6: Pulse separation times Δt used for the PIV campaign based on aerodynamic algorithm.

			FOV 1		FOV 2		FOV 3	
$\mathbf{U}_\infty$ [m/s]	**Case** [−]	φ [°]	$\mathbf{U}_e$ [m/s]	Δt [μs]	$\mathbf{U}_e$ [m/s]	Δt [μs]	$\mathbf{U}_e$ [m/s]	Δt [μs]
7	SFPG	-13	7.7	28	10.4	23	10.4	75
15	SFPG	-13	16.6	13	22.3	11	22.3	35
15	ZPG	0	15.1	14	15.3	16	15.3	52
30	ZPG	0	30.1	7	30.5	8	30.5	26
15	SAPG	10	14.1	15	12.4	19	12.4	63
30	SAPG	10	28.2	8	24.8	10	24.8	32

The cameras that were utilized have a pixel size of 6.45×10^{-6} m for an area of 1376 by 1040 pixels. FOV 1 and FOV 2 are sampled into 1000 image pairs at a frequency of 5 Hz. This low acquisition frequency means that the flow is not time-resolved, and thus is not suitable for time-resolved turbulence development. FOV 3 has to capture less important turbulent structures (namely at the outer layer of the turbulent boundary layer), and thus

300 image pairs are taken for FOV 3. The particles are captured using three cameras (Figure 3.29), which are placed at a distance d_o from the field of view. The seeding particles for the experiment are provided by a Safex fog generator and have a typical diameter of 1 μm. The light source that is used to illuminate the particles is the Spectra Physics Quanta-Ray PIV-400 laser, which is a Neodym-YAG laser with a repetition rate of 10 Hz, maximum pulse energy of 400 mJ, pulse duration of 6 ns and a wave length of 532 nm. The cameras and the laser are controlled by a programmable timing unit (PTU), that is connected with the PIV software DaVis 8.1 by LaVision. The cross-correlation is performed in DaVis 8.1, and then exported into data files that can be further analyzed.

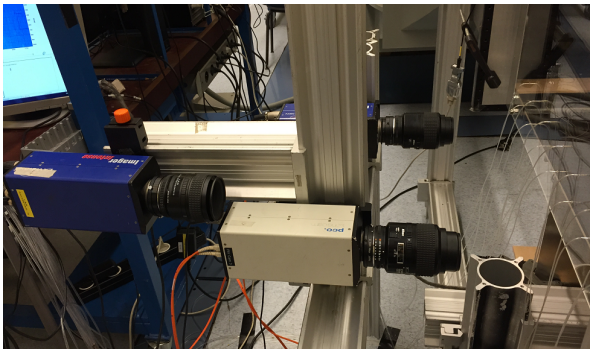

FIGURE 3.29: PIV camera set-up.

3.3.2 Processing

Within DaVis several steps are taken to arrive at a physical flow velocity field that can be further analyzed. The sequential steps are discussed here.

Calibration. First a calibration is performed in order to allow the algorithm to couple particle displacement to an actual physical distance. To this end a calibration plate with millimeter paper is used to calibrate the image pairs.

Pre-processing. Before the velocities are calculated by DaVis the quality of the images can be improved to yield flow fields with less outliers. To this end several operations are performed within DaVis to increase the quality of the raw snapshots. In Figure 3.30a a raw image is presented of a small area close to the wall. The following operations are then performed:

- Subtracting the minimum. (Figure 3.30b) To delete the noise from the background of each snapshot, the minimum of all the snapshots is computed by DaVis and subsequently removed from each individual snapshot. The cross-correlation algorithm can give erroneous results when stationary objects in the background interfere with it, as the velocity should be purely be computed from the displacement of the particles.
- Division by the average. (Figure 3.30c) The values show by DaVis for each snapshot show the relative intensity values of each particle. By computing the average and dividing by it the pixel intensity between each particle is normalized, leaving a more equalized snapshot. To have sufficient pixel intensity after division by the average, the image is multiplied by a large integer value beforehand.

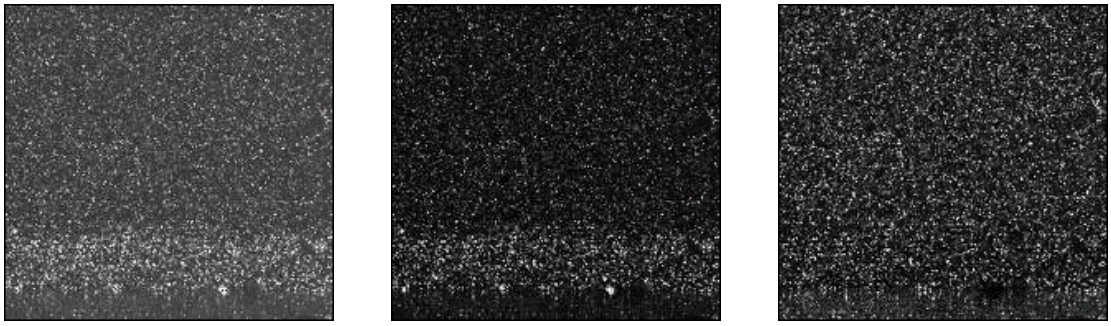

(A) (B) (C)

FIGURE 3.30: PIV pre-processing steps.

Correlation. It is wanted to have a sufficient resolution to capture the turbulence scales as much as possible. An iterative cross-correlation is performed in which an initial iteration is performed with a square interrogation window of 96×96 pixels with an overlap of 50%. Three iterations are then performed with a 32×32 4:1 elliptical interrogation window, as the mean velocity is expected to change the most in the wall-normal direction. For FOV 3 a 96×96 square interrogation window is taken. Eventually a vector spacing of 0.17 mm (5.8 vectors/mm) is found for FOV 1, 0.19 mm (5.2 vectors/mm) for FOV 2, and 1.9 mm (0.5 vectors/mm) for FOV 3.

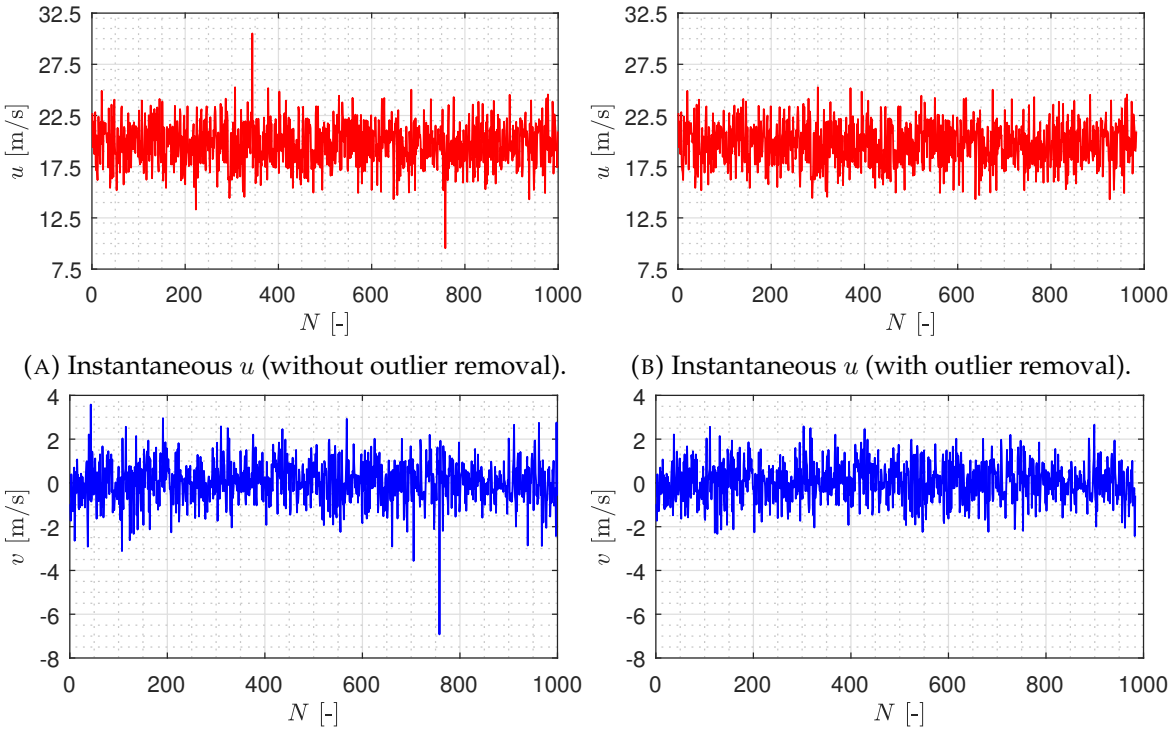

(A) Instantaneous u (without outlier removal).

(B) Instantaneous u (with outlier removal).

(C) Instantaneous v (without outlier removal).

(D) Instantaneous v (with outlier removal).

FIGURE 3.31: Custom MATLAB outlier removal algorithm example.

Post-processing. As a *quadrant analysis* is to be performed on the Reynolds stress, it is chosen to perform the post-processing of the velocity fields computed by DaVis in a MATLAB algorithm so that the instantaneous values can be split into quadrants and greater user control is permitted. As outliers negatively influence the computation of the mean Reynolds stress the first step is to remove the outliers in the velocity fields. The fields are loaded into

MATLAB, then the mean velocity fields for the horizontal and vertical velocity are computed by taking the mean of each original velocity field. The instantaneous fluctuation fields are then computed by a subtraction of the mean on each original flow field. As a turbulent flow is considered, the instantaneous fluctuations in each point resembles a stochastic signal (Figure 3.31a). An outlier is identified as a point that has a magnitude higher than three times the standard deviation of this signal, and is then subsequently removed (Figure 3.31b). As the number of samples is important in the computation of the uncertainty, the number of samples N is adjusted for the outlier removal in that point.

Before the required turbulent boundary layer properties are extracted, FOV 2 and FOV 3 need to be coupled to one another. FOV 2 and FOV 3 are not captured simultaneously due to differences in Δt, and thus it is not possible to cross-correlate each instantaneous velocity field. Instead an approach is taken in which the mean properties of the field are merged by a curve-fitting process. This is schematically shown in Figure 3.32. Due to the calibration it is known where the profile in FOV 2 (d_2) resides in FOV 3 (d_1+d_2), thus the relative position of the measured boundary layer profile in FOV 2 can be determined in FOV 3. The mean velocity at the bottom of FOV 3 is known, and the top velocity in FOV 2 is known. Using a least-squares curve-fit the relative distances between FOV 2 and FOV 3 is then calculated.

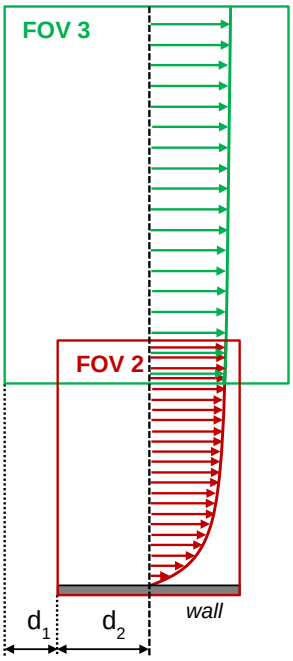

FIGURE 3.32: Merging of FOV 2 and FOV 3 in the MATLAB algorithm.

3.4 Hot-wire anemometry

To provide another quantification of the turbulent boundary layer the hot-wire anemometry technique is used. A hot-wire is a thin and fragile wire that makes use of heat transfer to determine the flow velocity of a fluid. A hot-wire makes use of the principle that heat is convected by the passing of a fluid around it. As the electrical current of a hot-wire is connected to the temperature by dissipation (Joule effect), energy transfer to keep the temperature (or the electrical current) constant can be used to connect the electrical properties to the flow properties.

In constant temperature anemometry (CTA) the temperature of the wire is kept constant by a variable current through the wire using a Wheatstone bridge. In equilibrium, the heat production is equal to the loss of heat. The rate of change of the thermal energy is then equal to the power generated by the Joule effect minus the heat transfer to the surroundings, which next to convection consists of conduction and radiation. This can be mathematically expressed as:

$$\frac{\mathrm{d}e_{th}}{\mathrm{d}t} = W - Q_{conv} - Q_{rad} - Q_{cond} \tag{3.10}$$

In equilibrium, assuming that radiation and conduction are negligible, the heat production of the Joule effect is equal to the energy that is convected:

$$W = Q_{conv} \tag{3.11}$$

$$I^2 R_{wire} = \frac{\mathrm{Nu} A k_f}{d}(T_{wire} - T_\infty) \tag{3.12}$$

where the following terms are defined:

- I the current through the wire,
- R_{wire} the resistance of the wire,
- Nu the Nusselt number,
- A the exposure area of the wire through which the heat transfer takes place,
- d the diameter of the wire,
- k_f the conductivity of the fluid,
- T_{wire} the temperature of the wire,
- T_∞ the upstream velocity.

White (2006) describes the relation between the Nusselt number Nu and the Reynolds number around an infinite cylinder. Substituting this relation into Equation 3.12 leads to King's law (Equation 3.14):

$$\mathrm{Nu} = a_1 + b_1 \mathrm{Re}^n = a_2 + b_2 U^n \tag{3.13}$$

$$I^2 R_{wire}^2 = E = \sqrt{(T_{wire} - T_s)\,(a_3 + c_3 U^n)} \tag{3.14}$$

where a_3, b_3 and n are constants.
For a CTA system the value for $\mathrm{T_{wire}}$ - T_∞ is a constant, and thus the calibration procedure only requires the voltage and the velocity to acquire the calibration constants c_1 and c_2. For a single wire Equation 3.14 does not take into account the direction of the wire-normal flow. Thus, the measured velocity is equal to the result wall-normal and streamwise velocity. As the streamwise velocity is considerably higher than the wall-normal velocity, it can be assumed that the measured velocity is approximately equal to the streamwise velocity. The calibration of the velocity for the current experiment is given in Section 3.4.2. First it is explained in Section 3.4.1 how the hot-wire is integrated into the test section.

3.4.1 Experimental set-up

The current CTA bridge that is used is the IFA-300, which is connected to a LABVIEW program on a computer. For the HWA experiment the Dantec Dynamics type 55P15 hot-wire with curved prongs is used. The shape of the curved prongs allows measurements close to the test plate wall without any interference of the probe body. The hot-wire is connected to

a small hollow tube, which in part is connected to a stiff rod. The rod is connected to a support structure that can be moved in spanwise direction over an X-beam construction. With two traversing wheels the probe can be moved in streamwise direction and wall-normal direction as much as the slot allows. For the current investigation it is only wanted to inspect the behavior in wall-normal direction at one particular streamwise and spanwise position, namely the same location as where the PIV measurements are made. The hot-wire probe traversing system is inserted through a slot downstream of the test plate (Figure 3.33a). This allows a fixed mounting of the traversing system while still allowing for opening and closing of the test-section door while. The gaps next to the traversing system are then closed during the experiment to prevent ambient interference to the measurements.

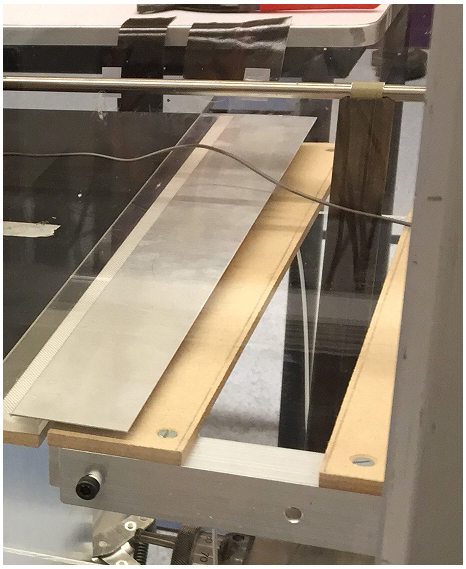

(A) Hot-wire probe insert.

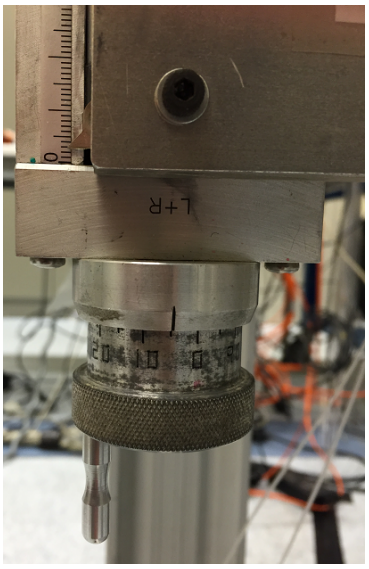

(B) Traversing wheel.

FIGURE 3.33: Hot-wire set-up specifics at the downstream slot.

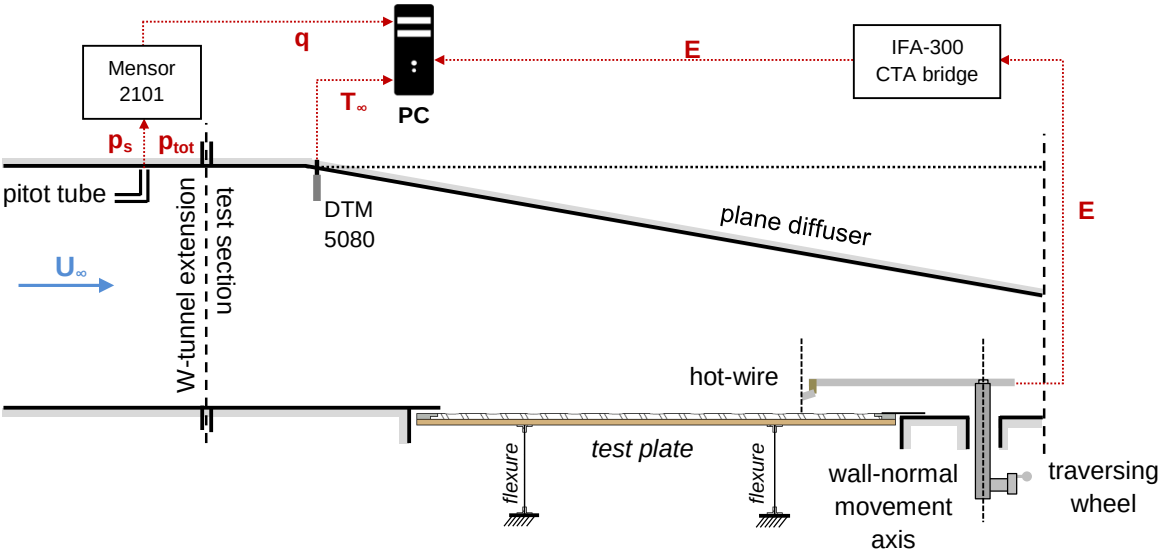

FIGURE 3.34: Hot-wire set-up within the test-section.

An attempt was made to measure the turbulent boundary layer in the upstream measurement location, but due to the length of the rod and the induced vibrations by the flow it

was not possible to measure the region in the upstream measurement location. Instead the location was fixed at the center of FOV 2 of the PIV measurements, such that the same measurement domain for the analysis was considered. This HWA path is shown together with the PIV domains in Figure 3.28.

The hot-wire measurements are sampled for 5 s with a sampling frequency of 50,000 Hz, in steps of 0.1 mm close to the wall, and steps of 2 mm further away of the wall. While the relative position between each measurement point could be determined by the traversing the wheel, determining its absolute position in respect to the wall can be a devious task. The HWA experiments were performed while the PIV cameras were active and calibrated. As result it was possible to detect the hot-wire probe in the captured area of the cameras (Figure 3.35). When the hot-wire is in close proximity to the wall, a reflection becomes visible on the surface of the test plate. Since the field of view of the camera is calibrated, it was possible to determine the smallest distance between the hot-wire and the wall by measuring the distance between the hot-wire and its reflection and dividing and two. To make sure the displacement imposed by the traversing wheel coincided with the displacement measured with the cameras, the hot-wire was captured at four locations. Its displacement was then correlated with the expected displacement by the traversing wheel to account for possible calibration errors.

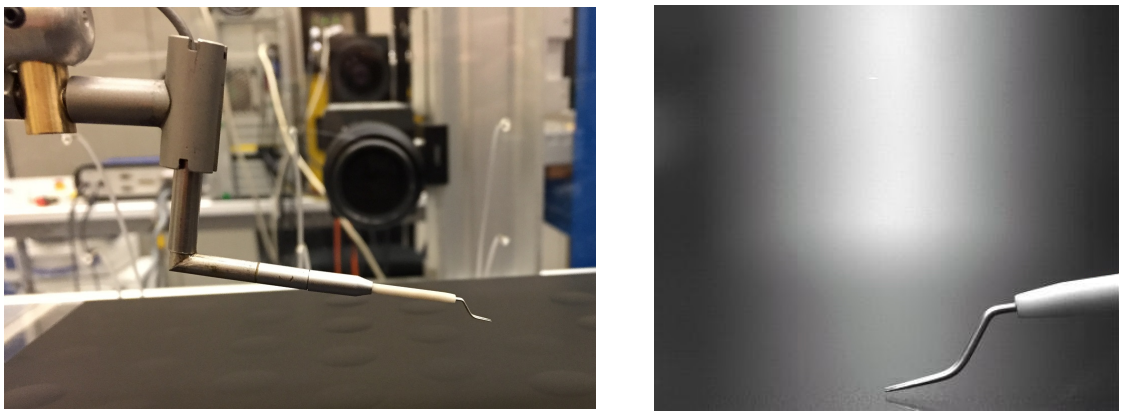

(A) Probe in camera view. (B) Probe and its reflection in DaVis.

FIGURE 3.35: Hot-wire observation with the PIV system.

3.4.2 Calibration

Before any actual measurement can be taken, the measured voltage must be associated with a corresponding flow velocity. Therefore first a calibration is performed. Before the wind-tunnel is started, the temperature of the hot-wire probe must be determined and calibrated. Using the overheat resistor of the bridge the overheat ratio can be set such that the wire has a desired temperature during the measurements. Using the values from the hot-wire probe specification, this overheat ratio is computed first and added to the program that sets the CTA bridge together with a predetermine gain value of 12 and an offset value of 1.16. Since the boundary layer has a decreasing mean streamwise velocity when moving towards the wall, the hot-wire is places at a sufficiently high location as far upstream as possible to have a good correspondence between the velocity measured with the pitot tube and the velocity measured by the hot-wire probe.

The Labview algorithm prescribed an initial calibration table that should be measured. A total measurement of 17 points spanning from $U_\infty = 0$ to $U_\infty = 30$ m/s was considered,

representing the velocity domain from the wall to the freestream respectively. A fourth order polynomial fit was then taken through the measured calibration values. The measured values and the calibration fit are given in Figure 3.36.

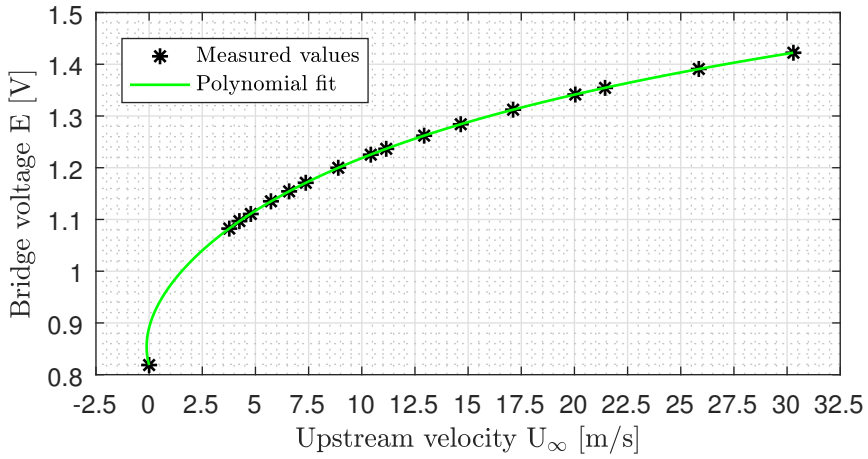

FIGURE 3.36: Calibration curve of the hot-wire.

3.4.3 Uncertainty

In this section some of the uncertainties will be addressed in respect to the HWA configuration. First of all there is the statistical error, that exists for N uncorrelated samples:

$$\epsilon_{\overline{u}} = \frac{u_{rms}}{\sqrt{N}} \tag{3.15}$$

$$\epsilon_{u_{rms}} = \frac{u_{rms}}{\sqrt{2N}} \tag{3.16}$$

which are the errors for the mean flow and the standard deviation respectively. As the number of samples N for each HWA measurement is 250,000. Taking the position close to the wall for the ZPG case at U_∞ = 15 m/s, where the velocity fluctuation are highest, an uncertainty margin of 0.02% is computed. This error becomes negligible when compared to research on drag-reducing riblets and oscillating walls, wherein changes in the order of a few percent in peak turbulence intensity are reported. Other than the statistical error, other possible errors can be identified:

- Calibration error. The pitot tube that is used to measure the upstream velocity U_∞ is placed in the wind-tunnel extension upstream of the measurement location. Due to boundary layer growth the velocity inside the test-section is accelerating slightly (as observed in Table 4.7). It is thus wanted to measure the velocity as close to the hot-wire as possible, while also staying outside of the boundary layer. To this end a pressure rod was attached near the hot-wire during the calibration (Figure 3.37). Instead of using the static port of the pitot tube, the pressure rod was used instead. There is still a wall-normal distance between the hot-wire and the pressure rod, but the streamwise difference is eliminated in this way.

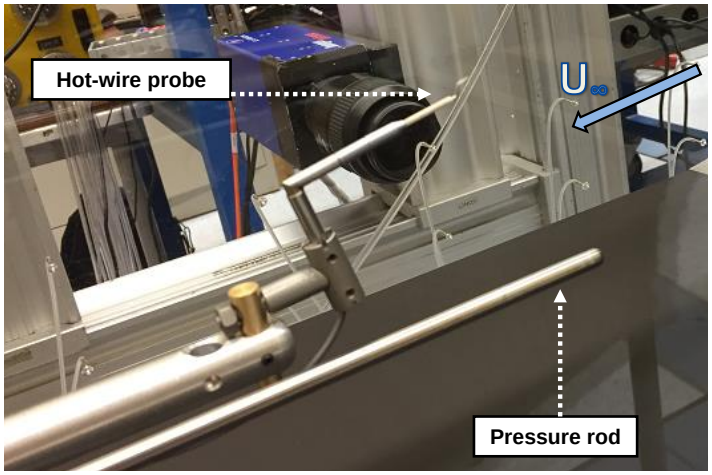

FIGURE 3.37: Location of the pressure rod relative to the hot-wire.

- Temperature differences. Throughout the day the ambient temperature inside the wind-tunnel changes, while the flow also heats up slightly due to the wind-tunnel fan. The calibration temperature T_{cal} is taken to be the mean of all the temperatures measured during the calibration. The LABVIEW program takes into account the temperature variations on the current by using Equation 3.17:

$$E_{corrected} = E_{amb}\sqrt{\frac{T_{wire} - T_{cal}}{T_{wire} - T_{\infty}}} \tag{3.17}$$

- Hot-wire misalignment. Ideally it is wanted to have the freestream velocity impinge the hot-wire perpendicularly. During placement there is a possibility that the hot-wire probe is misaligned with the flow direction. From Figure 3.35b it can be observed that the hot-wire supports align in both streamwise and wall-normal direction. The effect of possible misaligment is thus expected to be negligible.

- Wall interference. As the probe moves progressively towards the wall the effect of the wall becomes more profound. Heat flow next to the surface of the plate will also conduct into the wall surface. Jørgensen (2002) describes that this influence starts at $y^+ = 3.5$.

Even though errors can exist they exist only in the absolute sense: as turbulent boundary layer properties are compared for the HWA campaign, it is still possible to compare measured values relatively to one another.

Chapter 4

Results

In this chapter the results of the DFM, PIV and HWA campaigns (as well as the pressure measurements) are discussed. Instead of describing the results of each experimental technique into a separate section, a more integrated discussion is presented. First a *flow validation* is presented in Section 4.1, where the streamwise pressures and the flow topology observed by the tufts are discussed. The drag for the total test plate, encompassing the DFM campaign, is presented in Section 4.2 as the *total drag quantification*. Finally the boundary layer turbulent properties measured with the PIV and HWA experimental technique is discussed in Section 4.3 as the *flow quantification*.

4.1 Flow validation

The subject of this study is the effect of a pressure gradient on the drag-reducing properties of a dimpled surface. This pressure gradient was captured by means of streamwise pressure taps. In this section it is validated that adverse and favorable pressure gradients are created by the plane diffuser deflection. Due to the inherent properties of the drag balance (that requires side gaps) and the plane diffuser (that introduces a step angle deflection), the flow field is inherently affected by the application of a pressure grap. This flow field is qualitatively investigated by the mean of tufts at several crucial locations.

4.1.1 Tuft behavior

Before arriving at a quantification of the pressure gradients, the flow topology observed from the tufts is discussed first. To examine the flow topology during the experiments tufts were applied at three general locations:

- Plane diffuser, to check for separations for adverse pressure gradients,
- Close to the test plate surface at the wall, to check for wall vorticity and flow behavior near the gaps,
- Flexure shielding, to check for the flow behavior underneath the test section due to the release of side flow through the gaps.

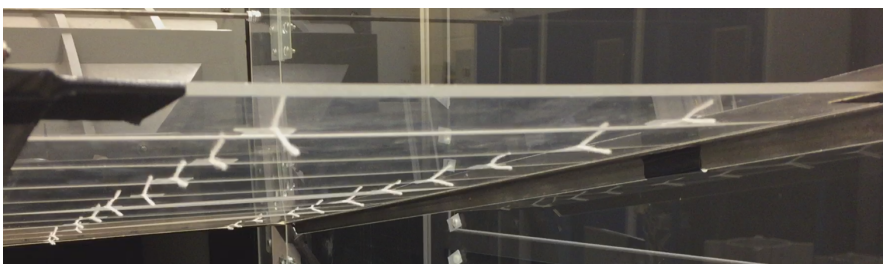

FIGURE 4.1: Tufts at the upper wall at U_∞ = 10 m/s in the SAPG configurations.

Plane diffuser. A step angle φ is applied near the intersection of the wind tunnel nozzle with the test set-up. To see if the flow separates for the SAPG case, which has a high deflection angle of $\varphi = 10°$, tufts were applied on each sliding plate that makes up the diffuser. The most critical case of U_∞ was considered, and it was found from the tuft behavior in Figure 4.1 that the flow was not separating at the top diffuser. As the flow was not separating for this case, the sliding plates were not shifted throughout the experiment, and no screen behind the test-section was required to create natural boundary layer separation.

Test plate surface. The physical gap with the test sections starts as soon as the flow enters from the tunnel wall to the test plate. At this location the flow is then suddenly exposed to the ambient below the test plate. The flow was inspected in further detail at this location for several pressure gradient cases. In Figure 4.2 the tufts at the start of the test plate are shown.

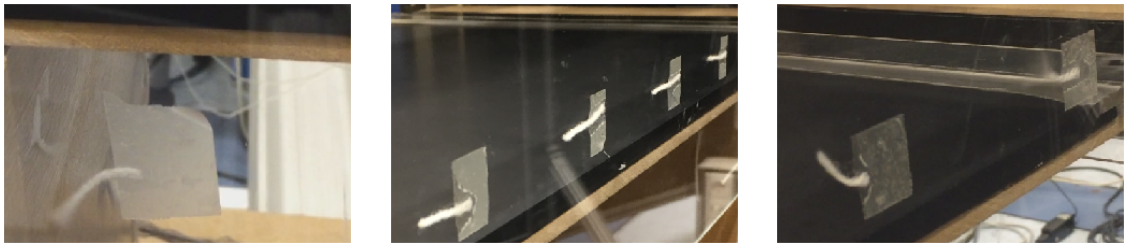

(A) SFPG. (B) ZPG. (C) SAPG.

FIGURE 4.2: Wall tuft behavior near the test plate for the highest considered upstream velocities.

It is found that when a favorable gradient was applied (by a negative downward deflection of the top planar diffuser), the flow leaves the test section in a steep manner (Figure 4.2a), For the ZPG, no considerable oscillations of the tufts were observed. When an adverse pressure gradient was applied the tufts were pointed in an upward position, indicating that flow from the ambient is entering the test section at the start of the test plate. The effects of the gaps become more profound as the Reynolds number increases.

(A) (B) (C)

FIGURE 4.3: Tufts vibrating below the test plate at the flexure shielding for the SFPG figuration.

Flexure shielding. It is observed from Figure 4.2a that flow is escaping the test section through the gaps at the sides of the test plate. This flow then enters the space underneath the test plate where the force is measured. The drag balance consists of two delicate plates, where small external flow impingement can cause extra forces measured by the load cell that are hard to quantify and are not part of the drag force experienced by the plate. To counteract this the flexures are shielded with cardboard and fitted with tufts to see if this is actually transpiring. In Figure 4.3 the flow field under the test plate is inspected in further

detail for the SFPG configuration. The tufts show violent behavior, and show clear flow impingement against the flexures.

4.1.2 Streamwise pressure

The pressures are measured at the wall location at the utmost spanwise position of the test plate. At this location there is also the gap that is required to perform the drag balance measurements. As a result the measurements at the side wall are influenced by the effect of flow entering or leaving the test sections through the gaps at these locations. The pressure is measured locally in the pressure transducer system and compared to the ambient temperature. As a result the values for Δp shown in Figure 4.4 for different diffuser angles are measured in respect to the ambient instead of the upstream position.

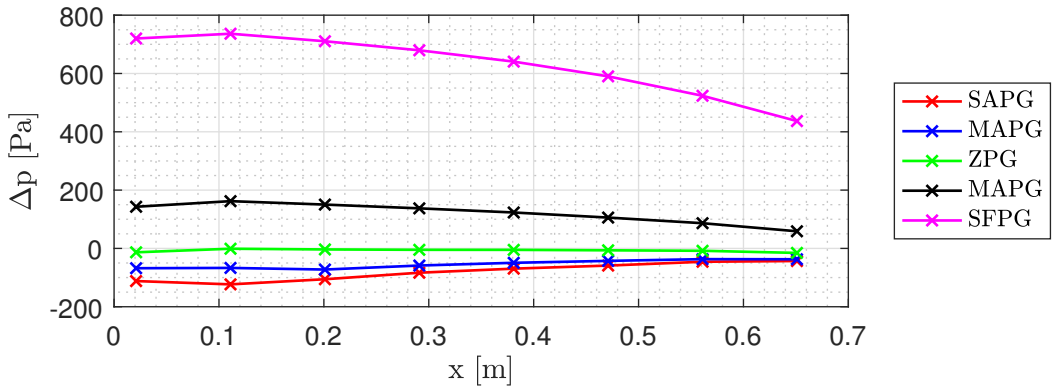

FIGURE 4.4: Pressure differences Δp in respect to the ambient pressure for the different configurations for U_∞ = 22 m/s.

From Figure 4.4 it is found that the effect of inducing a favorable pressure gradient has a more significant effect on the pressure gradient than the variation for an adverse pressure gradient. The SFPG case has the largest inward deflection φ = -13° (SFPG) and causes the highest pressure gradient. For this case the streamwise pressure decreases when traversing in the downstream direction, indicating an accelerating flow and confirming a favorable pressure gradient. The same can be declared for the intermediate favorable pressure gradient case MFPG. The pressure is observed to increase in the streamwise direction for the MAPG and SAPG cases confirming an adverse pressure gradient and indicating deceleration of the flow. The effect of outward deflection is less powerful than for inward deflection. The absolute differences between the SAPG and the MAPG case are smaller than the difference measured between the MFPG and the SFPG case. For the adverse pressure gradient cases it is observed that the pressure differences become increasingly close when closing in at the end of the test section. The profiles do not end up at the ambient level (Δp = 0) as the flow is still accelerating of decelerating when it reaches the test section end.

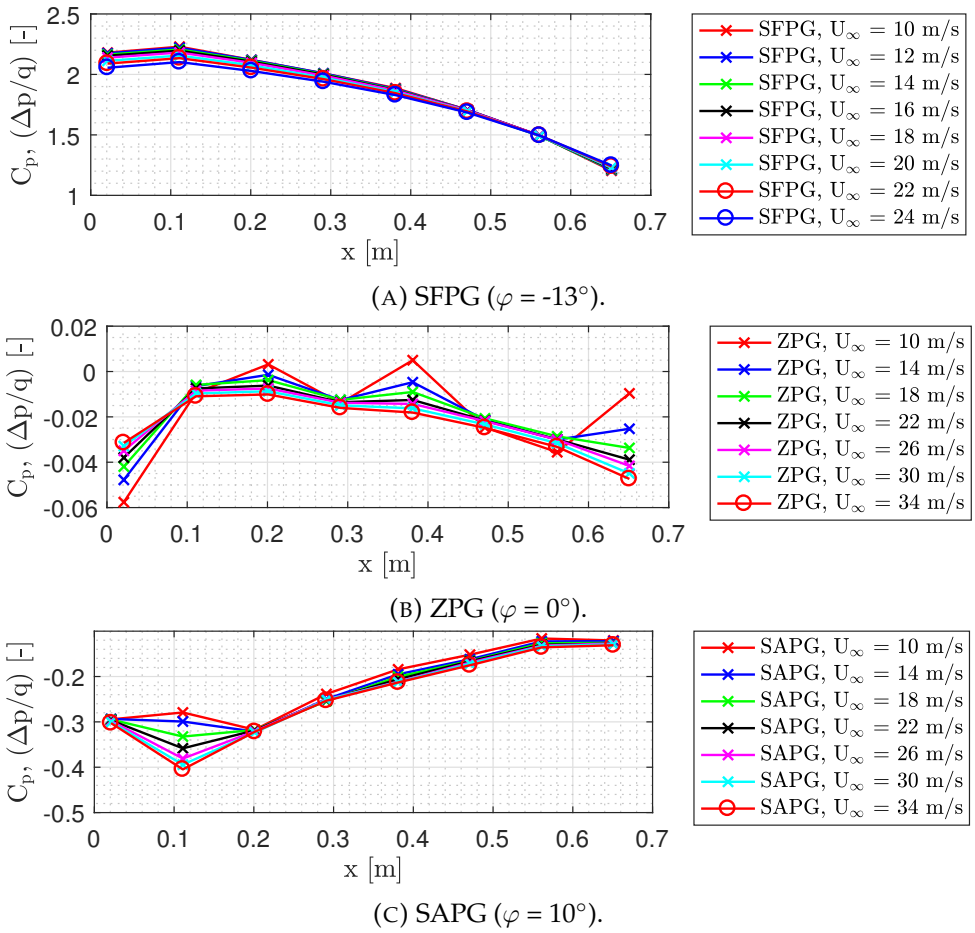

(A) SFPG (φ = -13°).

(B) ZPG (φ = 0°).

(C) SAPG (φ = 10°).

FIGURE 4.5: Streamwise pressure coefficients.

It is proper custom in aerodynamics to non-dimensionalize quantities and the pressure is no exception to this. When the pressure difference with the ambient Δp is divided by the dynamic pressure q the result is the pressure coefficient C_p in Figure 4.5. In Figure 4.5 the pressure coefficients are given for different upstream velocities for the most extreme pressure gradient cases and the zero pressure gradient case. For the all pressure gradient cases it is observed that the pressure coefficient curves coincide into a single C_p curve. For the SAPG case in Figure 4.5c it is found that the second pressure tap in the streamwise direction at x = 0.1 m shows a response to the change in upstream velocity that is not observed for the zero and favorable pressure gradient cases. This location coincides with the location where the flow was observed to enter the test section in Figure 4.2c whereas the first tap is placed just in front of the interface between the test plate and the wind tunnel extension. The pressure coefficients then most likely disagree due to the influx of flow from the ambient at this wall location.

4.2 Total drag quantification

Whereas the PIV and HWA campaigns quantify the flow at specified streamwise positions, the DFM campaign establishes a drag force for the *entire* test plate and thus poses a complete picture of the total drag force. In this section the results of the direct force measurements will be discussed leading up to the drag reductions observed for the different pressure gradient cases.

4.2.1 Raw force data

When the experimental procedure of Section 3.2.5 is followed a force signal and a velocity signal is created for each run. In Figure 4.6a and 4.6b such a typical force signal and velocity signal is shown for the FZ1 case.

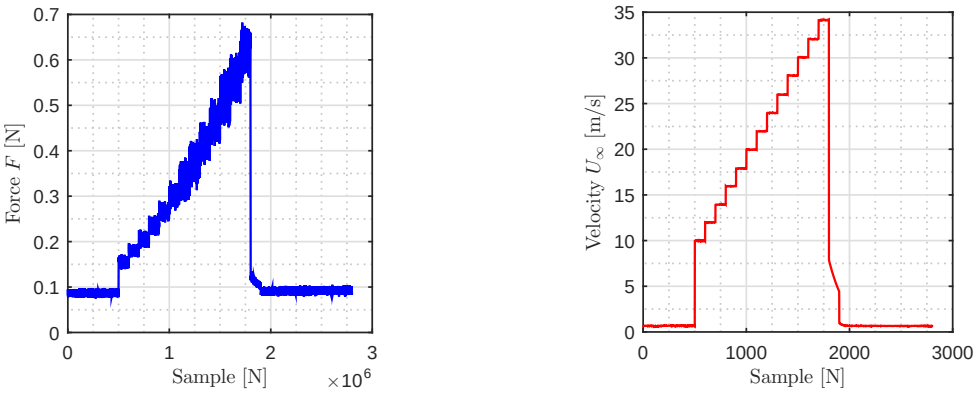

(A) Calibrated force F. (B) Upstream velocity U_∞.

FIGURE 4.6: Unprocessed signals.

The upstream velocity starts at 10 m/s and progresses up to 34 m/s, the maximum setting of the RPM, and is then shut off. The windtunnel does not shut off immediately, and thus there is still a 'recovering' period present in the force signal after the highest upstream velocity. For the raw force signal it is observed that the data spread increases for increasing velocities, and is thus prone to increasing vibrations in the system.

In accordance with aerodynamic tradition the aerodynamic properties are non-dimensionalized for proper comparison. For each step the force signal is averaged into F_{raw}, corrected for the initial pre-run force and the pressure difference (see Section 3.2.4) into an effective drag force F_D, then non-dimensionalized by the test plate area S and the dynamic pressure q (that is also captured in the raw velocity file outputs) to yield a drag coefficient C_D.

$$C_D = \frac{F_D}{qS} \tag{4.1}$$

The upstream velocity is non-dimensionalized into the Reynolds number Re_D that is based on the dimple diameter D and the kinematic viscosity ν determined from the flow temperature:

$$Re_D = \frac{DU_\infty}{\nu} \tag{4.2}$$

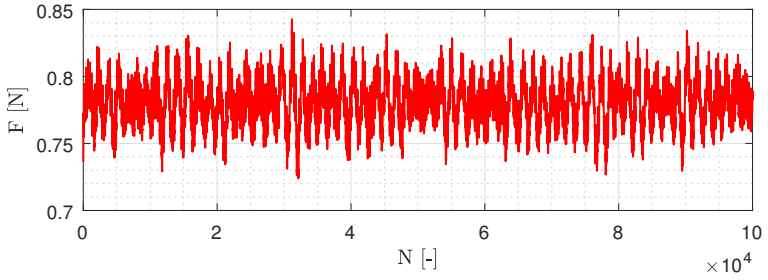

FIGURE 4.7: Typical force signal at one specific upstream velocity over a 10 s period. Conversion by calibration already applied.

The force is samples at 10,000 Hz for 10 s, resulting in a total of 100,000 measurement points for each measurement. A look at the force signal in Figure 4.7 shows the existence of a force signal bandwidth imposed by vibrations in the force signal. This increasing force signal spread with increasing upstream velocity has implications for the statistical significance of the force signal, which is discussed in further detail in Section 4.2.2. A look at the energy spectrum of the force signal is given in Section 4.2.3.

4.2.2 Statistical significance

Even though the force signal is oscillatory, it is observed that with enough sample points individual measurements fall into a normal distribution. In Figure 4.8 the measurements at higher velocities have higher variances, with large overlapping areas. For smaller velocities the variance is relatively small compared to one another.

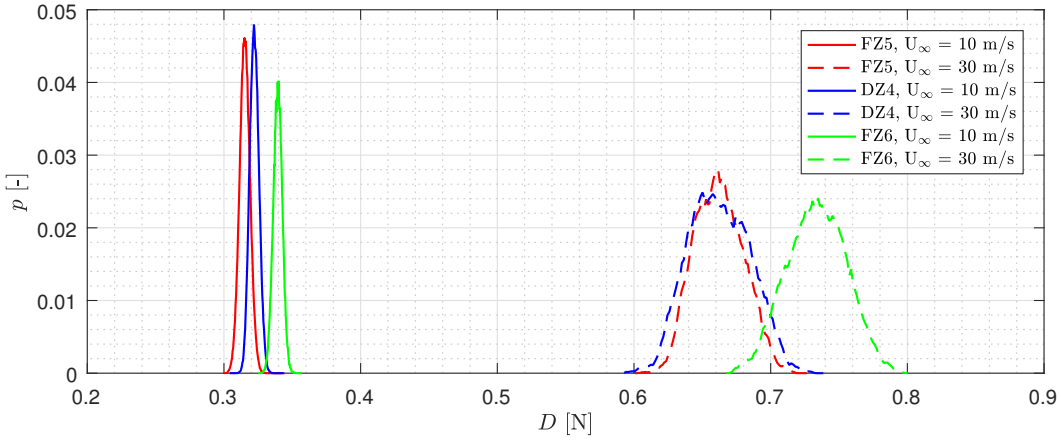

FIGURE 4.8: Uncorrected force probability distributions for different velocities and cases.

When a large part of the probability distribution starts to overlap, small differences in the mean value become less significant. A way to quantify the statistical significance is by the classic t-test by Welch (1938), exemplified in Equation 4.3 for two mean values $\overline{X}_1$ and $\overline{X}_2$. A confidence interval of 0.01% is chosen to compare the statistical significance.

$$t = \frac{\overline{X}_1 - \overline{X}_2}{\sqrt{\frac{\sigma_1^2}{N_1} + \frac{\sigma_2^2}{N_2}}} \tag{4.3}$$

There are two ways in which the t-value can become sub-critical for the measurements (for a same amount of measurement points). When the means of both measurements are very close to one another, or/and when the variances of the data sets are relatively large. The behavior observed in Figure 4.9, where the t-values generally decrease towards the higher Reynolds number regimes can then be explained by the increase of the variance of the force signal with increasing Reynolds number. The values are however well above the critical t-value. In Figure E.1a the t-values computed for the ZPG cases are shown. The t-values are computed by comparing the dimpled value with both the preceding and subsequent measurement (thus two t-distributions per dimpled case). Only one of the t-values is below the critical t-value for a 99.99% confidence interval, corresponding to one measurement point. The t-values for each pressure gradient case are given in Appendix E.

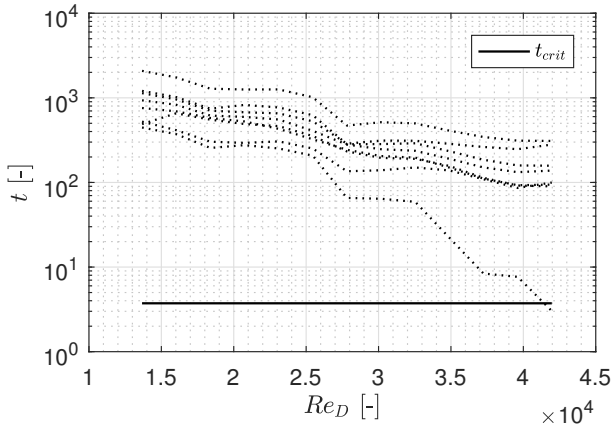

FIGURE 4.9: T-values for the ZPG case.

4.2.3 Vibration analysis

From the force signal presented in Figure 4.7 it becomes clear that there exist periodical variation in the signal. The result of the vibrations causes the force signal to have a higher variation for increasing Reynolds numbers. By applying a direct Fourier transform to the force signal at a high velocity of U_∞ = 30 m/s the power spectral density is computed. The flexures themselves are designed to have a low stiffness compared to the force sensor. The disadvantage of this flexibility is that they become prone to vibrations. The flexure balance presented in Section 3.2.3 has an effective stiffness and a defined mass. This allows for computing the expected natural frequency of the total flexure system. With an equivalent stiffness of 8,589 N/m and a plate mass of 5.5 kg the natural frequency can be computed with Equation 4.4.

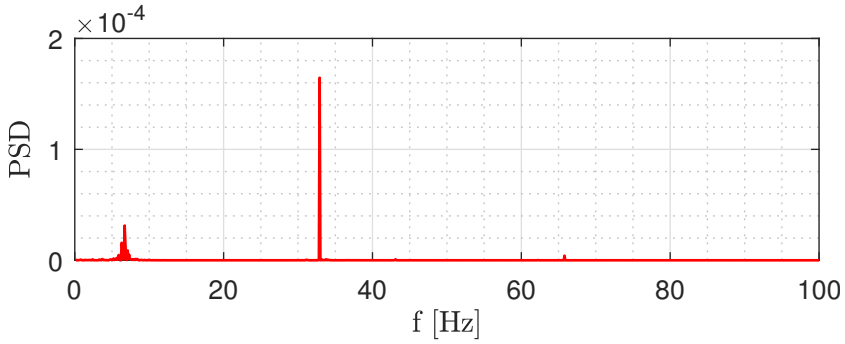

(A) Test plate attached to the load cell (FZ5).

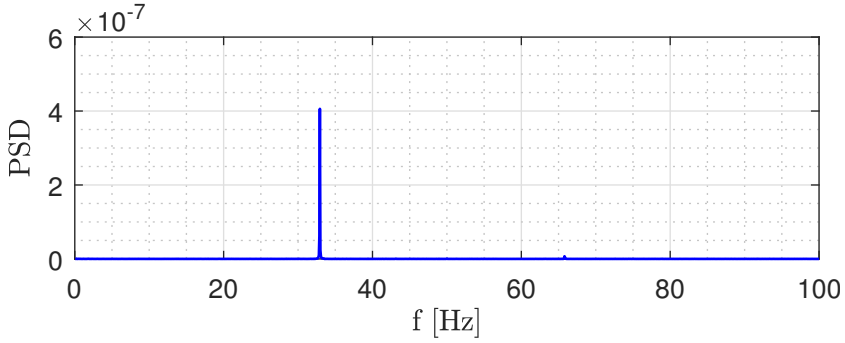

(B) Test plate detached from load cell (VZ).

FIGURE 4.10: Power spectral density for the ZPG case for U_∞ = 30 m/s.

$$f_{nat} = \frac{1}{2\pi}\sqrt{\frac{k_{eq}}{m_{plate}}} \tag{4.4}$$

A natural frequency of 6.6 Hz is computed. The vibration analysis is presented for U_∞ = 30 m/s for the ZPG case in Figure 4.10. This corresponds with the peak observed in Figure 4.10a. Another peaks is observed at 33 Hz. To investigate if these peaks are a result of aerodynamic phenomena, a dry run has been performed where the test plate is anchored and making no contact with the force sensor underneath the test plate. Looking at the same frequency plot in Figure 4.10b it is observed that the peak is maintained, although at a smaller spectral density compared to the attached test plate. The wind tunnel fan is operating at 866 RPM at this velocity, equivalent to 14 Hz, and thus this frequency is not caused by the wind tunnel fan. Other phenomena are thus responsible for this peak frequency other than the drag balance and the tunnel fan, but as of yet unknown. However, due to the relatively large frequency the vibration is averaged out over the 10 s measurement period.

4.2.4 Temperature averaging

As previously mentioned in Section 3.2.5 the sandwich principle is applied in which the performance of a dimpled plate is compared to the average of the preceding and subsequent flat plate. In Figure 4.11 the temperature during each measurement run is shown for the ZPG case. Two main features are observed. Firstly, the temperature increases slightly as the velocity in the test-section increases, possibly due to warming of the wind-tunnel fan. Secondly, the temperature varies throughout the day. The temperature in the wind-tunnel increases throughout the day, but decreases in the evening. Note that some measurement points are missed (for CFZ3 and CFZ8) due to failure of the LABVIEW algorithm to toggle the measurement routine at these points.

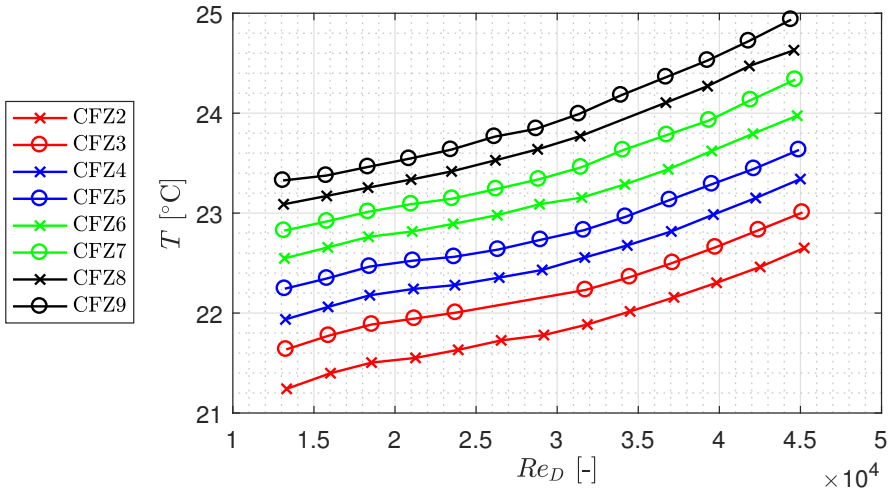

FIGURE 4.11: Temperature during each run for the second repeatability experiment.

Now the sandwiching is applied to the temperature profiles presented in Figure 4.11. CFZ2 is sandwiched by CFZ1 and CFZ3, CFZ3 by CFZ2 and CFZ4 etcetera. The result is shown in Figure 4.12. In this case it is shown that the temperature increases quasi-linearly throughout the day. As the same time interval between each measurement is taken, the average temperature of the preceding and subsequent runs approaches the sandwiched case quite adequately.

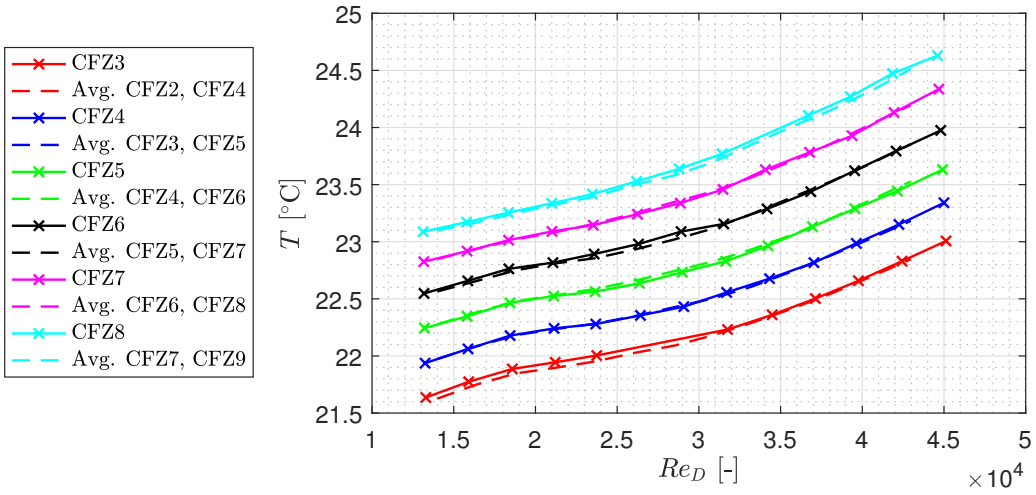

FIGURE 4.12: Sandwiching principle applied to temperature for the second repeatability experiment.

4.2.5 Repeatability

The drag balance and the experimental set-up are new additions to the experimental repertoire, and thus they are scrutinized first to check if possible drag reduction can actually be attributed to a dimpled surface. To this end repeatability experiments are performed with the balance in the ZPG configuration during the first two days of the experimental campaign. Two effects will be examined in the repeatability measurements: the effectiveness of the sandwiching described in Section 3.2.5 and the effect of opening the door and replacing the plate. The same measurement routine and timing intervals are used, to ensure good comparison with the actual measurement days where the dimpled surfaces are compared to the flat surfaces. In the sandwiching principle the drag coefficient of a dimpled plate is compared with the previous and following flat plate drag coefficients. The general drag reduction formula is presented in Equation 4.5:

$$\Delta C_D = \frac{C_{D,dimpled} - C_{D,flat}}{C_{D,flat}} \times 100\% \tag{4.5}$$

where $C_{D,flat}$ is the average of the preceding and following plate, linearly interpolated to the dimpled Re_D value. When the dimpled plate is replaced with a flat plate the effective drag reduction should be zero. Any other value would indicate faults with the test set-up or the calculation routine. To this end repeatability experiments are performed in which the flat plate is left in the set-up and is thus not replaced in between runs (indicated by prefix R-). The section door stays closed. Theoretically this means that no physical changes are made to the experimental set-up throughout the day and purely the effect of sandwiching can be investigated.

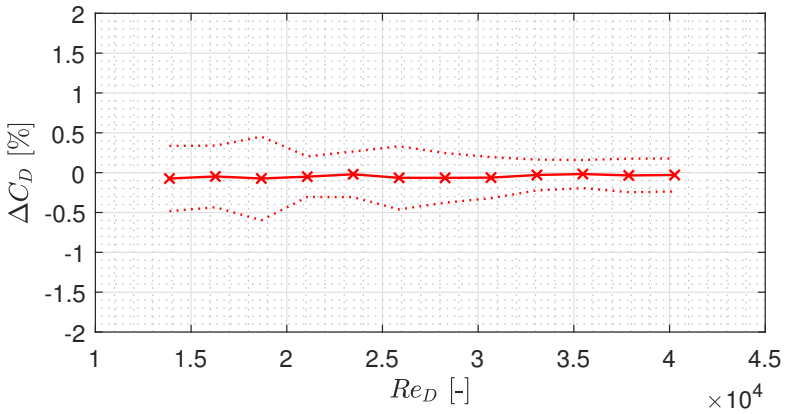

FIGURE 4.13: Computed drag difference for the repeatability experiments where the test-section is left stationary, with dotted RMSE bounds.

In total 9 repeatability measurements are performed, meaning that the sandwiching can be applied 7 times (as the first plate can not be compared to a preceding plate and the last plate can not be compared to a following plate). The effective drag reductions computed with the sandwich principle are shown in Figure 4.13 over the entire Reynolds number domain. The mean of the drag difference is shown to be slightly below the 0% line. A slight decrease of the error is observed with increasing Reynolds number. It is tedious to find a real physical explanation for this. Only a relatively small number comparisons are performed. It could be possible that increasing the sample size annuls the RMSE error differences with Reynolds number change.

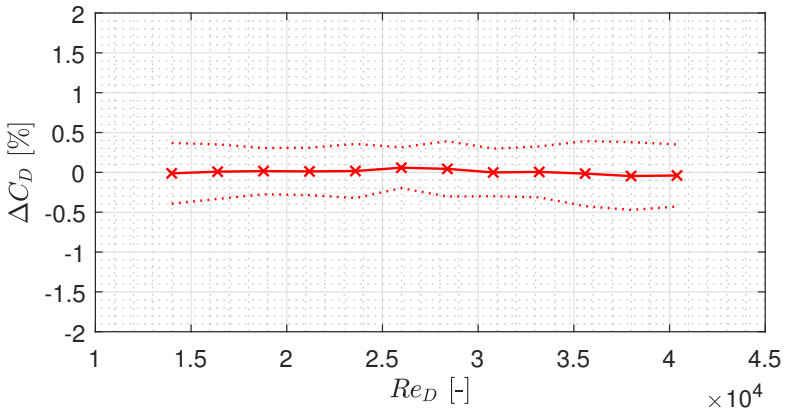

FIGURE 4.14: Computed drag difference for the repeatability experiments where the flat plate is interchanged between measurements, with dotted RMSE bounds.

The invariability of the set-up is only breached when the section door is opened and the test plate is replaced. Small force differences are measured, and thus small changes to the set-up can possibly cause unwanted differences between measurement runs. To achieve consistency as much as possible is done to ensure the invariability of the set-up, including the shielding and clamping of the experimental set-up such that internal movement is prevented. Internal movement could cause small misalignment of the balance with the force sensor, causing changes in the results between runs that are not due to the dimples. The only changes that are allowed to the test set-up from design are the replacement of the test-plates and the opening of the test-section door. To examine if the opening of the door and replacement of the plate has any measurable effect on the drag coefficient a second repeatability

experiment is performed (with prefix C-). Once again only a flat plate is used, but instead of leaving it inside the test section it is taken out and subsequently placed back again between measurement runs. The effect of the plate replacement and door opening on the drag difference can then be quantified. The results are given in Figure 4.14.

Once again the mean of the drag difference varies slightly around 0% throughout the entire Reynolds regime. A maximum RMSE of 0.4% is observed from Figure 4.14, but compared to the first repeatability experiment there is no decrease in RMSE error as the Reynolds number increases. A small increase with Reynolds number is however observed, but the RMSE still falls within the 0.4% range. The experiment runs show that the expected mean value of 0% drag difference is produced with a RMSE well within the order of several percent for which drag reductions are found (for the ZPG configuration).

4.2.6 Effect of pressure gradient

Now that the repeatability of the experiment has been discussed, the sandwiching principle is also applied for the other pressure gradient cases. In this section the drag differences as a function of Reynolds number are presented.

Zero pressure gradient (ZPG). The first case that is considered is the ZPG case ($\varphi = 0°$). The ZPG case has been studied extensively for other drag-reduction mechanisms and also for the dimpled case by Vervoort (2007), Van Nesselrooij (2015) and Van Campenhout (2016). For the ZPG case a total of 4 dimpled cases were measured. After applying the corrections and non-dimensionalizing, the results in Figure 4.15 were acquired.

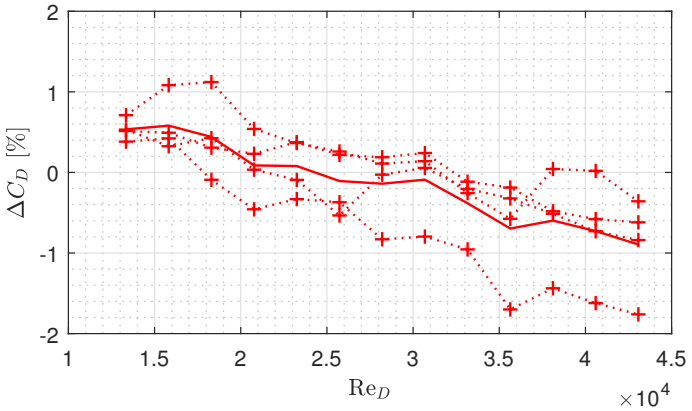

FIGURE 4.15: Drag difference for the individual measurements and mean drag difference against Reynolds number for the ZPG case.

The drag difference starts at a positive value for low Reynolds numbers, indicating a drag increase. When the Reynolds number is increased, the drag differences starts to become negative, indicating a drag reduction. Thus an increasing drag reduction is observed for increasing Reynolds numbers. A maximum drag reduction of 0.8% is observed. All individual comparisons show a drag reduction at the highest Reynolds number measurement.

Just as the repeatability measurements shown in Section 4.2.5 the same diffuser angle $\varphi = 0°$ was used. Measured over two different days in this configuration the average drag delta was observed to be twice zero-valued when only flat plates were considered, with error margins lying within a half percent. The current ZPG case in which the dimple is used yields an effective drag reduction using the same set-up, and thus this result seems to indicate that

a drag reduction is present, although relatively small. When looking at Figure 4.3 it is also observed that the t-values computed for the ZPG case are with exception of a single measurement point all within a 0.01% confidence interval significance.

Strong favorable pressure gradient (SFPG). The second discussed case is the SFPG configuration (φ = -13° case). For this configuration a total of three sandwiched dimpled plates were considered. In Figure 4.16 the results of the three comparisons are given.

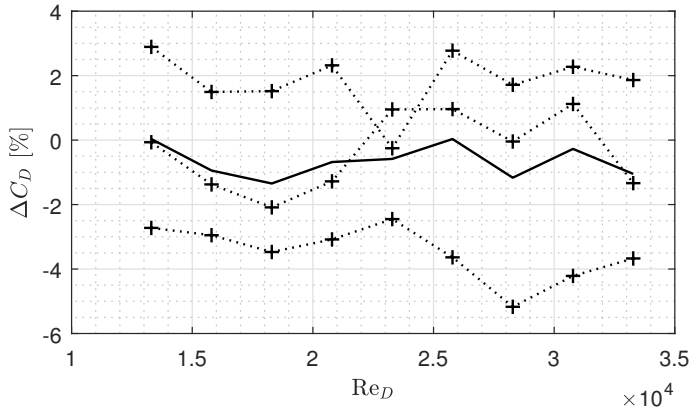

FIGURE 4.16: Drag difference for the individual measurements and mean drag difference against Reynolds number for the SFPG case.

From Figure 4.16 it is found that the individual measurements show a relatively constant behavior with $\mathrm{Re_D}$. When looking at the individual measurements, it is found that during the experiment one measurement run yielded a drag reduction, while the other two a drag reduction. When averaging the drag differences for all three considered measurement runs a drag difference ΔC_D between 0% and -2% is found. The Reynolds number does not seem to have a large influence on the drag difference, as the mean difference is relatively constant with $\mathrm{Re_D}$, and no downward trend is observed as for the ZPG case. The results are acquired using the same experimental procedure as for the ZPG case and a drag reduction is observed, but compared to the ZPG case, no repeatability experiment is performed to see the effect of diffuser deflection on the drag difference results using just a flat plate.

Mild favorable pressure gradient (MFPG). Between the ZPG case and the SFPG the intermediate diffuser angle φ = -6° is considered, imposing a smaller favorable pressure gradient compared the SFPG case. Three sandwiched dimpled plate cases are considered, shown in Figure 4.17.

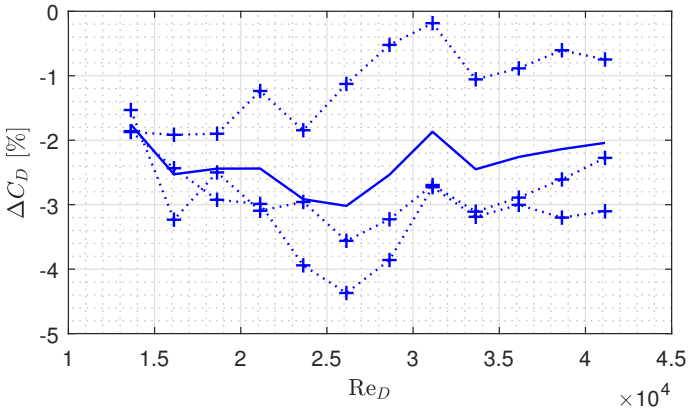

FIGURE 4.17: Drag difference for the individual measurements and mean drag difference against Reynolds number for the MFPG case.

In contrast to the previous SFPG case all three individual measurements show a negative drag difference. One measurement which yields the smallest drag reduction shows an upward trend for the drag difference with $\mathrm{Re_D}$. while the other two considered comparison show a downward trend with increasing Reynolds number. The total drag difference then oscillates between -2% and -3%, indicating that for the MFPG case a drag reduction is also observed. The mean trend with $\mathrm{Re_D}$ is then observed to be relatively constant. Comparison between the MFPG and SFPG case then implies that the drag difference is more profound for a relatively mild favorable pressure gradient, although increasingly stochastic.

Mild adverse pressure gradient (MAPG). Now that the favorable and zero-valued pressure gradients are considered, an adverse pressure gradient is investigated, in this case the MAPG case with a deflection φ = 5°, intermediate between the SAPG and the ZPG cases. Once again three sandwiched dimpled plates are considered. In Figure 4.18 the results of the MAPG measurements are presented.

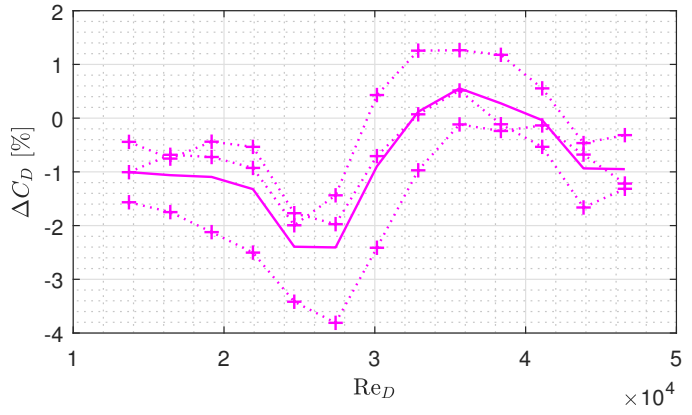

FIGURE 4.18: Drag difference for the individual measurements and mean drag difference against Reynolds number for the MAPG case.

Compared to the previous cases the behavior of the drag reduction is consistent for each drag comparison but in a somewhat tedious pattern. It decreases to a mean drag reduction of 2.5%, then increases up to a drag increase of 0.5% and subsequently moves downward again to a drag reduction of -1% for the highest considered Reynolds number. Analogous to the drag result of the SAPG case, the MAPG case has a distinct dent in its force signal,

possibly indicating the dent on in the force signal. Looking at the particular drag difference behavior at the dent, it is observed that the rise in ΔC_D between $Re_D = 2.6\times10^4$ and $Re_D = 3.8\times10^4$ corresponds to the dent in the drag coefficient curve as presented in Figure 4.20.

Strong adverse pressure gradient (SAPG). The final case that is considered in the DFM campaign is the SAPG configuration. For the SAPG configuration a step angle deflection $\varphi = 10^\circ$ is considered. For this configuration it was validated that no flow separation occurred on the top plane diffuser, although it was observed that flow entered the set-up through the side gap. Bearing this in mind, the drag difference results are presented in Figure 4.19. For this configuration a total of three sandwiched dimpled plates were considered.

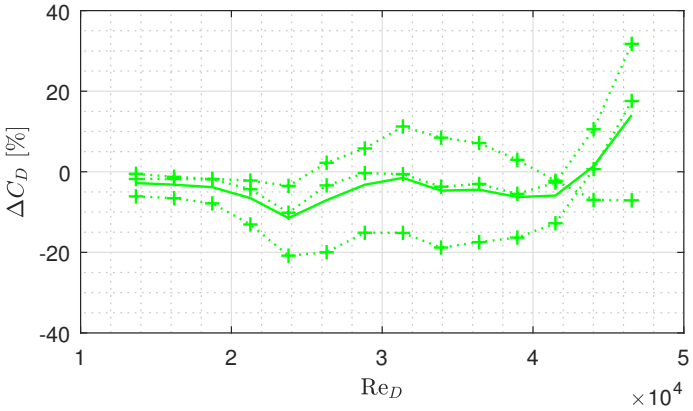

FIGURE 4.19: Drag difference for the individual measurements and mean drag difference against Reynolds number for the SAPG case.

From Figure 4.19 it is found that the drag difference starts at a drag reduction, and goes to drag difference of -10%. It then starts to increase again up to a drag difference of approximately 0% and then continues upwards to approximately 10%, indicating a drag increase. The results indicate a relatively large drag reduction that goes into a relatively large drag increase at the highest considered Reynolds number.

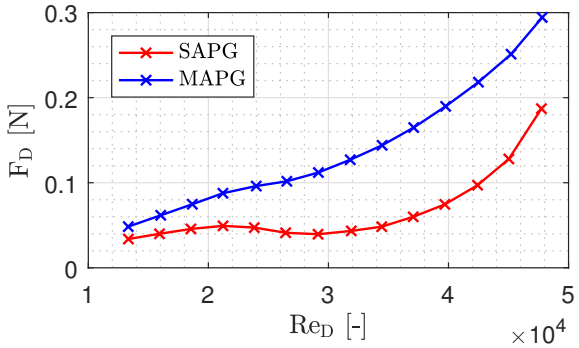

FIGURE 4.20: Dent in the force signals for the MAPG and SAPG cases.

When looking at an individual force signal in Figure 4.20 it is observed that for the adverse pressure gradient cases a dent exists the drag difference. A decreased force could indicate the advent of separation on the plate. It was however investigated using a tuft to see if separation appears on the plate. However, no separation was observed by means of the tuft, as it would indicate chaotic movement of the tuft in all directions. As a result the cause is still unknown.

4.3 Flow quantification

In the previous section the drag reducing effect of the entire surface was given. In this section the results from the PIV and HWA campaigns are used to quantify the flow in the boundary layer to resolve if a drag reduction is observed in the boundary layer profile and how it is achieved.

4.3.1 Flow field convergence

Instantaneous flow fields. During the DFM campaign it was checked that the flow was turbulent by using a microphone, which measures a larger amount of noise for a turbulent boundary layer than for a laminar boundary layer. An additional check is performed using the instantaneous velocity fields of the PIV campaign. A turbulent flow is characterized by chaotic structures and alternating regions of high and low velocity. For relatively higher Reynolds numbers the flow becomes increasingly prone to transition to a turbulent flow, so the low Reynolds numbers are most critical when looking for the presence of a turbulent boundary layer.

The mean velocity for the streamwise and wall-normal component are determined by Equation 4.6, where N is the total number of samples after outlier removal.

$$\overline{u}(x,y) = \frac{1}{N}\sum_{i=1}^{N} u_i(x,y), \qquad \overline{v}(x,y) = \frac{1}{N}\sum_{i=1}^{N} v_i(x,y) \tag{4.6}$$

The instantaneous streamwise and wall-normal fluctuation in a point are then determined by Equation 4.7.

$$u_i'(x,y) = u_i(x,y) - \overline{u}(x,y), \qquad v_i'(x,y) = v_i(x,y) - \overline{v}(x,y) \tag{4.7}$$

Applying these relations to all the raw velocity profiles obtained from PIV, the instantaneous velocity fluctuation fields are computed. In Figure 4.21 the instantaneous velocity fluctuation fields are shown for the upstream location (FOV 1) for both the SFPG and SAPG case.

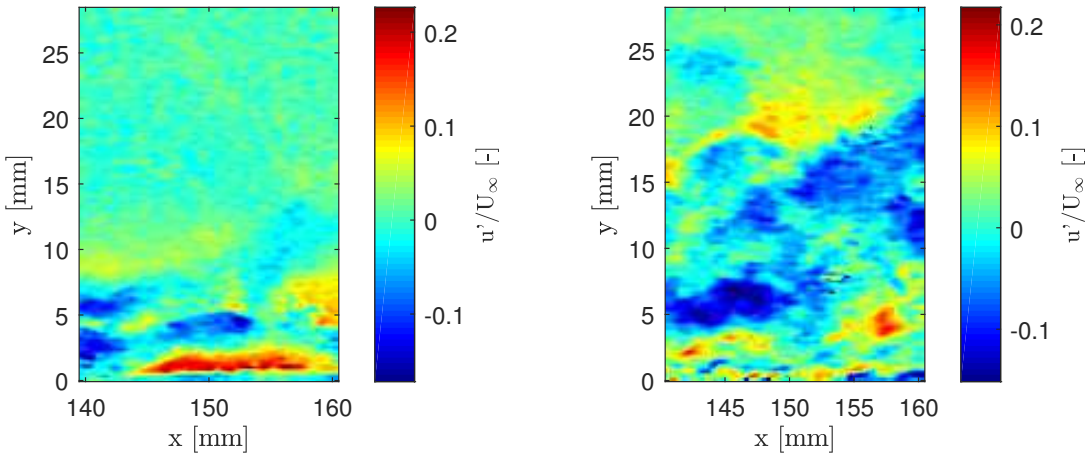

(A) SFPG, U_∞ = 7 m/s. (B) SAPG, U_∞ = 15 m/s.

FIGURE 4.21: Instantaneous streamwise velocity fluctuation fields in the upstream location at x = 150 mm.

In Figure 4.21 both the streamwise fluctuations are shown for the SFPG case and the SAPG case. In both Figure 4.21a and 4.21b is observed that there exist fluctuations of both negative and positive magnitude, confirming the existence of a turbulent boundary layer. It is seen in Figure 4.21a that most fluctuations are confined to the lower part of the turbulent boundary layer, while for the SAPG case the fluctuations are also present in the top part of the turbulent boundary layer. The boundary layer instantaneous fluctuation fields thus confirm the turbulent boundary layer heard by the microphone.

Flow convergence. The outlier removal procedure shown in Section 3.3.2 leads to the number of samples to be slightly less than 1,000 (which is the original sample size). This leads to every point on the FOV to have a different number of samples, which is is incorporated into the MATLAB processing algorithm. The mean flow fields computed by Equation 4.6 are thus computed at a different N at each location (x,y). After outlier removal the mean streamwise velocity fields are obtained. They are given in Figure 4.22 for both the SFPG and the APG case.

The SFPG is caused by an accelerating flow. The boundary layer is becoming thinner with increasing streamwise distance while the SAPG boundary layer is becoming thicker. Due to the growth of the boundary layer for the SAPG case, the freestream velocity can not be captured due to the top of the boundary layer being outside the field of view. It is furthermore found that both flow fields are smooth, and no outliers are observed in the converged flow fields.

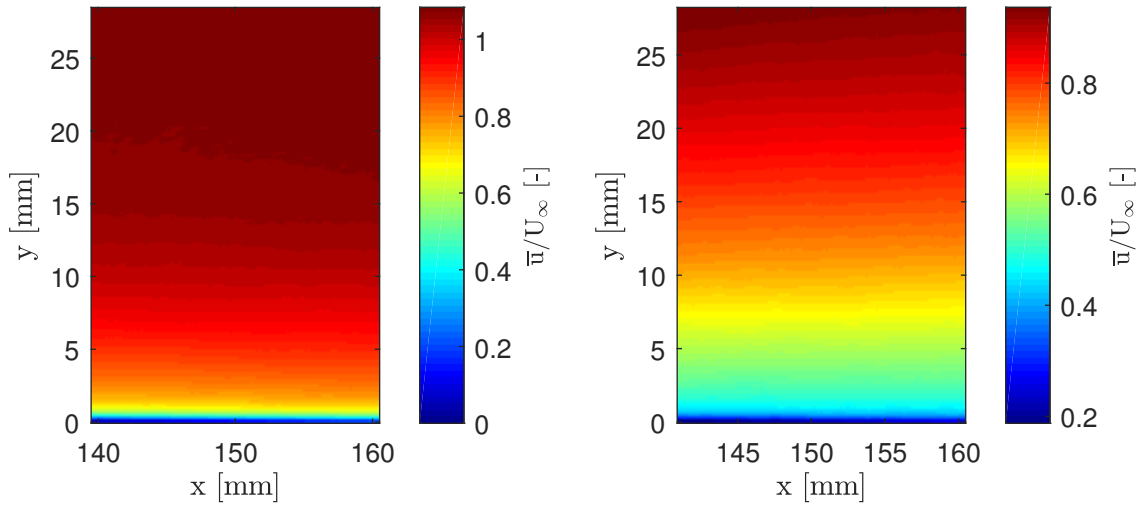

(A) SFPG, U_∞ = 7 m/s. (B) SAPG, U_∞ = 15 m/s.

FIGURE 4.22: Mean streamwise velocity fields in the upstream location at x = 150 mm.

Other than the mean flow fields, the Reynolds shear stress is a required parameter as it is used to determine the skin-friction coefficient contribution from all the quadrant events inside the turbulent boundary layer. The Reynolds shear stress is a function of the velocity fluctuations. The Reynolds shear stress is the average of the multiplied velocity fluctuation. When an outlier is found it often comes with both an erroneous streamwise velocity fluctuation and an erroneous wall-normal velocity fluctuation. Multiplication of outliers makes the Reynolds shear stress convergence extra sensitive to the existence of outliers within the individual flow fields. The Reynolds shear stress is thus computed after outlier removal

using Equation 4.8.

$$\overline{u'v'}(x,y) = \frac{1}{N}\sum_{i=1}^{N} u_i'(x,y)v_i'(x,y) \tag{4.8}$$

The different quadrant contributions by Q1, Q2, Q3 and Q4 can be easily extracted by checking the sign of the velocity fluctuation components during processing. It must then be noted that the different quadrant contributions of the Reynolds shear stress are computed using fewer samples than the total Reynolds shear stress. Applying Equation 4.8 to the individual velocity fluctuations for the same SFPG and SAPG cases as before, the Reynolds shear stress field of Figure 4.23 is obtained.

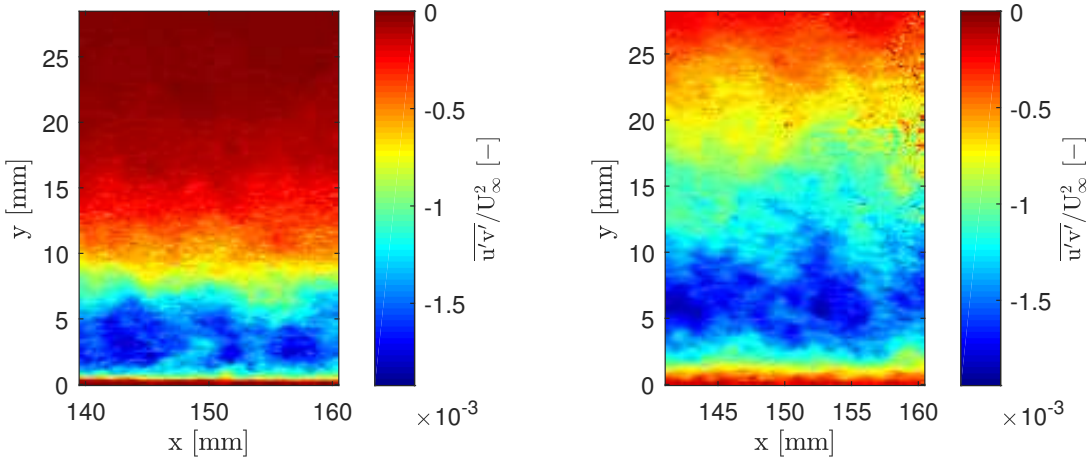

(A) SFPG, U_∞ = 7 m/s. (B) SAPG, U_∞ = 15 m/s.

FIGURE 4.23: Reynolds shear velocity fields in the upstream location at x = 150 mm.

It is shown in Figure 4.23 that the Reynolds shear stress is not smooth with 1,000 samples. In Figure 4.24 the Reynolds shear stress profile is presented in red for a single streamwise location at the center of the field of view. In order to arrive at a smoother profile it is attempted to increase the sample size by taking a bandwidth of streamwise Reynolds shear stress profiles. Instead of taking the location at the center of the field of view, the profile is determined by taking 25% of the field of view before and 25% of the field of view after the center location, in total spanning half (50%) of the field of view. The averaging is built upon the assumption that when changes are observed in the Reynolds shear stress profiles due to the dimples, the effects of the drag reducing properties should also be observable just before and after the wanted location at the center of the field of view. The effect of the averaging is presented in Figure 4.24, where it is shown that the Reynolds shear stress arrives at a smoother profile when the sample size is increased by a bandwidth addition, although variance persists in the profile.

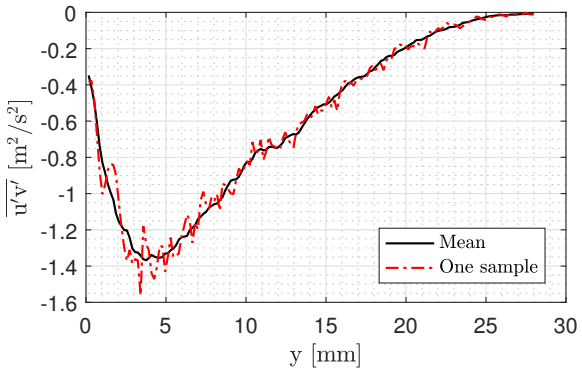

FIGURE 4.24: Increasing sample size by taking a streamwise bandwidth of wall-normal Reynolds shear stress distributions $\overline{u'v'}(y)$.

4.3.2 Uncertainty quantification

Just as for the direct force measurements it is paramount to quantify the significance of a measured value in the flow quantification procedure. For PIV the cross-correlation can be calculated using Equation 4.9 according to Raffel et al. (1998):

$$\epsilon_{cor} = \frac{0.1}{R\Delta t} \tag{4.9}$$

where R is the px/m in the FOV. A conservative estimate of 0.1 pixel is chosen to determine the correlation error. The uncertainty for the mean flow properties and the turbulence properties were noted by Benedict and Gould (1996). For the mean streamwise and wall-normal velocities Equation 4.10:

$$\epsilon_{\overline{u}} = \frac{\sqrt{\overline{u'^2}}}{\sqrt{N}}, \qquad \epsilon_{\overline{v}} = \frac{\sqrt{\overline{v'^2}}}{\sqrt{N}} \tag{4.10}$$

and for the turbulent intensity:

$$\epsilon_{u_{rms}} = \frac{\sqrt{\overline{u'^2}}}{\sqrt{2N}}, \qquad \epsilon_{v_{rms}} = \frac{\sqrt{\overline{v'^2}}}{\sqrt{2N}} \tag{4.11}$$

with finally for the Reynolds shear stress:

$$\epsilon_{\overline{u'v'}} = \frac{\sqrt{1 + R^2_{\overline{u'v'}}}\sqrt{\overline{u'^2}}\sqrt{\overline{v'^2}}}{\sqrt{N}} \tag{4.12}$$

where $R_{\overline{u'v'}}$ is the correlation coefficient:

$$R_{\overline{u'v'}} = \frac{\overline{u'v'}}{\sqrt{\overline{u'^2}}\sqrt{\overline{v'^2}}} \tag{4.13}$$

These equations have been evaluated for all the pressure gradient cases and velocities encountered in the experiment. The highest found values are noted in Table 4.1.

TABLE 4.1: Computed uncertainties

		ZPG		SAPG		SFPG	
$\mathbf{U_\infty}$	**[m/s]**	15 m/s	30 m/s	15 m/s	30 m/s	7 m/s	15 m/s
ϵ_{cor}	[m/s]	0.15	0.27	0.16	0.31	0.10	0.22
$\epsilon_{\overline{u}}/U_\infty$	[-]	0.0032	0.0028	0.0036	0.0025	0.0043	0.0044
$\epsilon_{u_{rms}}/U_\infty$	[-]	0.0023	0.0020	0.0025	0.0018	0.0030	0.0031
$\epsilon_{v_{rms}}/U_\infty$	[-]	0.0010	0.0009	0.0011	0.0010	0.0010	0.0013
$\epsilon_{\overline{u'v'}}/U_\infty^2$	$[\times 10^{-4}]$	1.267	1.125	1.366	1.095	1.447	2.170

4.3.3 Zero pressure gradient

When the deflection is kept at $\varphi = 0°$ the ZPG case is found for which a drag reduction was found in the total drag quantification effort. In Table 4.2 the boundary layer characteristics are shown for both the PIV and HWA measurements while the boundary layer profiles are given in Figure 4.25.

TABLE 4.2: Boundary layer characteristics measured for the ZPG case.

Geometry **[-]**	**x** **[mm]**	$\mathbf{U_\infty}$ [m/s]	δ_{99} **[mm]**	δ^* **[mm]**	θ **[mm]**	**H** **[-]**	$\mathbf{U_e}$ **[m/s]**	$\mathbf{C_p}$ **[-]**
Flat (PIV)	150	15	24.3	4.0	2.97	1.36	15.0	0.00
Dimpled (PIV)	150	15	24.6	4.0	2.96	1.35	15.1	-0.02
Flat (PIV)	150	30	23.9	3.8	2.83	1.34	30.2	-0.01
Dimpled (PIV)	150	30	23.9	3.7	2.80	1.33	30.1	-0.01
Flat (PIV)	520	15	32.2	5.0	3.77	1.33	15.2	-0.03
Dimpled (PIV)	520	15	31.3	4.9	3.67	1.32	15.2	-0.03
Flat (PIV)	520	30	30.6	4.6	3.48	1.31	30.5	-0.03
Dimpled (PIV)	520	30	32.0	4.6	3.55	1.30	30.5	-0.03
Flat (HWA)	520	15	34.0	5.5	3.99	1.38	15.2	-0.02
Dimpled (HWA)	520	15	32.6	5.3	3.91	1.36	15.2	-0.02
Flat (HWA)	520	30	28.5	4.6	1.35	1.35	30.9	-0.06
Dimpled (HWA)	520	30	29.0	4.6	1.34	1.34	30.9	-0.06

The mean velocity profiles in Figure 4.25a agree well between the PIV and the HWA measurements. A small offset exists between the values measured by the HWA and the PIV measurements, where the PIV measurements show higher values for δ^* and smaller values for θ, which then result in a higher shape factor H. A slightly higher freestream velocity is observed for the U_∞ = 30 m/s, which could be due to slight differences in measurement location between the HWA and the PIV measurement.

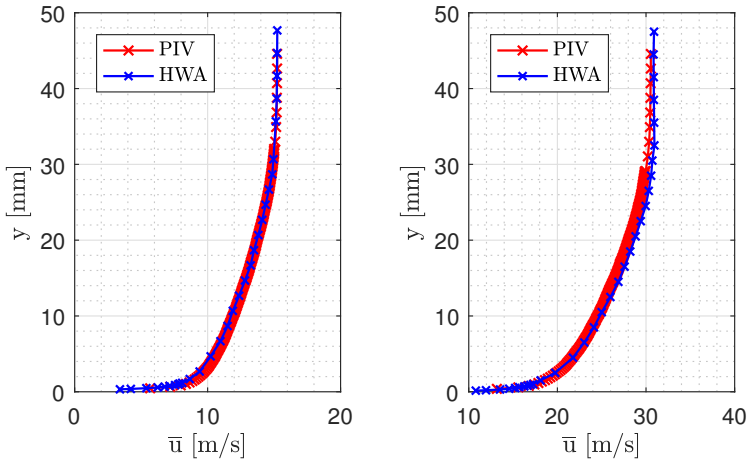

(A) U_∞ = 15 m/s. (B) U_∞ = 30 m/s.

FIGURE 4.25: Comparison of flat plate mean velocity profiles for the ZPG case.

As is furthermore expected, the boundary layer thickness increases downstream and accompanied with this is a slight rise in the freestream velocity U_e due to the contraction of the section area due the boundary layer growth. The pressure coefficient C_p is slightly lower than zero, indicating that the flow is accelerating which is in correspondence with the aforementioned. Pope (2000) reports that the typical shape factor H measured for a ZPG turbulent boundary layer is around 1.3. Looking at the shape factor in Table 4.2 is is found that for most profiles this is the case, with slightly higher values reported for upstream locations at low velocities. Only small changes are observed for both δ_{99}, δ^* and H. The skin-friction can be derived by examining the streamwise change in the momentum thickness $\mathrm{d}\theta/\mathrm{dx}$, but the value stays nearly constant between the dimpled and the flat case indicating that the dimpled surface has only a minor effect. In the next section the boundary layer is inspected in more detail to derive the skin-friction using the law of the wall as defined by Spalding (1961).

Skin-friction coefficient. One common feature of a drag-reduced flow is that the logarithmic part of the non-dimensionalized has an upward shift by the addition ΔB to the wall-intercept value B in the law of the wall by Spalding (1961). Both for the riblets and the oscillating wall drag reductions are always accompanied by positive values for ΔB.

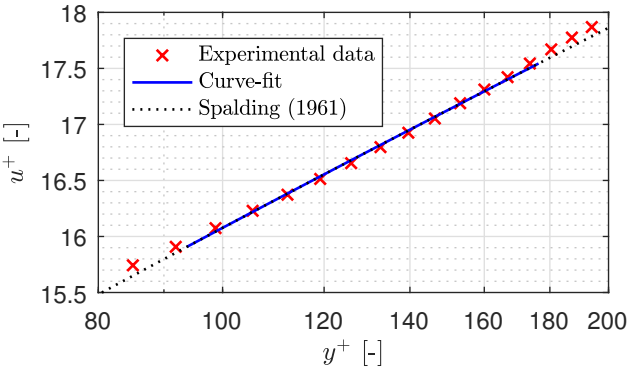

FIGURE 4.26: Curve-fitting the TBL profile with Spalding's law of the wall.

In order to fit the boundary layer profile to the law of the wall with an intercept addition ΔB, the law of the wall by Spalding (1961) is rewritten by reversing the wall-coordinate non-dimensionalization such that the wall-normal position y can be described as a function

of the parameters that are known from experiment (mean velocity profile $\overline{u}$, freestream velocity U_e, kinematic viscosity ν, Von Karman constant κ and wall intercept value B) and the parameters that are required (skin-friction coefficient C_f and wall intercept change ΔB). This rewritten expression is given in Equation 4.14. When a flat plate is considered it is assumed that $\Delta B = 0$.

$$y = \frac{2\overline{u}\nu}{U_e^2 C_f} + \frac{\nu}{U_e}\sqrt{\frac{2}{C_f}}e^{-\kappa(B+\Delta B)}\left[e^{\frac{\kappa\overline{u}}{U_e}\sqrt{\frac{C_f}{2}}} - 1 - \frac{\kappa\overline{u}}{U_e}\sqrt{\frac{C_f}{2}} - \frac{1}{2}\left(\frac{\kappa\overline{u}}{U_e}\sqrt{\frac{C_f}{2}}\right)^2 - \frac{1}{6}\left(\frac{\kappa\overline{u}}{U_e}\sqrt{\frac{C_f}{2}}\right)^3\right] \tag{4.14}$$

Using a nonlinear least-squares fitting algorithm in MATLAB, all the known parameters are fitted to the rewritten law of the wall to yield the wanted parameters C_f and ΔB. To have a notion of the curve fitting error, the squared residuals of the fit for different values for ΔB and C_f are given in Figure 4.27. From this it is observed that a minimum squared residual value is found at $C_f = 3.17$ and $\Delta B = 0.11$. Figure 4.27 exemplifies that small changes in the experimental y that are compared to the fitted y of Equation 4.14 have an effect on the values for C_f and ΔB found by the curve-fitting algorithm.

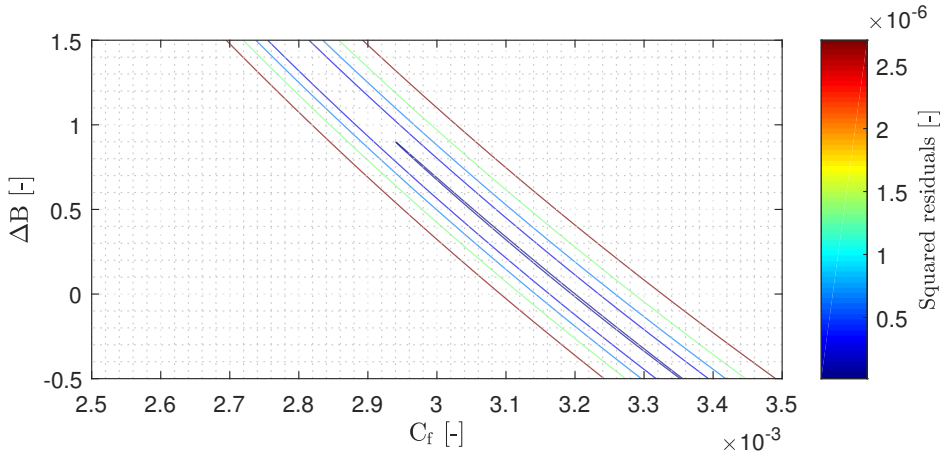

FIGURE 4.27: Squared residuals as fitting parameter for the dimpled plate, upstream at $U_\infty = 15$ m/s as a function of ΔB and C_f. Smallest contour line associated with the magnitude of 1.1 times the minimum squared residual.

The first case that is considered for a shift in the logarithmic layer is the ZPG case. The boundary layer profiles non-dimensionalized in wall units are shown in Figure 4.28. For all the considered cases in Figure 4.28 it is observed that the logarithmic layer of the measured velocity profiles fits well to the law of the wall by Spalding (1961). Changes start to exist in the buffer layer, where it is observed that the deviations are most profound for the case considered in Figure 4.28c. As the fitting procedure is based on a finite number of points there exists a slight fitting error. As the profiles in wall units are plotted on a logarithmic axis, slight differences in skin-friction coefficient are exaggerated when non-dimensionalizing the spatial coordinate y to y^+. When going upwards in the velocity profile the advent of the turbulent wake region is observed where the profile starts to deviate from the linear region of the law of the wall. It is observed that for all positions and upstream velocities changes in the wall intercept value are small.

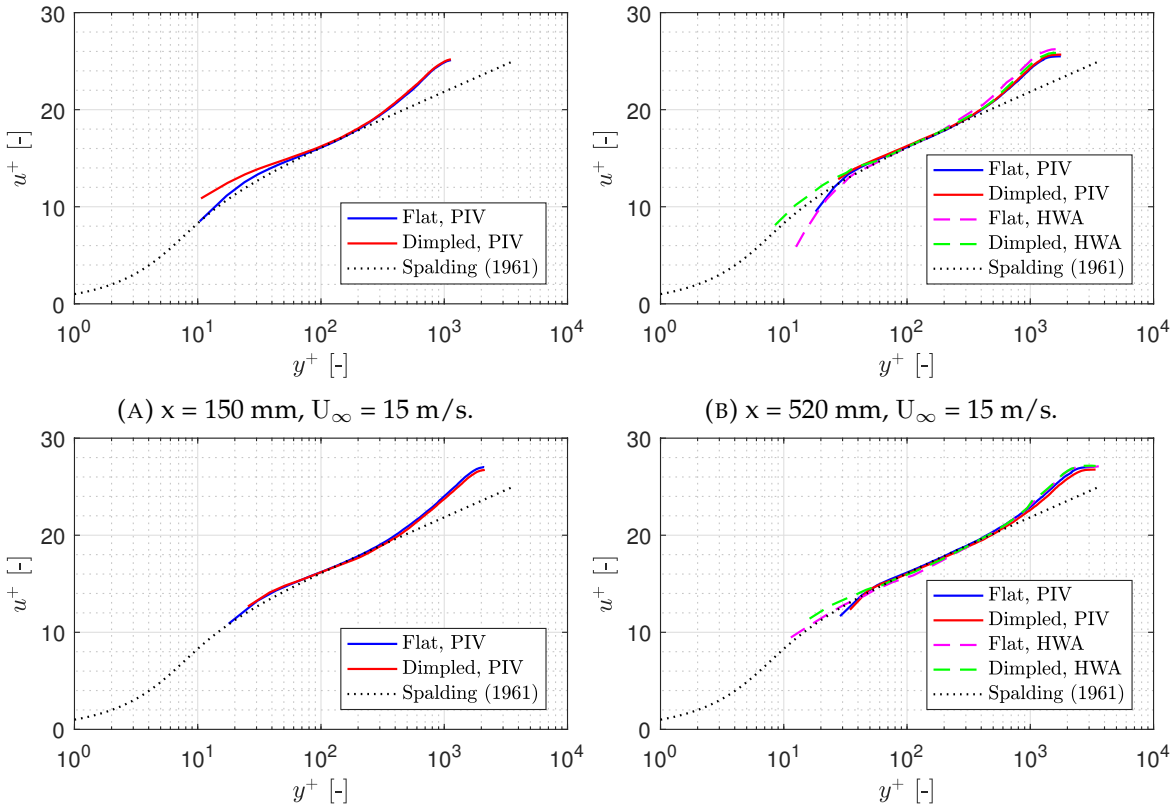

(A) x = 150 mm, U_∞ = 15 m/s.

(B) x = 520 mm, U_∞ = 15 m/s.

(C) x = 150 mm, U_∞ = 30 m/s.

(D) x = 520 mm, U_∞ = 30 m/s.

FIGURE 4.28: Boundary layer profiles in wall coordinates for the ZPG case.

TABLE 4.3: Clauser fit of the boundary layer profiles non-dimensionalized in wall units for the ZPG case.

				HWA		PIV	
Geometry [-]	**x [mm]**	**U_∞ [m/s]**	**Re_D [10^4]**	**C_f [10^{-3}]**	**ΔB [–]**	**C_f [10^{-3}]**	**ΔB [–]**
Flat	150	15	1.99	-	-	3.20	0
Dimpled	150	15	1.99	-	-	3.17	0.11
Δ[%]	**-**	**-**	**-**	**-**	**-**	**-0.9**	**-**
Flat	520	15	1.99	3.00	0	3.10	0
Dimpled	520	15	1.99	3.00	-0.09	3.07	0.09
Δ[%]	**-**	**-**	**-**	**0.0**	**-**	**-0.8**	**-**
Flat	150	30	3.99	-	-	2.75	0
Dimpled	150	30	3.99	-	-	2.81	-0.17
Δ[%]	**-**	**-**	**-**	**-**	**-**	**2.2**	**-**
Flat	520	30	3.99	2.67	0	2.75	0
Dimpled	520	30	3.99	2.71	-0.09	2.80	-0.16
Δ[%]	**-**	**-**	**-**	**0.1**	**-**	**1.8**	**-**

In Table 4.3 the skin-friction coefficient measured from the fitting procedure are shown together with the changes in wall intercept value B. It is observed that the skin-friction coefficient of both the dimpled and flat plates decreases when traversing in the downstream direction, as is generally expected for a ZPG boundary layer. It is found in Table 4.3 that the

skin-friction coefficient changes minimally for the boundary layer profiles that were measured with the HWA technique. For the PIV profiles it is observed that for U_∞ = 15 m/s a small skin-friction reduction is observed with a positive value for ΔB, indicating a small upwards shift of the logarithmic layer, while a skin-friction increase is observed for the U_∞ = 30 m/s case. This is in contrast with the measurements from the DFM campaign which show a drag increase for low Reynolds number (also due to pressure drag) and a reduction for the highest considered Reynolds number. For the HWA measurements a smaller skin-friction coefficient is found, for both upstream velocities. It must however be noted that for the HWA campaign a smaller amount of measurement points is used compared to the PIV campaign.

Reynolds shear stress. A quadrant decomposition is performed in which the Reynolds shear stress is decomposed in four quadrants representing each positive and negative combination of the turbulent velocity fluctuations. The resulting Reynolds shear stress are then non-dimensionalized by dividing by the square of the upstream velocity U_∞. The turbulent contribution to the skin-friction is computed using Equation 4.15 as by Mehdi et al. (2014).

$$C_{f,turb} = -\frac{4}{y_t^2 U_\infty^2} \int_0^{y_t} (y_t - y)\overline{u'v'}\mathrm{d}y \tag{4.15}$$

Equation 4.15 states that both increases in Q1 and Q2 as decreases in Q2 and Q4 lead to skin-friction reductions. Equation 4.15 is then applied to the averaged Reynolds shear stress profiles. In Figure 4.29 the averaged shear stress profiles are presented for both the flat and dimpled cases for both different locations and upstream velocities for the ZPG case.

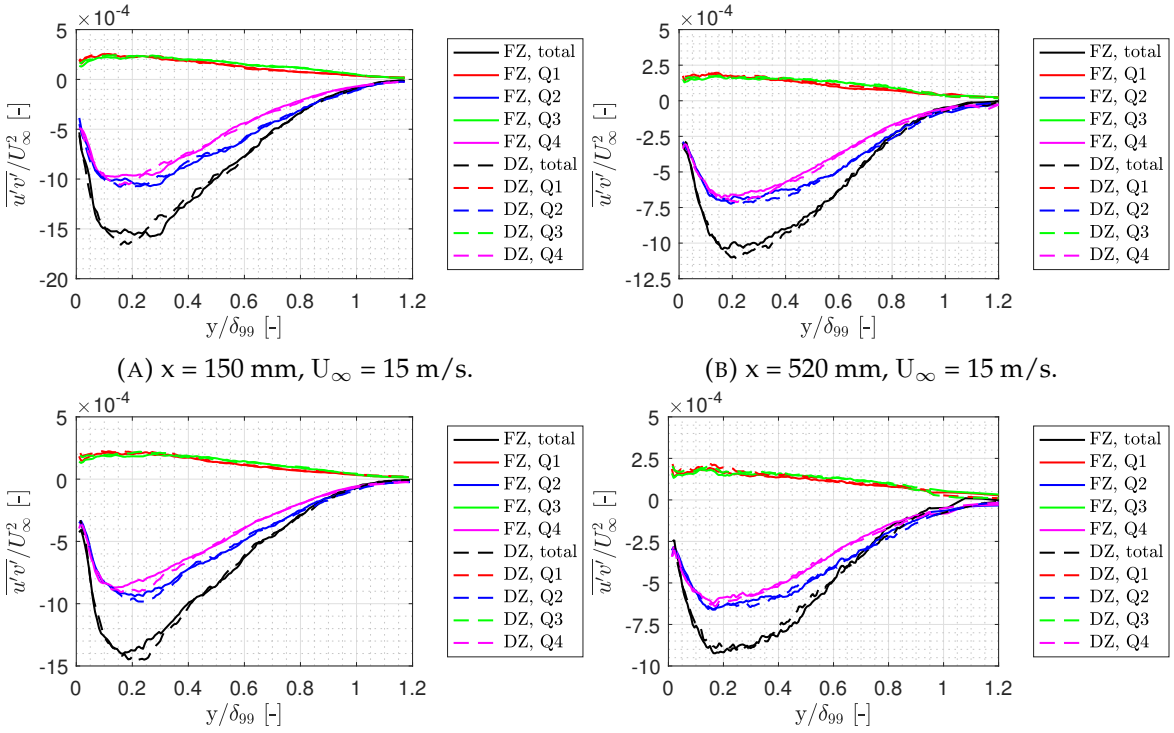

(A) x = 150 mm, U_∞ = 15 m/s.

(B) x = 520 mm, U_∞ = 15 m/s.

(C) x = 150 mm, U_∞ = 30 m/s.

(D) x = 520 mm, U_∞ = 30 m/s.

FIGURE 4.29: Reynolds shear stress profiles and quadrant contributions for the ZPG case.

As a general observation it is observed that the Q2 and Q4 quadrants make up the largest

part of the Reynolds shear stress, having the highest skin-friction contribution. Moving from the wall upwards the Reynolds shear stresses increase until a peak of all the Reynolds shear stress components around $y/\delta_{99} = 0.2$. After this peak the Reynolds shear stress decreases towards the freestream turbulence values of around zero. It must be noted that all the measured values are still unconverged, even after increasing the sample size with the procedure described above. For the cases considered in Figure 4.29a, 4.29b and 4.29c it is found that the Reynolds shear stress is most impacted at the peak value. For the dimpled (dashed) cases the total Reynolds shear stress is seen to increase before the flat plate peak, and reduced after it. Outside of the peak range the Reynolds shear stresses are approximately equal for all cases. For the case considered in Figure 4.29d it is observed that the Reynolds shear stress profiles show minor changes throughout the entire profile. Using the Reynolds shear stress integration routine of Equation 4.15 the results in Table 4.7 are obtained: the profiles are quantified into a skin-friction coefficient.

TABLE 4.4: Skin-friction contributions of the Reynolds shear stress for the ZPG case.

Geometry [-]	**x [mm]**	$\mathbf{U_\infty}$ $[\mathbf{m/s}]$	$\mathbf{Re_D}$ $[\mathbf{10^4}]$	$\mathbf{C_{f,turb}}$ $[\mathbf{10^{-3}}]$	$\mathbf{C_{f,Q1}}$ $[\mathbf{10^{-3}}]$	$\mathbf{C_{f,Q2}}$ $[\mathbf{10^{-3}}]$	$\mathbf{C_{f,Q3}}$ $[\mathbf{10^{-3}}]$	$\mathbf{C_{f,Q4}}$ $[\mathbf{10^{-3}}]$
Flat	150	15	1.99	2.10	-0.34	1.48	-0.35	1.31
Dimpled	150	15	1.99	2.08	-0.34	1.47	-0.36	1.32
Δ [%]	-	-	-	-1.1	0.8	-1.0	2.9	0.4
Flat	520	15	1.99	1.27	-0.24	0.93	-0.25	0.83
Dimpled	520	15	1.99	1.30	-0.25	0.95	-0.25	0.86
Δ [%]	-	-	-	2.3	6.2	2.1	2.9	3.8
Flat	150	30	3.99	1.74	-0.30	1.24	-0.31	1.11
Dimpled	150	30	3.99	1.77	-0.32	1.26	-0.32	1.14
Δ [%]	-	-	-	1.5	6.1	2.0	5.1	3.1
Flat	520	30	3.99	1.07	-0.24	0.82	-0.25	0.74
Dimpled	520	30	3.99	1.06	-0.26	0.83	-0.26	0.75
Δ [%]	-	-	-	-1.2	8.0	1.1	3.9	0.9

A total turbulent skin-friction reduction is found for the $U_\infty = 15$ m/s in the upstream position, and one which is more profound for the downstream $U_\infty = 30$ m/s location. A drag increase is observed for the downstream $U_\infty = 15$ m/s case and the upstream $U_\infty = 30$ m/s case. Looking the Reynolds shear stress profile it is however observed that there exists little variation between the profiles, and indeed it is observed that only the peak is increased somewhat for the dimpled cases, while the development of the remaining boundary layer stays equal. It is noted that the noise of the profile impedes the integration routine, and changes in the skin-friction coefficients can also be caused by integration of disturbances from the mean profile due to this noise.

For a different quadrant analysis the instantaneous fluctuations can be examined. Wallace (2016) describes a straightforward method in which the individual velocity fluctuation pairs are plotted on the instantaneous velocity fluctuation axes. The data points are available from the PIV measurements. The sample size was previously increased to include half of the field of view: for both the dimpled and the flat plate this then yields the same amount of sample points. By sorting the fluctuations into bins and normalizing the occurence in each bin the probability distribution can be computed.

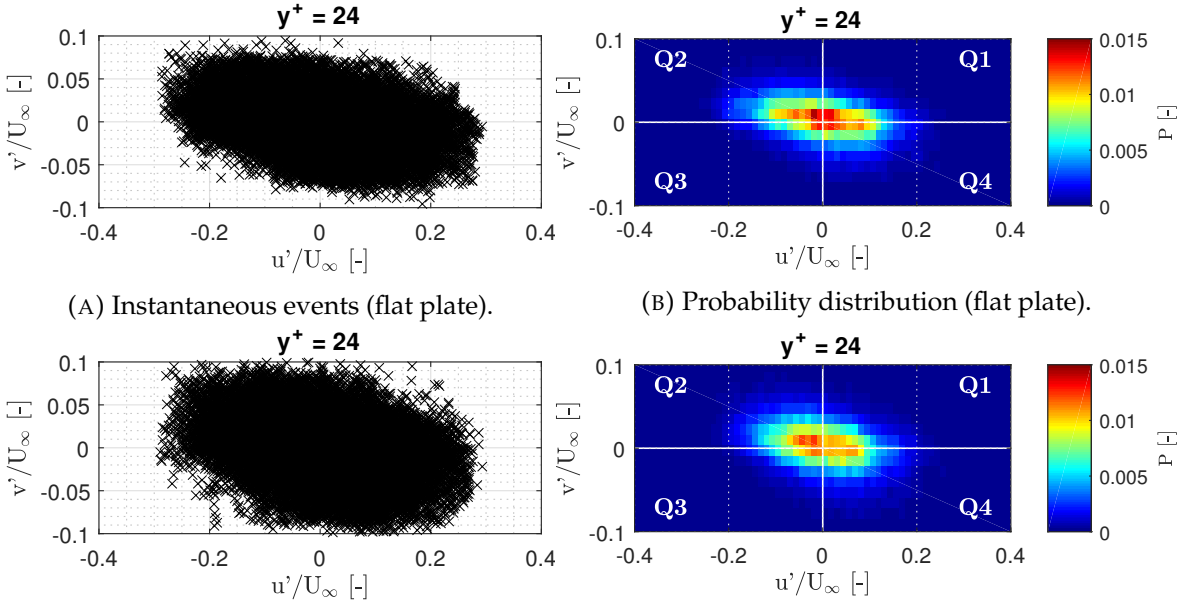

(A) Instantaneous events (flat plate).

(B) Probability distribution (flat plate).

(C) Instantaneous events (dimpled plate).

(D) Probability distribution (dimpled plate).

FIGURE 4.30: Quadrant analysis of at $y^+ = 24$ in the buffer layer for the ZPG case, downstream location at $U_\infty = 15$ m/s.

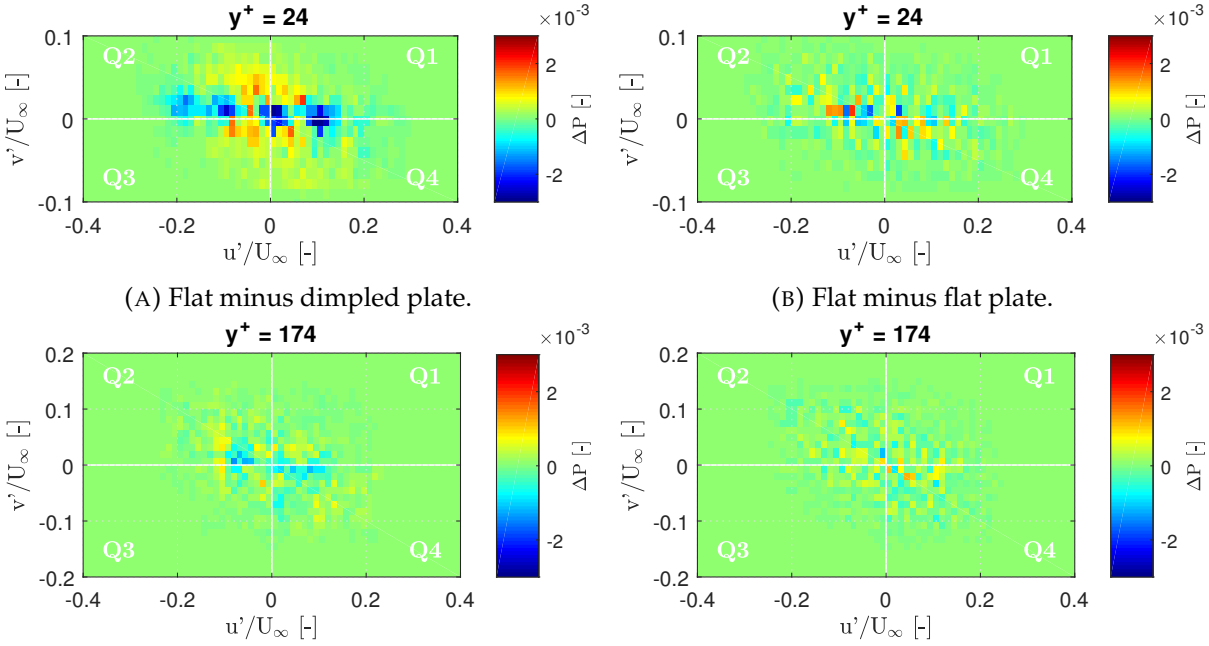

(A) Flat minus dimpled plate.

(B) Flat minus flat plate.

(C) Flat minus dimpled plate.

(D) Flat minus flat plate.

FIGURE 4.31: Quadrant probability difference for the ZPG case, downstream location at $U_\infty = 15$ m/s.

In Figure 4.31 a quadrant analysis is presented for both the flat plate and the dimpled plate for the ZPG case in the buffer layer at the same y^+ coordinate, including both the instantaneous events in their associated probability P. Yakeno et al. (2014) proposes that the near-wall events are manipulated here for an oscillating wall. It is generally found that the quadrant events are tilted towards the Q2-Q4 axis. The bins spacing for the probability of both the

dimpled and the flat plate have been chosen to be equal such that a subtraction can be performed to investigate the relative changes in probability ΔP. In Figure 4.31b the probability distribution for the dimpled plate (Figure 4.30c) is subtracted from the flat plate probability distribution (Figure 4.30a) to investigate relative changes that occur due to application of a dimpled surface. From Figure 4.31b it is then observed that around the u'-axis the quadrant events are diminished while they are enhanced further away from the u'-axis. Increases in Q1 and Q3 events lead to reduced Reynolds shear stresses while decreases in Q2 and Q4 events lead to reduced Reynolds shear stresses. These increases and decreases are small (in the order of tenths of a percent with maximum reduction of -0.3% in the Q4 region) and annulled by subsequent decreases and increases in other areas of the quadrant regions. Going upwards from the buffer layer, the peak location $y/\delta_{99} = 0.2$ at $y^+ = 174$ is investigated as well in Figure 4.31c. At this location the differences in probability become significantly smaller compared to the $y^+ = 24$ location, with differences measured being within uncertainty.

Turbulence intensity. In Figure 4.32 the turbulence intensities in the upstream position at x = 150 mm are shown. As is expected from literature there exists a strong peak in the streamwise fluctuation component u close to the wall, and a peak at $y/\delta_{99} = 0.2$ for the wall-normal velocity fluctuation as also reported by Klebanoff (1955).

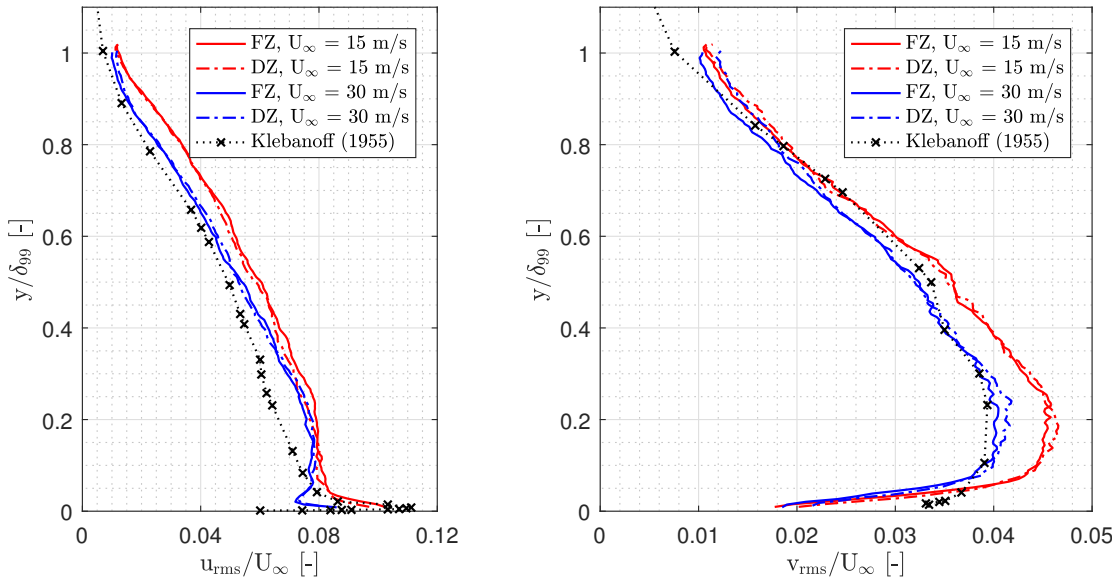

(A) u_{rms}. (B) v_{rms}.

FIGURE 4.32: Turbulent intensities for the ZPG case at x = 150 mm.

For the streamwise velocity component the turbulent intensities in Figure 4.32a for the dimpled case the peak is not captured totally, but there is no significant change trough out the entire boundary layer profile, as they are all within statistical uncertainty. The wall-normal velocity fluctuation component peak is however completely captured, but as is found in Figure 4.32b no significant changes exist in the profile between the flat and dimpled plate, with a hint being present that the dimpled profile has a slightly higher v_{rms} peak (although within statistical uncertainty).

The HWA measurements in the downstream position at x = 520 mm captures the streamwise component only, but due to the close proximity to the wall the HWA measurements capture the peak better than the PIV measurements for the $U_\infty = 15$ m/s case. In Figure

4.33 it is observed that just as for the upstream position no significant changes exists across the boundary layer profile for both considered upstream velocities as they are encountered for other drag-reducing methods. For these drag-reducing methods a general diminishing trend is observed for the entire turbulence intensity profile compared to the flat plate case, and thus as the peak is not captured it can be deduced from the rest of the profile that the changes in peak value are minor.

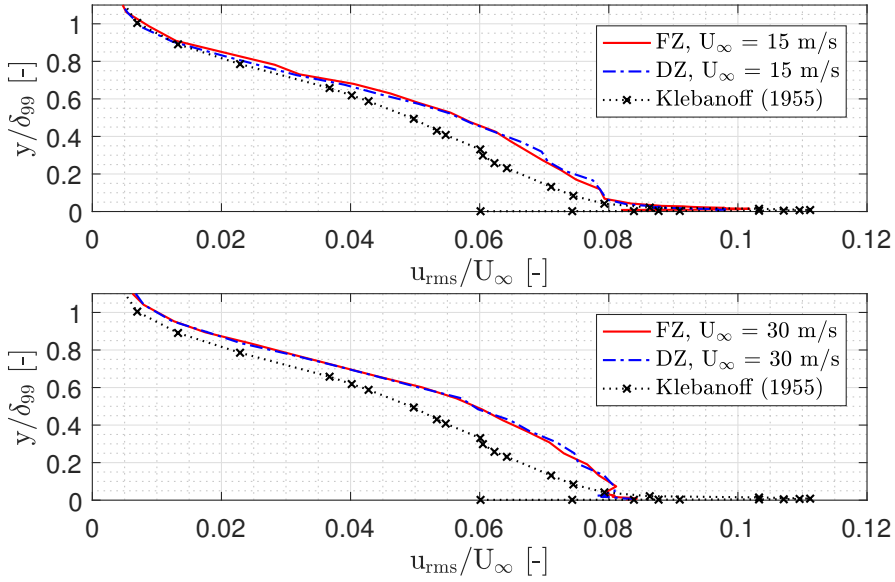

FIGURE 4.33: HWA streamwise turbulent intensities for the ZPG case in the downstream position at x = 520 mm.

4.3.4 Strong favorable pressure gradient

When an inward deflection is applied to the test plate the test section area contracts and the flow has to accelerate due to mass conservation. In this section the boundary layer properties are determined for the SFPG case, for which it was observed that the flow leaves through the side gaps of the test plate, indicating that mass conservation is not totally valid. Looking at Figure 4.34 it is found that the flow is indeed accelerating.

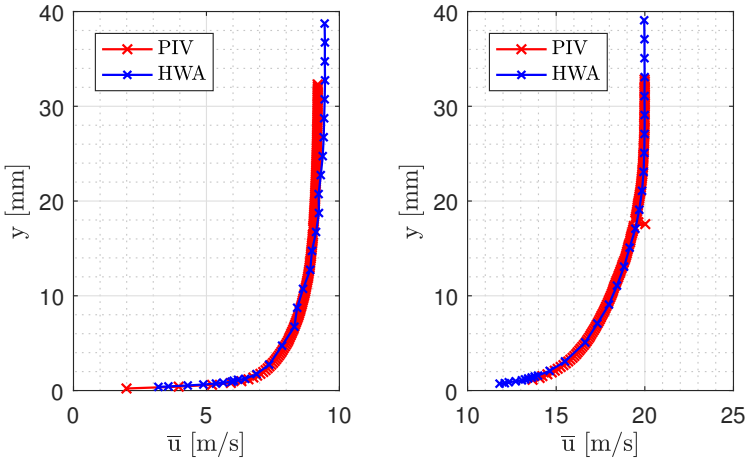

(A) U_∞ = 7 m/s. (B) U_∞ = 15 m/s.

FIGURE 4.34: Comparison of flat plate mean velocity profiles for the SFPG case.

In contrast to the ZPG case it is expected from the aerodynamic boundary layer algorithm that the boundary layer is becoming smaller in the downstream direction. Table 4.5 it is found that the boundary layer grows. This growth is most likely caused by the boundary layer thickness determination algorithm, which looks at the $y_{u/U_e=0.99}$ point. As there exists a high gradient in the SFPG turbulent boundary layer a point slighly lower than the $u/U_e = 0.99$ point leads to a relative high change in boundary layer thickness.

TABLE 4.5: Boundary layer characteristics measured for the SFPG case.

Geometry [-]	**x** [mm]	$\mathbf{U_\infty}$ [m/s]	δ_{99} [mm]	δ^* [mm]	θ [mm]	**H** [-]	$\mathbf{U_e}$ [m/s]	**K** [$\times 10^{-6}$]	$\mathbf{C_p}$ [-]
Flat (PIV)	150	7	15.4	2.1	1.50	1.39	7.5	1.93	-0.15
Dimpled (PIV)	150	7	14.7	1.9	1.41	1.34	7.6	2.31	-0.16
Flat (PIV)	150	15	22.2	3.1	2.39	1.29	16.0	0.74	-0.14
Dimpled (PIV)	150	15	21.7	3.0	2.31	1.28	16.0	0.81	-0.13
Flat (PIV)	520	7	16.7	1.6	1.23	1.30	9.1	3.21	-0.69
Dimpled (PIV)	520	7	16.8	1.6	1.21	1.29	9.3	3.88	-0.77
Flat (PIV)	520	15	20.2	1.9	1.57	1.19	19.0	1.92	-0.60
Dimpled (PIV)	520	15	19.6	2.0	1.64	1.20	19.1	1.60	-0.62
Flat (HWA)	520	7	24.5	2.4	1.9	1.24	9.2	-	-0.86
Dimpled (HWA)	520	7	27.0	3.0	2.3	1.27	9.4	-	0.82
Flat (HWA)	520	15	20.2	2.2	1.8	1.22	19.1	-	0.79
Dimpled (HWA)	520	15	20.2	2.3	1.9	1.22	19.6	-	0.71

In Table 4.5 the boundary layer characteristics are presented. For the SFPG case the acceleration is accompanied by a negative pressure coefficient C_p. To investigate the laminarization properties of the flow the acceleration parameter K is also presented in Table 4.5. A small velocity discrepancy is observed for the U_∞ = 7 m/s between the PIV and HWA measurements in Figure 4.34a. The mean velocity profile measured by the HWA technique shows a slightly higher freestream velocity accompanied by a higher boundary layer thickness, resulting in higher values for the displacement thickness δ^* and smaller values for momentum thickness θ, resulting in a lower boundary layer shape factor H. It is however shown that even though there are differences between the techniques, the effect on the shape factor by the favorable pressure gradient is clear, as it drops below the value of H = 1.3 reported by Pope (2000) for the typical ZPG turbulent boundary layer, and at smaller values than measured for the ZPG case in the current experiment. It is reported in literature that for K > $3.5\times10^{-}6$ the flow will start to relaminarize. It observed from Table 4.5 that the dimple increases the acceleration parameter K, indicating possible favorable effect of a dimple on the relaminarization process under a favorable pressure gradient as reported by Sreenivasan (1981). This is however not found for the downstream U_∞ = 30 m/s case.

Skin-friction coefficient. The turbulent boundary layer profile contains a clear turbulent wake for the ZPG case, and it is observed in Figure 4.35 that the wake is subdued in the advent of a favorable pressure gradient, indicating the partial cessation of turbulence. The acceleration is accompanied by a decrease in the turbulent wake in the upper layer of the turbulent boundary layer. This change is observed in Figure 4.35 to be most profound for the smallest upstream velocity of U_∞ = 7 m/s, as the the turbulent wake is still observable in in the upstream position at x = 150 mm for U_∞ = 7 m/s at the upstream position. Once again it is shown that the determination of the skin-friction fitting procedure leads to an erroneous fit of the viscous layer, with deviations shown for both the PIV and HWA measurements.

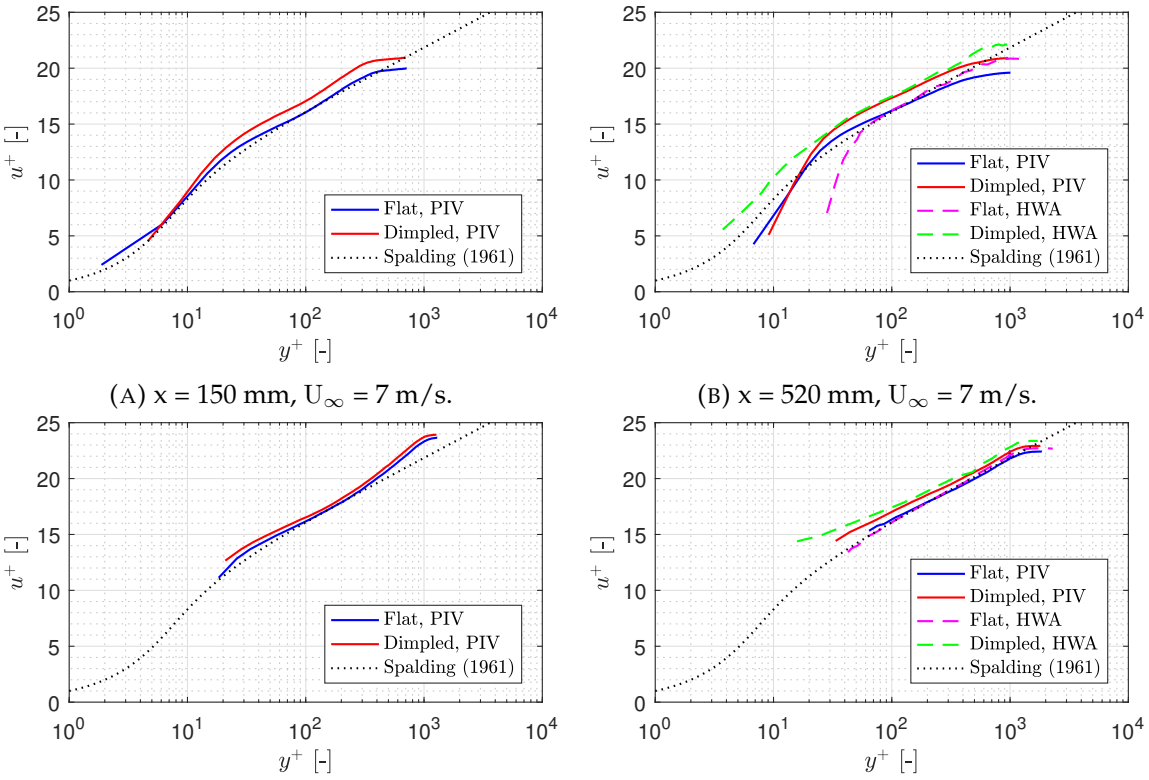

(A) x = 150 mm, U_∞ = 7 m/s.

(B) x = 520 mm, U_∞ = 7 m/s.

(C) x = 150 mm, U_∞ = 30 m/s.

(D) x = 520 mm, U_∞ = 30 m/s.

FIGURE 4.35: Boundary layer profiles in wall coordinates for the SFPG case.

A good fit is observed for the logarithmic layer for the flat plate. When the same fitting procedure is used, it immediately becomes apparent that there exists an upwards shift of the logarithmic layer for both the PIV and HWA measurements for the dimpled case compared to the flat plate, being most profound for the smaller upstream velocity of U_∞ = 7 m/s. Another approach to see if the logarithmic layer is shifted upwards is by taking a look at the mean velocity profiles that are not non-dimensionalized with wall units. It is reported by Choi (1989) that the upwards shift of the logarithmic layer is also observable in the mean velocity profile (Figure 2.10b) by an inflection of the velocity profile. In Figure 4.36 the velocity profiles are presented in where the upstream velocity U_∞ and the boundary layer thickness δ_{99} are used instead of the wall units to non-dimensionalize the profiles.

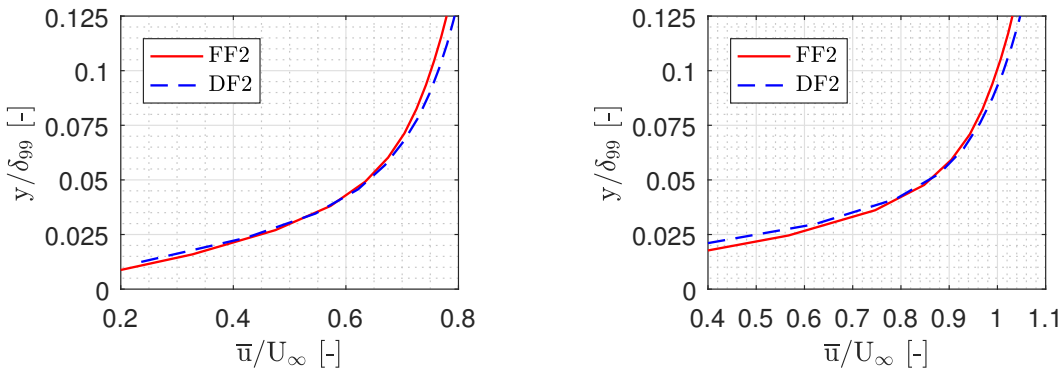

(A) x = 150 mm.

(B) x = 520 mm.

FIGURE 4.36: Mean velocity profiles for the SFPG case for U_∞ = 7 m/s.

TABLE 4.6: Clauser fit of the boundary layer profiles non-dimensionalized in wall units for the SFPG case.

				HWA		PIV	
Geometry [-]	**x [mm]**	**U_∞ [m/s]**	**Re_D [10^4]**	**C_f [10^{-3}]**	**ΔB [−]**	**C_f [10^{-3}]**	**ΔB [−]**
Flat	150	7	0.93	-	-	5.09	0
Dimpled	150	7	0.93	-	-	4.63	1.1
Δ[%]	**-**	**-**	**-**	**-**	**-**	**-9.0**	**-**
Flat	520	7	0.93	4.73		5.31	0
Dimpled	520	7	0.93	4.02	1.16	4.68	1.1
Δ[%]	**-**	**-**	**-**	**-14.9**	**-**	**-11.8**	**-**
Flat	150	15	1.99	-	-	3.60	0
Dimpled	150	15	1.99	-	-	3.51	0.4
Δ[%]	**-**	**-**	**-**	**-**	**-**	**-2.5**	**-**
Flat	520	15	1.99	3.88		4.03	0
Dimpled	520	15	1.99	3.66	0.81	3.85	0.7
Δ[%]	**-**	**-**	**-**	**-5.7**	**-**	**-4.5**	**-**

It is observed in Figure 4.36 that for both the upstream and downstream location an inflection points exists in the velocity profile where it is observed that the decrease in the velocity profile is shifted leading to an upwards shift of the logarithmic layer. In Table 4.6 the actual computed shifts are given and observed to be larger than for the ZPG case. The computed wall intercept changes ΔB are in the order of 1, as is also reported for drag-reducing riblets by Choi (1989) and compliant coatings by Choi et al. (1993). This effect is however not found for the ZPG case, and combined with the higher values for K a probable cause is that the dimple assists the relaminarization effort of the favorable pressure gradient.

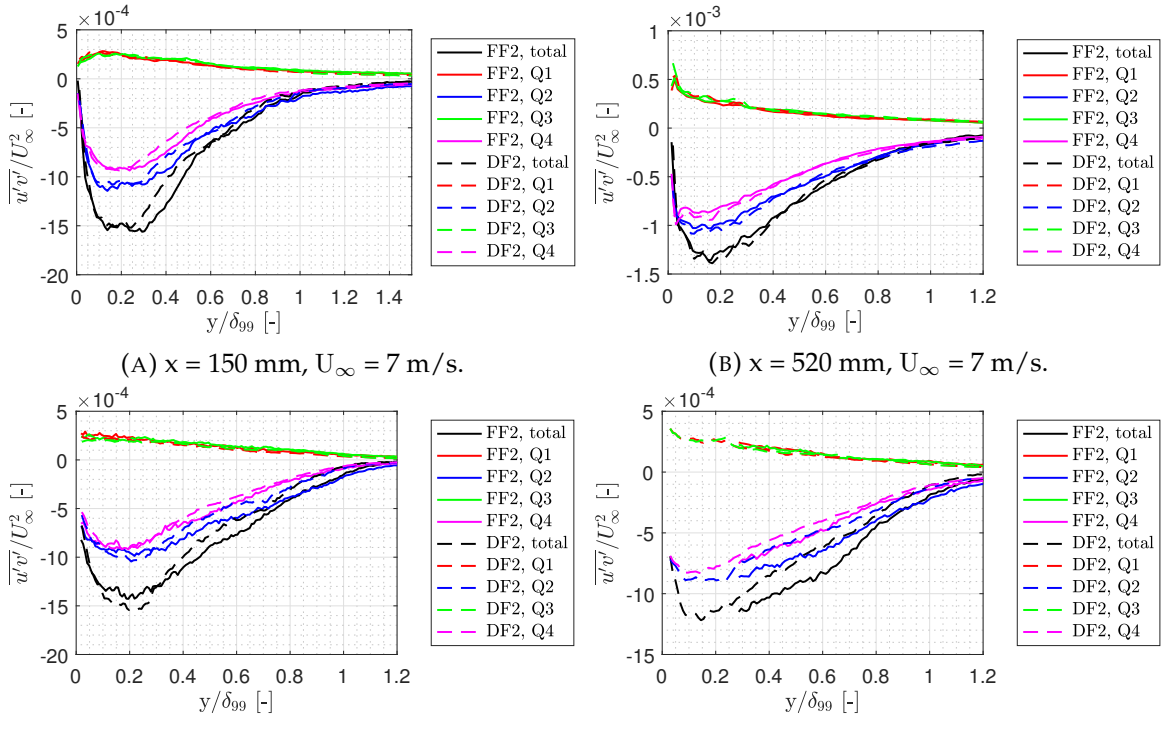

(A) x = 150 mm, U_∞ = 7 m/s.

(B) x = 520 mm, U_∞ = 7 m/s.

(C) x = 150 mm, U_∞ = 15 m/s.

(D) x = 520 mm, U_∞ = 15 m/s.

FIGURE 4.37: Reynolds shear stress profiles and quadrant contributions for the SFPG case.

Reynolds shear stress. The Reynolds shear stresses are presented in Figure 4.37. Compared to the ZPG case it is found that the Reynolds shear stress peak is located closer to the wall, and overall Reynolds shear stress values go to their freestream levels faster than the ZPG case, indicating that turbulence is maintained closer to the wall compared to the ZPG case. Due to the occurrence of persistent outliers the near wall region of the U_∞ = 15 case in the downstream region is not captured accurately for the flat plate.

The effect of the dimple is found to be beneficial for the upstream position for both upstream velocities. For the downstream location the difference is small for the U_∞ = 7 m/s case, and for the U_∞ = 7 m/s the near wall region is not fully captured due to persistent outlier. It can however be noted that in the latter case a reduction is observed for both the Reynolds shear stress profile that is captured. When the integration routine is performed to determine the skin-friction coefficient, it observed that for the upstream case at U_∞ = 7 m/s a skin-friction reduction is attained, as well as for the upstream location of the U_∞ = 15 m/s case. No considerable changes in skin-friction are found for the downstream locations, and for the downstream case of U_∞ = 15 m/s no changes in the near-wall region can be determined (although the rest of the profile shows a clear reduction). Once again it must be noted that noise of the profile inhibits proper computation of the skin-friction.

TABLE 4.7: Skin-friction contributions of the Reynolds shear stress for the SFPG case.

Geometry [-]	**x** [mm]	$\mathbf{U_\infty}$ [m/s]	$\mathbf{Re_D}$ [10^4]	$\mathbf{C_{f,turb}}$ [10^{-3}]	$\mathbf{C_{f,Q1}}$ [10^{-3}]	$\mathbf{C_{f,Q2}}$ [10^{-3}]	$\mathbf{C_{f,Q3}}$ [10^{-3}]	$\mathbf{C_{f,Q4}}$ [10^{-3}]
Flat	150	7	0.93	2.23	-0.39	1.65	-0.40	1.36
Dimpled	150	7	0.93	2.10	-0.39	1.59	-0.40	1.31
Δ [%]	-	-	-	-5.5	0.4	-4.1	2.3	-3.3
Flat	520	7	0.93	1.83	-0.43	1.48	1.24	3.58
Dimpled	520	7	0.93	1.85	-0.46	1.52	1.28	3.37
Δ [%]	-	-	-	1.2	8.4	2.2	3.5	-5.9
Flat	150	15	1.99	2.07	-0.36	1.50	-0.36	1.30
Dimpled	150	15	1.99	2.04	-0.32	1.43	-0.32	1.25
Δ [%]	-	-	-	-1.5	-12.8	-4.9	-13.0	-3.9
Flat	520	15	1.99	1.88	-0.64	1.67	-0.64	1.49
Dimpled	520	15	1.99	1.68	-0.38	1.30	-0.39	1.16
Δ [%]	-	-	-	-10.3	-40.1	-22.1	-39.1	-22.2

Just as for the ZPG case in the instantaneous probability difference ΔP can be determined to check if the quadrant events are changed close to the wall. In Figure 4.38 the difference is shown for the upstream location together with a measure of uncertainty by including the probability difference using just one flat plate data set. Since the same y^+ can not be attained due to the measurement resolution, the closest values of y^+ are chosen to do a comparison. Once again it is observed that there is some scattering of the events, with a reduction of events around the u'-axis and an increase further away of the u'-axis, although it must be noted that the differences are within half a percent and close to the uncertainty margins that are in the same order.

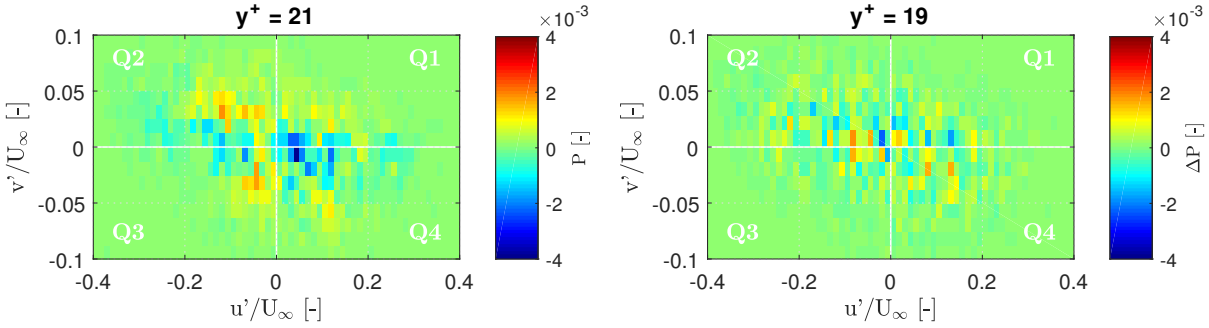

(A) Flat minus dimpled plate. (B) Flat minus flat plate.

FIGURE 4.38: Quadrant probability difference for the SFPG case, upstream location at $U_\infty = 7$ m/s.

Turbulence intensity. The turbulence intensity is presented for the SFPG case in Figure 4.39. In Figure 4.39 it is seen that the dimple reduces the streamwise velocity peak for the $U_\infty = 7$ m/s case, whereas the peak of the $U_\infty = 15$ m/s case is not accurately captured due to its close proximity to the wall. All the turbulence intensities presented in Figure 4.39 show a smaller value for the dimpled case. This is the case for both the streamwise and wall-normal velocities. Throughout the boundary layer, it is observed that there exists a diminishing trend caused by the dimple outside of the statistical uncertainty.

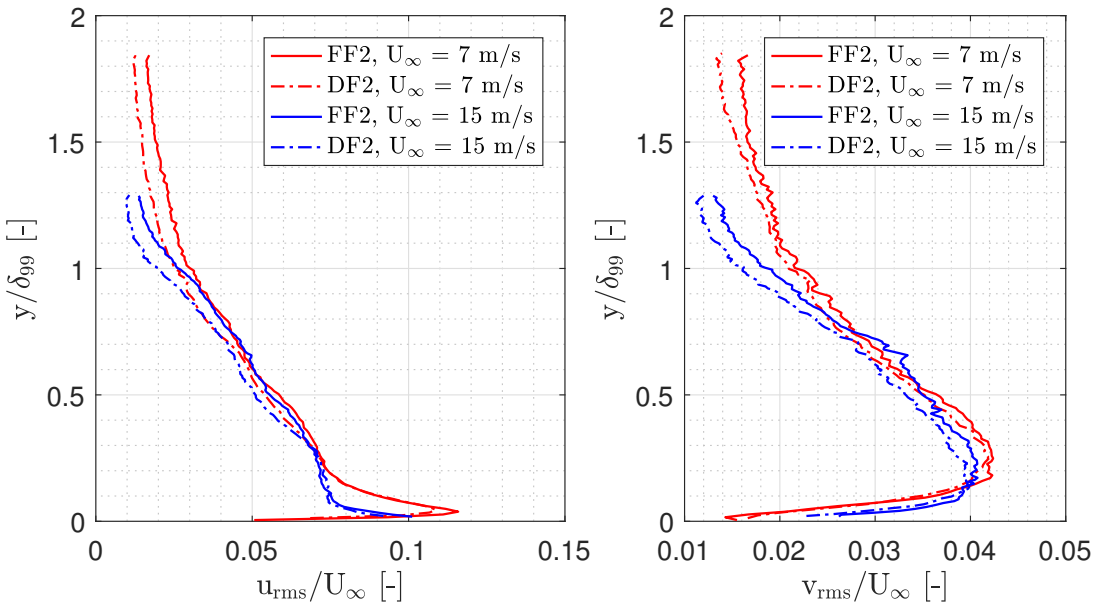

(A) u_{rms}. (B) v_{rms}.

FIGURE 4.39: Turbulent intensities for the SFPG case at x = 150 mm.

4.3.5 Strong adverse pressure gradient

Finally the boundary layer is quantified for the SAPG case. When an adverse pressure gradient is introduced to the boundary layer by means of a positive diffuser deflection $\varphi = 13°$ the flow velocity is expected to decrease. In an adverse pressure gradient the boundary layer starts to grow at a rate higher than for the ZPG case. The boundary layer thicknesses for the SAPG case computed by the aerodynamic boundary layer simulation discussed in Section 3.1.2 and tabulated in Table 4.7 are at lower values compared to the actual measured values.

The result of this is that the boundary layers in the upstream location are not captured in total for the SAPG case. It was found that for this configuration flow is sucked into the test section through the side gaps. In Table 4.8 the boundary layer characteristics of the SAPG case are shown, where the upstream values for the PIV measurements are missing due to the failure of capturing the entire boundary layer profile in the FOV. From Table 4.8 it is induced that the flow is indeed decelerating (accompanied by a positive pressure coefficient), and the shape factor starts to increase in downstream direction as is expected for an adverse pressure gradient.

TABLE 4.8: Boundary layer characteristics measured for the SAPG case.

Geometry [-]	**x** [mm]	$\mathbf{U_\infty}$ [m/s]	δ_{99} [mm]	δ^* [mm]	θ [mm]	**H** [-]	$\mathbf{U_e}$ [m/s]	$\mathbf{C_p}$ [-]
Flat (PIV)	520	15	41.0	9.6	6.21	1.55	13.1	0.23
Dimpled (PIV)	520	15	42.5	9.9	6.44	1.54	13.2	0.23
Flat (PIV)	520	30	49.3	12.4	7.87	1.57	26.4	0.23
Dimpled (PIV)	520	30	49.1	11.7	7.70	1.52	26.3	0.23
Flat (HWA)	520	15	43.6	10.1	6.5	1.56	13.1	0.24
Dimpled (HWA)	520	15	43.9	10.1	6.5	1.55	13.1	0.24
Flat (HWA)	520	30	40.9	9.6	6.2	1.54	26.4	0.23
Dimpled (HWA)	520	30	41.8	9.5	6.2	1.53	26.4	0.23

One particular inconsistency in Table 4.8 is the displacement thickness δ^* between the U_∞ = 30 m/s cases of both the HWA and PIV campaign. The value found for the PIV measurements is 10% higher than for the HWA campaign. To investigate this discrepancy further the mean velocity profiles are presented in Figure 4.40.

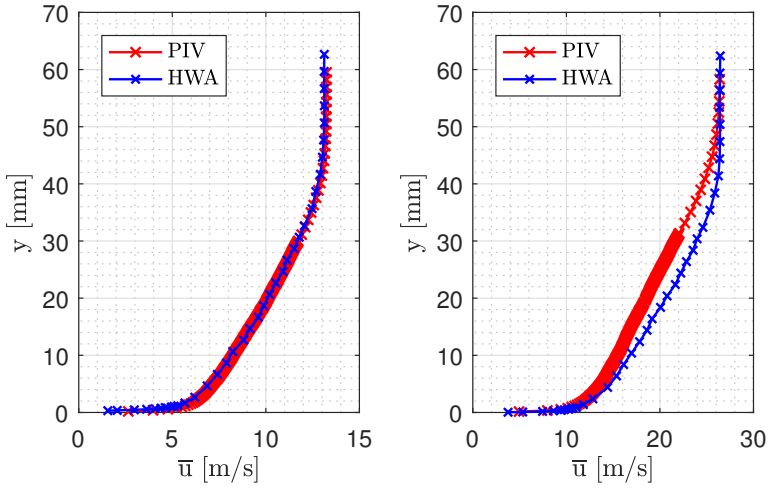

(A) U_∞ = 15 m/s. (B) U_∞ = 30 m/s.

FIGURE 4.40: Comparison of flat plate mean velocity profiles for the SAPG case.

It is found from Figure 4.40 that the mean velocity profiles of the U_∞ = 15 m/s case correspond closely, whereas there is a larger difference between the U_∞ = 30 m/s cases. The HWA profile shows a distinct fuller profile, although the freestream velocity is equal to one another. It is found that the PIV case was measured at an upstream velocity of U_∞ = 30.0023 m/s, while the HWA measurements where performed at an upstream velocity of

U_∞ = 30.0171 m/s: a minor difference. The PIV measurement at 30 m/s was also conducted directly after the the U_∞ = 15 m/s case, and thus changes to the set-up should be minor.

Skin-friction coefficient. As the flow starts to decelerate, it is observed that the wake region of the profile starts to increase and become larger compared to the ZPG case. In Figure 4.41 the curve-fitted boundary layer profiles are shown for the SAPG case. As the the wake region is larger for the SAPG case, the number of points used for the curve fit is smaller than for the ZPG case, increasing possible errors in the curve-fitting algorithm. Even though this is the case, generally good fits are found. For the upstream positions at x = 150 mm Figures 4.41a and 4.41c show that the boundary layer grows larger than the inspected field of view. As the curve-fitting procedure is dependent on the freestream velocity U_e a third curve-fitting property is added to the algorithm which is this freestream velocity. It is unwanted to perform a curve fit on three properties for the dimpled case. instead the freestream velocity is computed for the dimpled case by performing a curve-fit on the non-dimpled case, as such a curve fit only has two inputs which are C_f and U_e. As the upstream position at x = 150 mm is not far removed from the start of the test plate, it is assumed that the freestream velocity is not influenced by the dimples and equal to the freestream velocity for the flat plate case. The resulting freestream velocity is then inserted for the dimpled case. For the downstream location the freestream velocity U_e can however be determined by the merging of FOV 2 and FOV 3.

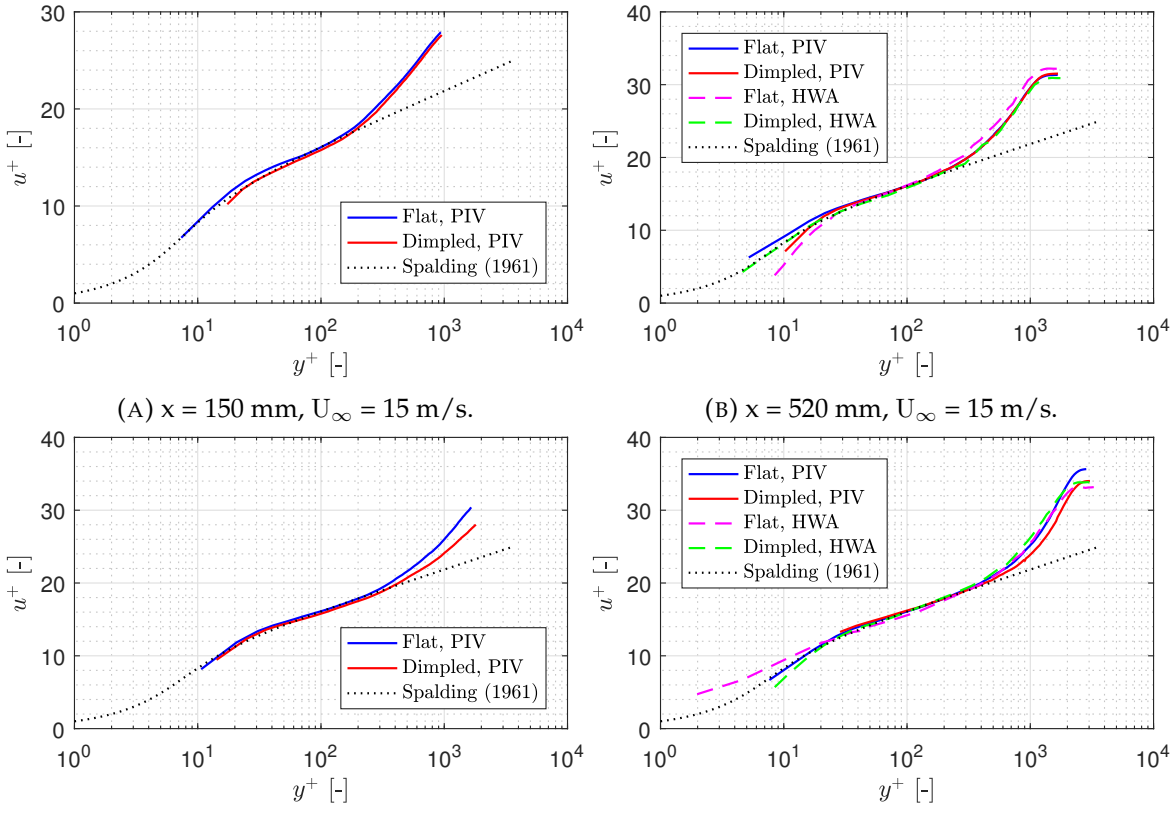

(A) x = 150 mm, U_∞ = 15 m/s.

(B) x = 520 mm, U_∞ = 15 m/s.

(C) x = 150 mm, U_∞ = 30 m/s.

(D) x = 520 mm, U_∞ = 30 m/s.

FIGURE 4.41: Boundary layer profiles in wall coordinates for the SAPG case.

The results of the curve-fitting procedure are then shown in Table 4.9 for the SAPG case. Skin-friction increases are found for the downstream locations in the HWA measurements. More profound drag increases are found in for the U_∞ = 30 m/s case in the downstream location. Drag reductions are indeed found for the U_∞ = 15 m/s case for the PIV measurements,

but it is accompanied by a negative shift of the logarithmic layer which should indicate a drag increase. As the number of fitting points is smallest for the 15 m/s case, this is the most likely cause together with the assumed freestream velocity derived from the fitting of the flat plate case. The results indicate that increasing the Reynolds number currently leads to a drag increase, where the highest drag increase is attained in the upstream location.

TABLE 4.9: Clauser fit of the boundary layer profiles non-dimensionalized in wall units for the SAPG case.

				HWA		PIV	
Geometry [-]	**x [mm]**	$\mathbf{U_\infty}$ $[\mathbf{m/s}]$	$\mathbf{Re_D}$ $[\mathbf{10^4}]$	$\mathbf{C_f}$ $[\mathbf{10^{-3}}]$	$\mathbf{\Delta B}$ $[-]$	$\mathbf{C_f}$ $[\mathbf{10^{-3}}]$	$\mathbf{\Delta B}$ $[-]$
Flat	150	15	1.99	-	-	2.65	0
Dimpled	150	15	1.99	-	-	2.64	-0.3
$\mathbf{\Delta}[\%]$	**-**	**-**	**-**	**-**	**-**	**-0.3**	**-**
Flat	520	15	1.99	2.03	-	2.08	0
Dimpled	520	15	1.99	2.09	0.00	2.05	0.0
$\mathbf{\Delta}[\%]$	**-**	**-**	**-**	**3.0**	**-**	**-1.7**	**-**
Flat	150	30	3.99	-	-	2.16	0
Dimpled	150	30	3.99	-	-	2.58	-0.4
$\mathbf{\Delta}[\%]$	**-**	**-**	**-**	**-**	**-**	**19.5**	**-**
Flat	520	30	3.99	1.68	-	1.58	0
Dimpled	520	30	3.99	1.75	0.00	1.73	0.0
$\mathbf{\Delta}[\%]$	**-**	**-**	**-**	**4.0**	**-**	**9.9**	**-**

Reynolds shear stress. For adverse pressure gradients it is reported in literature that the turbulent events move upwards from the wall. This general trend is indeed observed in the Reynolds shear stress profiles of the SAPG case. In Figure 4.42 it is found that the Reynolds shear stress profile resembles the ZPG case, but traversing further downstream the effect of the pressure gradient becomes visible. Whereas for the ZPG case the location of maximum Reynolds shear stress is location around $y/\delta_{99} \approx 0.2$, this position of maximum shear stress moves upward in Figure 4.42b and Figure 4.42d to $y/\delta_{99} \approx 0.35$. It is found that for U_∞ = 15 m/s a small change exists, but more profoundly for U_∞ = 30 m/s.

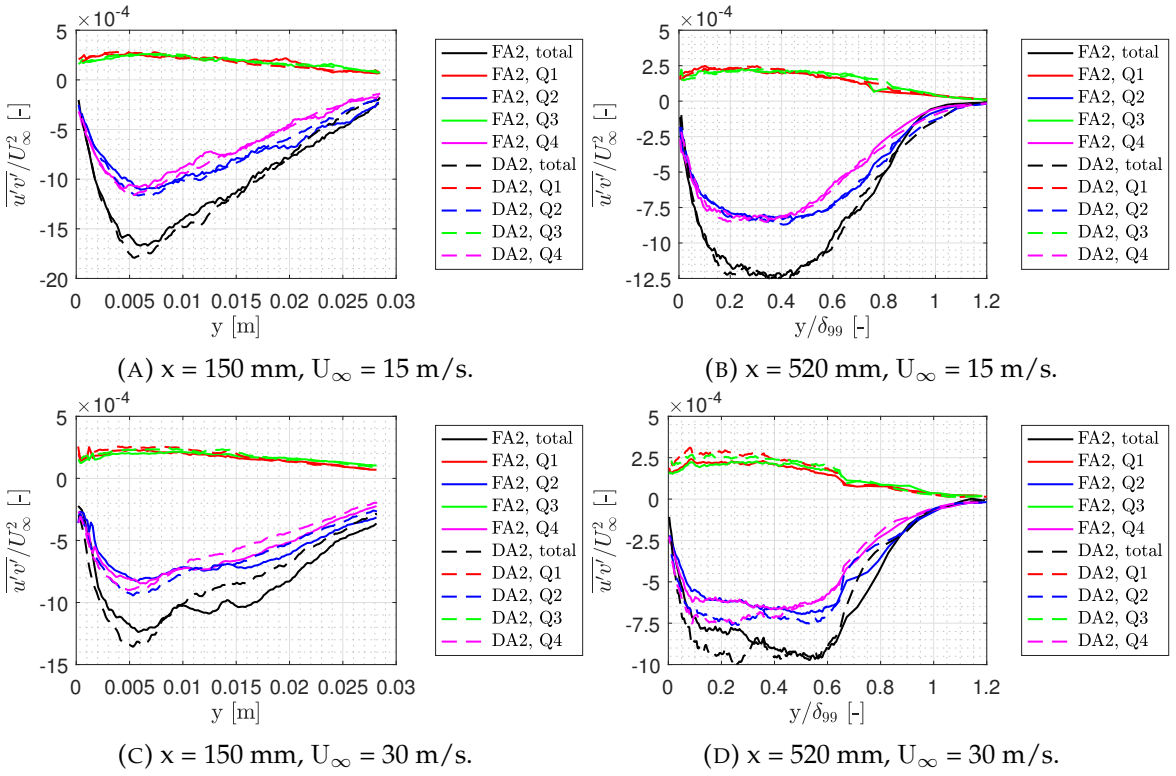

(A) x = 150 mm, U_∞ = 15 m/s.

(B) x = 520 mm, U_∞ = 15 m/s.

(C) x = 150 mm, U_∞ = 30 m/s.

(D) x = 520 mm, U_∞ = 30 m/s.

FIGURE 4.42: Reynolds shear stress profiles and quadrant contributions for the SAPG case.

Integrating the Reynolds shear stress profiles then leads to the values found in Table 4.10. Once again it is found that the noise introduced due to an unconverged Reynolds shear stress influences the integration procedure. It is found as a general trend from Figure 4.42 that the Reynolds shear stress has a larger peak value for the dimpled plate than for the flat plate, but noise in the profile does not allow for accurate numerical comparison.

TABLE 4.10: Skin-friction contributions of the Reynolds shear stress for the SAPG case.

Geometry [-]	**x [mm]**	$\mathbf{U_\infty}$ [m/s]	$\mathbf{Re_D}$ [10^4]	$\mathbf{C_{f,turb}}$ [10^{-3}]	$\mathbf{C_{f,Q1}}$ [10^{-3}]	$\mathbf{C_{f,Q2}}$ [10^{-3}]	$\mathbf{C_{f,Q3}}$ [10^{-3}]	$\mathbf{C_{f,Q4}}$ [10^{-3}]
Flat	150	15	1.99	2.34	-0.43	1.63	-0.40	1.54
Dimpled	150	15	1.99	2.44	-0.42	1.69	-0.42	1.60
Δ [%]	-	-	-	4.3	-1.4	3.2	3.9	3.8
Flat	520	15	1.99	1.63	-0.32	1.16	-0.33	1.11
Dimpled	520	15	1.99	1.66	-0.33	1.19	-0.33	1.13
Δ [%]	-	-	-	2.2	4.7	2.3	-0.1	2.1
Flat	150	30	3.99	1.90	-0.37	1.32	-0.37	1.32
Dimpled	150	30	3.99	1.88	-0.41	1.39	-0.40	1.30
Δ [%]	-	-	-	-0.7	10.0	5.3	8.4	-1.2
Flat	520	30	3.99	1.39	-0.34	1.06	-0.35	1.02
Dimpled	520	30	3.99	1.48	-0.41	1.17	-0.40	1.12
Δ [%]	-	-	-	6.3	21.3	10.2	13.4	9.7

In Figure 4.43 the quadrant probability difference is presented for the downstream location of the SAPG case for U_∞ = 15 m/s. Contrary to the ZPG and SFPG case, the events are

increased around the u'-axis and reduced further away from it, instead of vice-versa. The differences are however small, within half of a percent difference. Especially the Q2 and Q3 events are amplified in the near-wall region for this case. These events lead to an increase and decrease of Reynolds stress respectively, and thus it is expected that the combined effect of the increases is net zero.

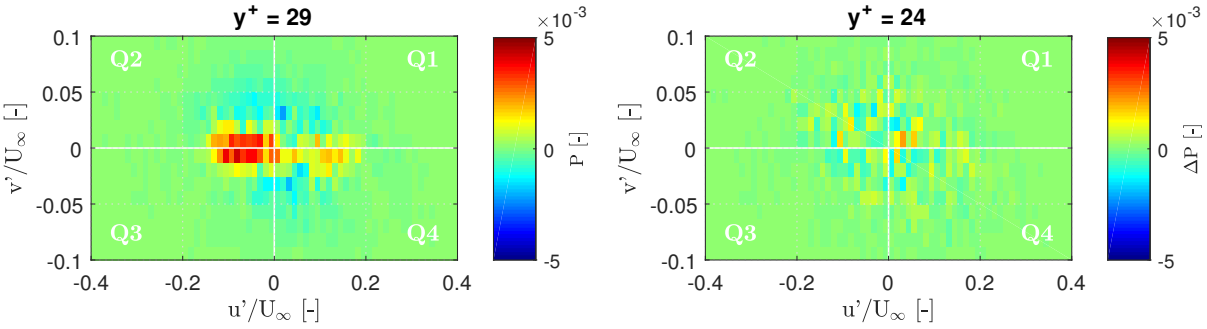

(A) Flat minus dimpled plate.

(B) Flat minus flat plate.

FIGURE 4.43: Quadrant probability difference for the SAPG case, downstream location at U_∞ = 15 m/s.

Turbulence intensity. When a strong adverse pressure gradient is applied the occurrence of a second u_{rms} peak is reported by literature. When looking at Figure 4.44 it is indeed observed that a second peak is present that is located higher than the near wall peak, and of higher magnitude. This behavior is represented in the Reynolds shear stress behavior as well, where it is observed that the traditional peak at y/δ_{99} = 0.2 for the ZPG case is moved upwards in Figure 4.42b and Figure 4.42d.

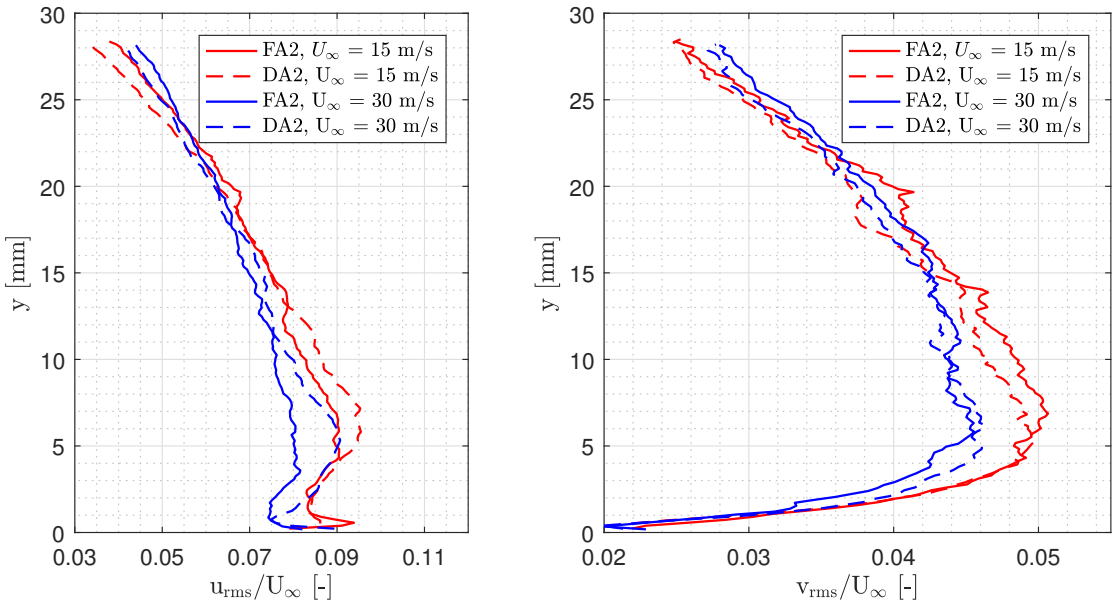

(A) u_{rms}.

(B) v_{rms}.

FIGURE 4.44: Turbulent intensities for the SAPG case at x = 150 mm.

When comparing the different values it is observed that for the streamwise velocity turbulence intensity the dimpled case shows overall higher values throughout the boundary layer for the streamwise turbulence intensities. For the wall-normal turbulence intensities a

smaller peak value is observed, but is currently within statistical uncertainty. The streamwise turbulent intensity is observed in the HWA results, where a second peak is also observed. The differences in turbulence intensity between the dimple and the flat plate are however minor in the downstream location.

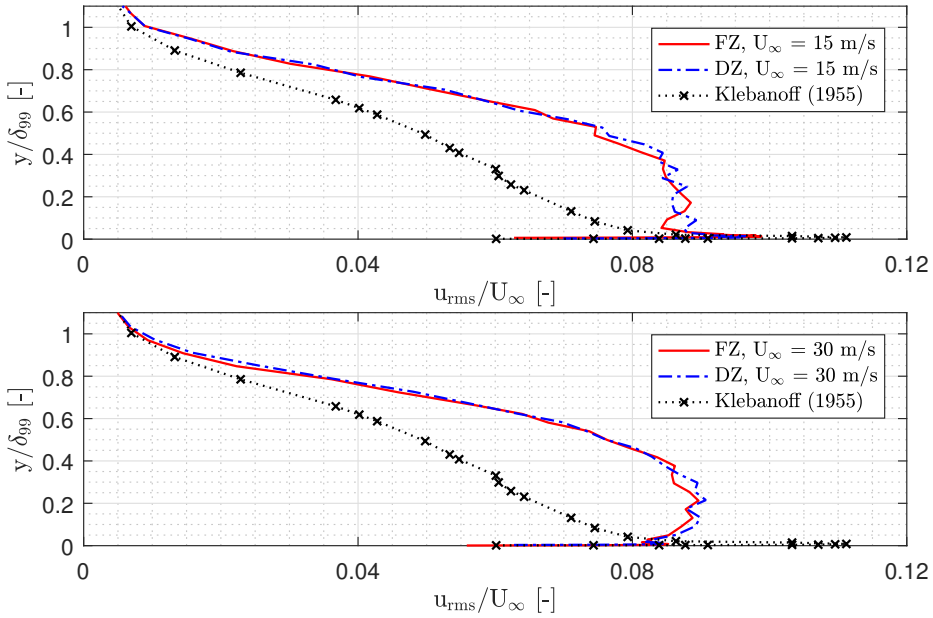

FIGURE 4.45: HWA streamwise turbulent intensities for the SAPG case in the downstream position at x = 520 mm.

Chapter 5

Conclusion

In this chapter the results from the direct drag quantification and the boundary layer flow quantification are used to synthesize a conclusion on the current research and recommendations for future research.

5.1 Conclusions

Before reaching the concluding remarks, the research questions are restated here:

1. *How is the skin-friction reduction in a dimpled surface affected by the pressure gradient and the Reynolds number?*
2. *Does a dimpled surface cause a skin friction reduction by a change in the turbulent properties?*

After performing a DFM campaign, PIV campaign and HWA campaign these research questions will be answered below for the different considered pressure gradient cases in this experimental investigation. First some general conclusions are noted for the experimental campaigns. It was found using tufts that the existence of a required gap for the drag balance allowed flow to enter and leave the test section during the experimental runs, possibly introducing unwanted flow properties. These were the most prevalent for the larger Reynolds numbers, and least prevalent for the ZPG case as a whole. The boundary layer profiles that were obtained were measured at two streamwise locations at the spanwise center of the test plate. As a result, differences in skin-friction measured at these locations do not imply that they are also found at other stations on the test plate. It must however be noted that the measurement location was at the location of the highest spanwise induced velocity of the dimple, and thus this is the as of yet best probable location to measure a drag difference if the spanwise shear theory is valid.

Zero pressure gradient. The ZPG results for the direct drag quantification are extracted from the total set of results as a good repeatability was determined for the ZPG case. For this case deviations below 0.5% were determined, indicating that the result for the ZPG case for the dimpled case is the strongest result of the DFM campaign. This data set is extracted and placed within the existing body of knowledge obtained at DUT, as previous experiments at DUT have been performed for the same wind-tunnel geometry, pressure gradient, Reynolds number range and test plate geometry. The main difference between previous measurements at DUT is the use of a new drag balance and a different wind-tunnel. For the ZPG case a drag reduction was found by using direct force measurements, and a trend of increasing drag reduction with increasing Reynolds number was observer analogous to the results of Van Nesselrooij (2015). The magnitude of the drag reduction is however lower: 0.8% for the current study against 4% for the study performed by Van Nesselrooij (2015). The results of the ZPG total drag quantification are shown in Figure 5.1 together with previous results at DUT.

Within the boundary layer a minimal change was found in the turbulent properties, with negligible differences for the turbulence intensity and even a slight increase of the Reynolds shear stress, for both upstream and downstream locations for the two considered upstream velocities. The skin-friction coefficients found from both measurement techniques yielded small differences in magnitude, and even negligible for the HWA results. Although these difference were found, they were both positive and negative, and no clear trend of the skin-friction reduction exists as a function of upstream Reynolds number $\mathrm{Re_D}$. This is in contrast with the results observed from the total drag quantification, in which the total drag force of the test plate is captured and a consistent trend with $\mathrm{Re_D}$ was observed. It was observed that a drag reduction of 0.8% is obtained for the maximum considered Reynolds number for the ZPG case in the total drag quantification. This configuration was also thoroughly validated with the repeatability measurements in which set-up bias was quantified. The obtained drag reductions by the dimpled surface in the ZPG configuration lies within the uncertainty margins determined from the two repeatability runs performed beforehand.

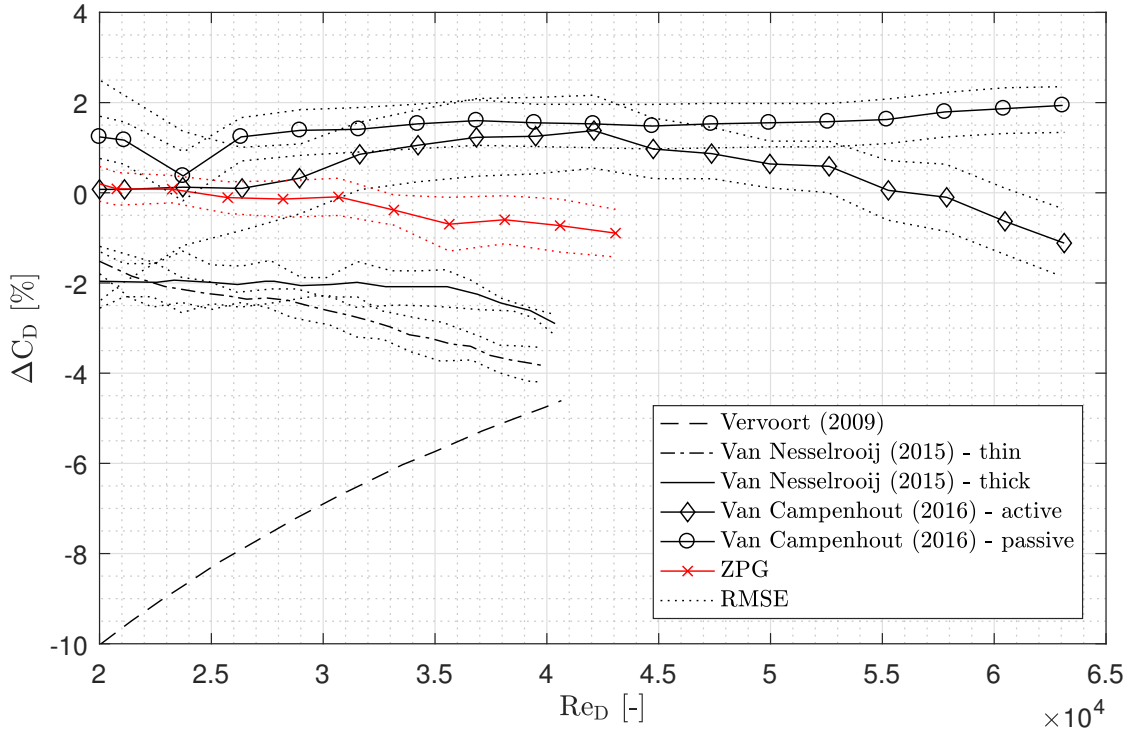

FIGURE 5.1: Total drag quantification results shown between previous results at DUT.

Favorable pressure gradient. The favorable pressure gradient case was investigated for both a strong case (SFPG, φ = -13°) and a mild case (MFPG, φ = -6.5°) for the total drag quantification. Both cases showed a mean drag reduction, as is shown in Figure 5.2. For the MFPG case the drag difference with the dimpled plate varied between -2% and -3%, remaining fairly constant with increasing Reynolds number. For the SFPG case the drag difference varied between 0% and -2% for the dimpled plate and just as the MFPG case it stayed fairly constant with increasing Reynolds number. The SFPG case showed a drag increase for one individual measurement run and thus the mean drag reduction is plagued by a deviation around the mean that traverses into a drag increase. This deviation introduces uncertainty for the actual occurrence of a drag reduction. The results of the direct drag quantifications are however strengthened by the results obtained from the boundary layer profile quantification, which was performed for the SFPG case. For all considered upstream velocities, and

for both the upstream and downstream location, a reduced skin-friction coefficient is found accompanied by an upwards shift of the logarithmic layer ΔB in the order of 1, comparable to the shifts found for drag-reducing compliant coatings by Choi et al. (1997). Looking at other turbulent properties like the Reynolds shear stress, the turbulence intensity it is indeed observed that they decrease in the SFPG case. An increase in the laminarization parameter K is found for all upstream velocities and locations, with an exception for the downstream location at U_∞ = 15 m/s, where the relaminarization parameter K decreases. As the change is not observed within the ZPG case, it seems the dimple has a beneficial effect on the laminarization effort of the SFPG, allowing the boundary layer to laminarize faster.

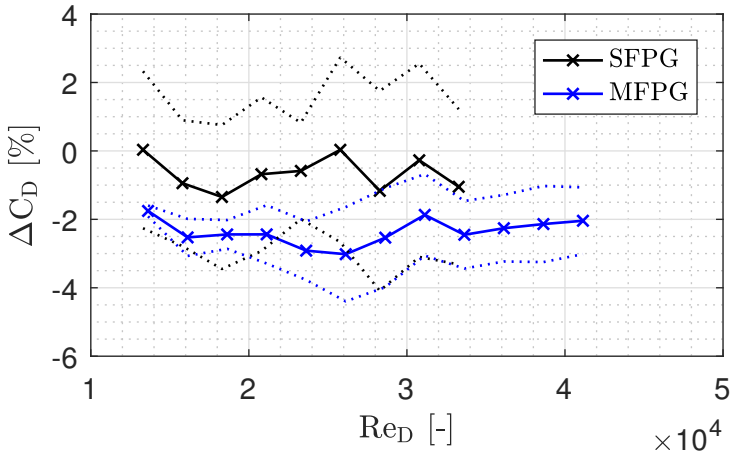

FIGURE 5.2: Total drag quantification results for the FPG cases.

Adverse pressure gradient. The adverse pressure gradient case was investigated for both a strong case (SAPG, $\varphi = 10°$) and a mild case (MAPG, $\varphi = 5°$) for the total drag quantification. The investigation of the adverse pressure gradient was subjected to several problems. First of all it was observed during the experiment that flow was sucked in from the ambient at the set-up/test plate interface. Looking at the force signal, it was furthermore observed that when the Reynolds number increased, a dent starts to exist in the force signal, indicating a decreasing force when the velocity is increased. This change persisted when performing the run backwards, and using tufts the flow field was qualitatively investigated on all walls in the experimental set-up. No separation was observed at any wall. The cause of the dent in the force signal as of now still remains unknown. The dent seems to have an effect on the drag reduction caused by a dimple. The results for both adverse pressure gradients are given in Figure 5.3. For the SAPG case a relatively large reduction of 10% was found, which traversed into a drag increase of 10% with increasing Re_D, with a relatively large deviation around the mean. For the MAPG case a smaller deviation around the man is found, and a drag reduction was reported for the larger part with the exception of the Reynolds regime affected by the dent in the force signal.

For the PIV and HWA measurements the correlation algorithm had less measurement points to fit to the rewritten law of the wall, impeding proper comparison of the skin-friction coefficients between the flat surface and the dimpled surface. The turbulent properties were also investigated, and they revealed an increase in turbulence intensity throughout the entire boundary layer profile. The Reynolds stress profiles were not converged in such a matter that precise comparison can be made. From the Reynolds shear stress profiles that were obtained, it was however found that for the dimpled surface the Reynolds shear stress increases at the peak location. As Reynolds stresses close to the surface are weighted more

heavily in the skin-friction coefficient, it is expected that the skin-friction is in fact higher at this location.

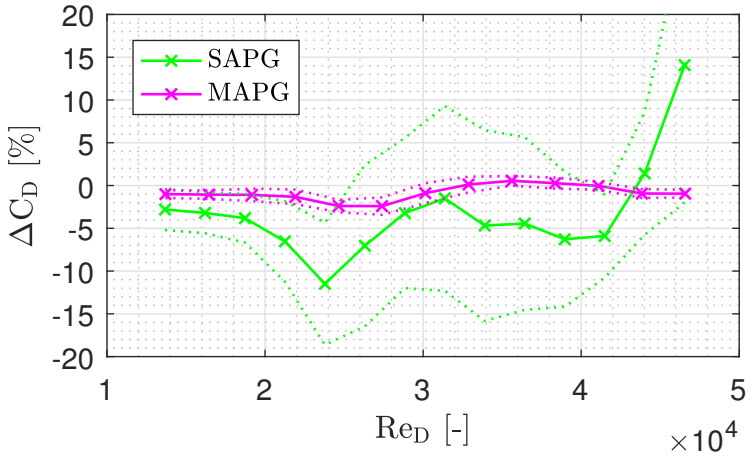

FIGURE 5.3: Total drag quantification results for the APG cases.

5.2 Recommendations

As is commonplace for experimental investigations, the new insights into the experiment can be used to formulate recommendations for future research. They are briefly noted in this section.

Experimental set-up optimization. During the experiments it was found that inherent properties of the drag balance inhibit uniform flow features of the drag properties, especially for the pressure gradient cases. The gaps at the sides of the drag balance, which are indispensable for the drag balance, introduce flow into the set-up for the adverse pressure gradient cases and allow flow to leave the set-up. To improve the set-up it is wanted to reduce the width of the side gaps, which could be attained by the application of a small film covering them. For the drag balance it was also required to have a low flexure stiffness to allow the bulk of the force to be applied at the force sensor. This inherent property also leads to structural resonance since the natural frequency of the system is then also relatively low. In order to reduce the effect of vibrations the test plate can be connected to an oil bath by means of an extra rod. Such an extra measure would introduce dampening into the system, reducing the spread of the force signal and increasing the statistical significance of the signal.

Momentum deficit analysis. As a fluid moves over a surface it exchanges momentum to the surface which is manifested in the drag force of the surface. Using the momentum deficit of the boundary layer the effective drag coefficient of the test plate can be computed. The momentum deficit can be investigated over a spanwise distance relative to the streamwise locations considered in this study. This can be done either by putting a PIV laser plane sheet over the exit of the test section, perpendicular to the mean flow, as well as at the start. The difference in momentum can then be manipulated into a drag force. A fine pressure rake is another possibility, which can be fitted with a traversing wheel to allow a relatively large spatial resolution. An advantage of a momentum deficit method is that no side gaps are required, and the test section can be completely closed off from the outside world. When testing at different pressure gradients this then also circumvent the exchange of flow with the ambient through the gaps.

Skin-friction measurement. The skin-friction coefficient of was determined by taking a nonlinear least-squares fit of the logarithmic layer, in which both C_f and ΔB were determined simultaneously. To determine the skin-friction coefficient more accurately two possible options could be attempted. The skin-friction could be determined by measuring the pressure loss over two locations spaced closely together (as is common in channel flows drag reduction studies), and measuring the boundary layer profile between those locations to determine the actual wall intercept change. Another more direct option is by measuring the wall-normal velocity gradient very close the wall with either a hot-wire or μ-PTV, as the skin-friction is a function of the velocity gradient at the wall.

Drag reduction in a favorable pressure gradient. If the dimple has a beneficial effect on the relaminarization parameter K, it is of interest if this drag reduction in maintained for increased Reynolds number. The relaminarization parameter K is inversely correlated to the upstream velocity, indicating that the critical value K = 3.5×10^{-6} becomes harder to attain when the freestream velocity increases. It is expected that possible effects of the dimple are annulled when the Reynolds number is further increased.

Direct numerical simulation. As also posed by previous authors, there could also be a benefit into investigating the turbulent structures around a dimple by means of a DNS study. Yakeno et al. (2014) used DNS to investigate the effect of an oscillating wall on the turbulent structures that exist within the near-wall region, and such an analysis can also give insight into possible manipulation of the flow field in the near-wall region by a dimpled surface. The possible downside of a DNS study is that it is restricted to low Reynolds numbers, whereas the perceived drag reductions are obtained at relatively higher Reynolds numbers. It is posed that that at low Reynolds numbers the effect of a skin-friction reduction is annulled by the advent of a pressure force. A DNS study could however still yield valuable results into the actual *presence* of turbulence manipulation by the dimpled surface, although at lower Reynolds numbers.

These recommendations can then lead to the further advancement of the knowledge on drag reductions by dimpled surfaces in turbulent boundary layers.

Bibliography

R. J. Adrian, C. D. Meinhart, and C. D. Tomkins. Vortex organization in the outer region of the turbulent boundary layer. *Journal of Fluid Mechanics*, 422:1–54, 2000. ISSN 0022-1120. doi: 10.1017/S0022112000001580.

J. B. Zhao, Y. T. Chew, and B. Khoo. Experimental studies on hydrodynamic resistance and flow pattern of a narrow flow channel with dimples on the wall. 260, 01 2004.

H. P. Bakewell and J. L. Lumley. Viscous sublayer and adjacent wall region in turbulent pipe flow. *The Physics of Fluids*, 10(9):1880–1889, 1967. ISSN 0031-9171. doi: 10.1063/1.1762382.

L. H. Benedict and R. D. Gould. Towards better uncertainty estimates for turbulence statistics. *Experiments in Fluids*, 22(2):129–136, Dec 1996. ISSN 1432-1114. doi: 10.1007/s003480050030.

N. K. Burgess and P. M. Ligrani. Effects of dimple depth on nusselt numbers and friction factors for internal cooling in a channel. (41685):989–998, 2004. doi: 10.1115/GT2004-54232.

H. Choi, P. Moin, and J. Kim. *Direct Numerical Simulation of Turbulent Flow Over Riblets*, volume 255. 1993. doi: 10.1017/S0022112093002575.

H. Choi, P. Moin, and J. Kim. Active turbulence control for drag reduction in wall-bounded flows. *J. Fluid Mech.*, 262:75–110, 1994.

K. S. Choi. Near-wall structure of a turbulent boundary layer with riblets. *J. Fluid Mech*, 208: 417–458, 1989.

K. S. Choi and B. R. Clayton. The mechanism of turbulent drag reduction with wall oscillation. *International Journal of Heat and Fluid Flow*, 22(1):1–9, 2001. ISSN 0142-727X. doi: 10.1016/S0142-727x(00)00070-9.

K. S. Choi, X. Yang, B. Clayton, E. Glover, M. Atlar, B. Semenov, and V. Kulik. Turbulent drag reduction using compliant surfaces. In *Proceedings of the Royal Society of London A: Mathematical, Physical and Engineering Sciences*, volume 453, pages 2229–2240. The Royal Society, 1997. ISBN 1364-5021.

K.-S. Choi, J.-R. Debisschop, and B. R. Clayton. Turbulent boundary-layer control by means of spanwise-wall oscillation. *AIAA Journal*, 36(7):1157–1163, 1998. ISSN 0001-1452. doi: 10.2514/2.526.

E. R. Corino and R. S. Brodkey. A visual investigation of the wall region in turbulent flow. *Journal of Fluid Mechanics*, 37(1):1–30, 1969. ISSN 0022-1120. doi: 10.1017/S0022112069000395.

B. Dean and B. Bhushan. Shark-skin surfaces for fluid-drag reduction in turbulent flow: a review. *Philosophical Transactions of the Royal Society A: Mathematical, Physical and Engineering Sciences*, 368(1929):4775, 2010.

J. R. Debisschop and F. T. M. Nieuwstadt. Turbulent boundary layer in an adverse pressure gradient - effectiveness of riblets. *AIAA Journal*, 34(5):932–937, 1996. doi: 10.2514/3.13170.

D. J. Dennis. Coherent structures in wall-bounded turbulence. *Anais da Academia Brasileira de Ciências*, 87:1161–1193, 2015. ISSN 0001-3765.

A. Dróżdż and V. Uruba. Comparison of piv and hot-wire statistics of turbulent boundary layer. *Journal of Physics: Conference Series*, 530, 2014.

A. Drozdz and W. Elsner. Detection of coherent strucutes in a turbulent boundary layer with zero, favourable and adverse pressure gradients. *Journal of Physics: Conference Series*, 318 (6), 2011.

A. Drozdz, W. Elsner, and S. Drobniak. Scaling of streamwise reynolds stress for turbulent boundary layers with pressure gradient. *European Journal of Mechanics B/Fluids*, 49:137–145, 2015.

J. H. Duncan. The response of an incompressible, viscoelastic coating to pressure fluctuations in a turbulent boundary layer. *Journal of Fluid Mechanics*, 171:339–363, 1986. ISSN 1469-7645.

G. Eitel-Amor, R. Örlü, P. Schlatter, and O. Flores. Hairpin vortices in turbulent boundary layers. *Physics of Fluids*, 27(2):025108, 2015. doi: 10.1063/1.4907783.

G. Elsinga, D. J. Kuik, B. van Oudheusden, and F. Scarano. Investigation of the three-dimensional coherent structures in a turbulent boundary layer with tomographic-piv. In *45th AIAA Aerospace Sciences Meeting and Exhibit*, 2007.

M. C. Fischer and R. L. Ash. A general review of concepts for reducing skin friction, including recommendations for future studies. Technical report, NASA Langley Research Center, 1974.

K. Fukagata, K. Iwamoto, and N. Kasagi. Contribution of reynolds stress distribution to the skin friction in wall-bounded flows. *Physics of Fluids*, 14, 2002.

M. Gad-el Hak. *Flow Control: Passive, Active, and Reactive Flow Management*. Cambridge University Press, 2006. ISBN 9780521036719.

D. Gatti. Reynolds-number dependence of turbulent skin-friction drag reduction induced by spanwise forcing. *J. Fluid Mech*, 802:553–582, 2016.

S. Ghebali, S. I. Chernyshenko, and M. A. Leschziner. Turbulent skin-friction reduction by wavy surfaces. *ArXiv e-prints*, 2017.

A. M. Hamed, A. Kamdar, L. Castillo, and L. P. Chamorro. Turbulent boundary layer over 2d and 3d large-scale wavy walls. *Physics of Fluids*, 27:106601, 2015.

M. Head. Entrainment in the turbulent boundary layer. *ARC*, 1960.

M. R. Head and P. Bandyopadhyay. New aspects of turbulent boundary-layer structure. *Journal of Fluid Mechanics*, 107:297–338, 1981. ISSN 0022-1120. doi: 10.1017/S0022112081001791.

International Air Transport Association. Annual Review 2016. Report, 2016.

S. A. Isaev, A. I. Leontiev, G. I. Kiknadze, N. A. Kudryavtsev, and I. A. Gachechiladze. Comparative analysis of the vortex heat exchange in turbulent flows around a spherical hole and a two-dimensional trench on a plane wall. *Journal of Engineering Physics and Thermophysics*, 78(4):749–761, 2005. ISSN 1062-0125. doi: 10.1007/s10891-005-0123-5.

F. E. Jørgensen. *How to measure turbulence with hot-wire anemometers*. Dantec Dynamics, 2002.

W. Jung, N. Mangiavacchi, and R. Akhavan. Suppression of turbulence in wall-bounded flows by high-frequency spanwise oscillations. *Physics of Fluids A: Fluid Dynamics (1989-1993)*, 4(8):1605–1607, 1992. ISSN 0899-8213.

N. Kasagi and K. Fukagata. *The FIK Identity and Its Implication for Turbulent Skin Friction Control*, book section 10, pages 297–324. World Scientific, 2006.

J. M. Kendall. The turbulent boundary layer over a wall with progressive surface waves. *Journal of Fluid Mechanics*, 41(02):259–281, 1970. ISSN 1469-7645.

G. I. Kiknadze, Y. K. Krasnov, and Y. V. Chushkin. Investigation of the enhancement of heat transfer due to self-organization of ordered dynamic twisted heat-carrier structures on a heat-transfer surface. Report, I. V. Kurchatov Institute of Atomic Energy, 1984.

G. I. Kiknadze, I. A. Gachechiladze, and T. T. Barnaveli Jr. The mechanisms of the phenomenon of tornado-like jets self-organization in the flow along the dimples on the initially flat surface. In *ASME International Mechanical Engineering Congress and Exposition, Proceedings (IMECE)*, volume 7, pages 3017–3026, 2012a.

G. I. Kiknadze, I. A. Gachechiladze, and T. T. Barnaveli Jr. The mechanisms of the phenomenon of tornado-like jets self-organization in the flow along the dimples on the initially flat surface. In *ASME International Mechanical Engineering Congress and Exposition, Proceedings (IMECE)*, volume 7, pages 3017–3026, 2012b.

J. H. Kim and J. H. Lee. Skin-friction drag reduction in turbulent channel flow based on streamwise shear control. *International Journal of Heat and Fluid Flow*, 63:28–43, 2017. ISSN 0142-727X. doi: http://dx.doi.org/10.1016/j.ijheatfluidflow.2016.12.001. URL `http://www.sciencedirect.com/science/article/pii/S0142727X16302016`.

P. Klebanoff. Characters of turbulence in boundary layer with zero pressure gradient. Report, NACA, 1955.

S. J. Kline, W. C. Reynolds, F. A. Schraub, and P. W. Runstadler. The structure of turbulent boundary layers. *J. Fluid Mech.*, 30:741–773, 1967.

S. Klumpp, T. Guldner, M. Meinke, and W. Schröder. *Riblets in a turbulent adverse-pressure gradient boundary layer*. Fluid Dynamics and Co-located Conferences. American Institute of Aeronautics and Astronautics, 2010. doi: 10.2514/6.2010-4706.

M. O. Kramer. Boundary layer stabiliztion by distributed damping. *Journal of the American Society for Naval Engineers*, 72:25–33, 1960. doi: 10.1111/j.1559-3584.1960.tb02356.x.

P.-A. Krogstad and P. E. Skare. Influence of a strong adverse pressure gradient on the turbulent structure in a boundary layer. *Physics of Fluids*, 7, 1995.

D. J. Kuik. *Tomographic PIV investigation of a turbulent boundary layer*. Thesis, Delft University of Technology, 2007.

V. M. Kulik, I. S. Poguda, and B. N. Semenov. *Experimental investigation of one-layer viscoelastic coatings action on turbulent friction and wall pressure pulsations*, pages 263–289. Springer Netherlands, Dordrecht, 1991. doi: 10.1007/978-94-011-3526-9_14.

Y. A. Lashkov and N. V. Samoilova. On the viscous drag of a plate with spherical recesses. *Fluid Dynamics*, 37(2):231–236, 2002. ISSN 0015-4628. doi: 10.1023/A:1015806332333.

J.-H. Lee and H. J. Sung. Structures in turbulent boundary layers subjected to adverse pressure gradients. *J. Fluid Mech.*, 639:101–131, 2009.

A. Leontiev, N. Kiselev, Y. Vinogradov, M. Strongin, A. Zditovets, and S. Burtsev. Experimental investigation of heat transfer and drag on surfaces coated with dimples of different shape. *International Journal of Thermal Sciences*, 118(Supplement C):152 – 167, 2017. ISSN 1290-0729. doi: https://doi.org/10.1016/j.ijthermalsci.2017.04.027. URL `http://www.sciencedirect.com/science/article/pii/S1290072916312911`.

H. Lienhart, M. Breuer, and C. Köksoy. Drag reduction by dimples? — a complementary experimental/numerical investigation. *International Journal of Heat and Fluid Flow*, 29(3): 783–791, 2008. ISSN 0142727X. doi: 10.1016/j.ijheatfluidflow.2008.02.001.

H. Ludwieg and W. Tillmann. Untersuchungen über die wandschubspannung in turbulenten reibungsschichten. *ZAMM - Journal of Applied Mathematics and Mechanics / Zeitschrift für Angewandte Mathematik und Mechanik*, 29(1-2):15–16, 1949. ISSN 1521-4001. doi: 10.1002/zamm.19490290112.

Y. Maciel, M. P. Simens, and A. G. Gungor. Coherent structures in a non-equilibrium large-velocity defect turbulent boundary layer. *Flow, Turbulence and Combustion*, 98:1–20, 2017.

F. Mehdi, T. G. Johansson, C. White, and J. W. Naughton. On determining wall shear stress in spatially developing two-dimensional wall-bounded flows. *Exp. Fluids*, 55, 2014.

H. Mitsudharmadi, C. M. J. Tay, and H. M. Tsai. Effect of rounded edged dimple arrays on the boundary layer development. *Journal of Visualization*, 12(1):17–25, Mar 2009. ISSN 1875-8975. doi: 10.1007/BF03181939. URL `https://doi.org/10.1007/BF03181939`.

R. Mukund, P. R. Viswanath, R. Narasimha, A. Prabhu, and J. D. Crouch. Relaminarization in highly favourable pressure gradients on a convex surface. *J. Fluid Mech.*, 566:97–115, 2006.

R. Narasimha and K. R. Sreenivasan. Relaminarization of fluid flows. *Advances in Applied Mechanics*, 19:222–309, 1973.

F. T. M. Nieuwstadt, W. Wolthers, H. Leijdens, K. Krishna Prasad, and A. Schwarz-van Manen. The reduction of skin friction by riblets under the influence of an adverse pressure gradient. *Experiments in Fluids*, 15(1):17–26, 1993. ISSN 1432-1114. doi: 10.1007/BF00195591.

M. Perlin, D. R. Dowling, and S. L. Ceccio. Freeman scholar review: Passive and active skin-friction drag reduction in turbulent boundary layers. *Journal of Fluids Engineering*, 138(9), 2016. ISSN 0098-2202. doi: 10.1115/1.4033295.

S. Pope. *Turbulent Flows*. Cambridge University Press, 2000. ISBN 9780521598866.

M. Raffel, C. Willert, and J. Kompenhans. *Particle Image Velocimetry: A Practical Guide*. Engineering online library. Springer Berlin Heidelberg, 1998. ISBN 9783540636830.

D. Roggenkamp, W. Jessen, W. Li, and M. Klaas. Experimental investigation of turbulent boundary layers of transversal moving surfaces. *CEAS Aeronaut J*, 6:471–484, 2015.

M. Sasamori, H. Mamori, K. Iwamoto, and A. Murata. Experimental study on drag-reduction effect due to sinusoidal riblets in turbulent channel flow. *Experiments in Fluids*, 55(10):1828, 2014. ISSN 1432-1114. doi: 10.1007/s00348-014-1828.

F. Scarano. Experimental aerodynmaics, February 2013. AE4180 course reader.

P. R. Spalart and J. D. McLean. Drag reduction: enticing turbulence, and then an industry. *Philos Trans A Math Phys Eng Sci*, 369(1940):1556–69, 2011. ISSN 1364-503X (Print) 1364-503X (Linking). doi: 10.1098/rsta.2010.0369.

D. B. Spalding. A single formula for the "law of the wall". *Journal of Applied Mechanics*, 28 (3):455–458, 1961. ISSN 0021-8936. doi: 10.1115/1.3641728.

K. R. Sreenivasan. Laminarescent, relaminarizing and retransitional flows. *Acta Mechanica*, 44(1):1–48, 1981.

A. Starke, R. Henkes, and M. Tummers. Effects of curvature and pressure gradient on a turbulent near wake. *Experimental Thermal and Fluid Science*, 19:49–56, 1999.

J. Szodruch. *Viscous drag reduction on transport aircraft*. Aerospace Sciences Meetings. American Institute of Aeronautics and Astronautics, 1991. doi: doi:10.2514/6.1991-68510.2514/6.1991-685. URL `https://doi.org/10.2514/6.1991-685`.

C. M. Tay. Determining the effect of dimples on drag in a turbulent channel flow. In *49th AIAA Aerospace Sciences Meeting*. AIAA, 2011. doi: 10.2514/6.2011-682.

C. M. Tay, Y. T. Chew, B. C. Khoo, and J. B. Zhao. Development of flow structures over dimples. *Experimental Thermal and Fluid Science*, 52:278–287, 2014. ISSN 08941777. doi: 10.1016/j.expthermflusci.2013.10.001.

C. M. Tay, B. C. Khoo, and Y. T. Chew. Mechanics of drag reduction by shallow dimples in channel flow. *Physics of Fluids (1994-present)*, 27(3):035109, 2015. ISSN 1070-6631.

V. I. Terekhov, S. V. Kalinina, and Y. M. Mshvidobadze. Pressure field and resistance of a single cavity with sharp and rounded edges. *Journal of Applied Mechanics and Technical Physics*, 34(3):331–338, 1993. ISSN 0021-8944. doi: 10.1007/BF00864784.

T. Theodorsen. Mechanism of turbulence. *Proc. Second Midwestern Conf. on Fluid Mechanics*, 1951.

O. W. G. Van Campenhout. *Going against the flow, an experimental investigation into the flow mechanics of dimpled surfaces in turbulent boundary layer*. Thesis, Delft University of Technology, 2016.

O. W. G. Van Campenhout, M. Van Nesselrooij, L. L. M. Veldhuis, F. Schrijer, and B. Van Oudheusden. Flow visualization over drag reducing dimpled surfaces in turbulent boundary layers using particle image velocimetry. *18th International Symposium on the Application of Laser and Imaging Techniques to Fluid Mechanics*, 2016.

T. Van der Hoeven. *Slot Suction of the Turbulent Boundary Layer*. Thesis, Delft University of Technology, 2013.

M. Van Nesselrooij. *On the drag reduction of dimpled surfaces in turbulent boundary layers*. Thesis, Delft University of Technology, 2015.

E. Vervoort. *Drag effect of dented surfaces in turbulent flows*. Thesis, Delft University of Technology, 2007.

J. M. Wallace. Quadrant analysis in turbulence research: History and evolution. *Annu. Rev. Fluid Mech.*, 48:131–158, 2016.

B. L. Welch. The significance of the difference between two means when the population variances are unequal. *Biometrika*, 29(3/4):350–362, 1938. ISSN 00063444.

F. M. White. *Viscous Fluid Flow*. McGraw-Hill, third edition edition, 2006.

A. Yakeno, Y. Hasegawa, and N. Kasagi. Modification of quasi-streamwise vortical structure in a drag-reduced turbulent channel flow with spanwise wall oscillation. *Physics of Fluids*, 26(8):085109, 2014. ISSN 1070-6631 1089-7666. doi: 10.1063/1.4893903.

W. Zhou, Y. Rao, and H. Hu. An experimental investigation on the characteristics of turbulent boundary layer flows over a dimpled surface. *Journal of Fluids Engineering*, 138(2): 021204, 2016. ISSN 0098-2202.

Appendix A

Set-up pictures

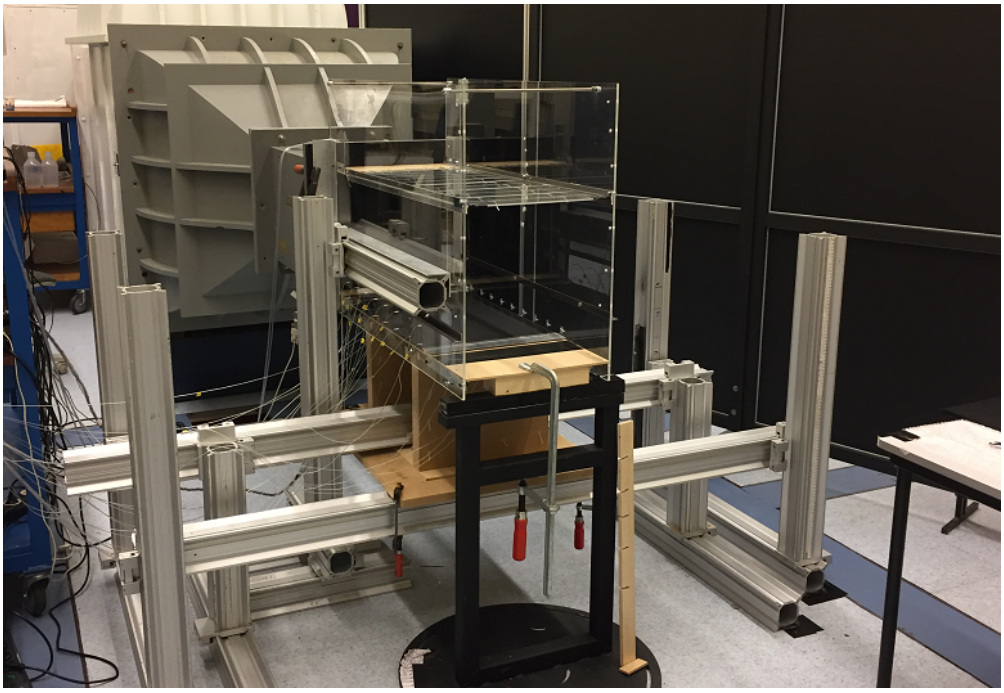

FIGURE A.1: Experimental set-up in ZPG configuration.

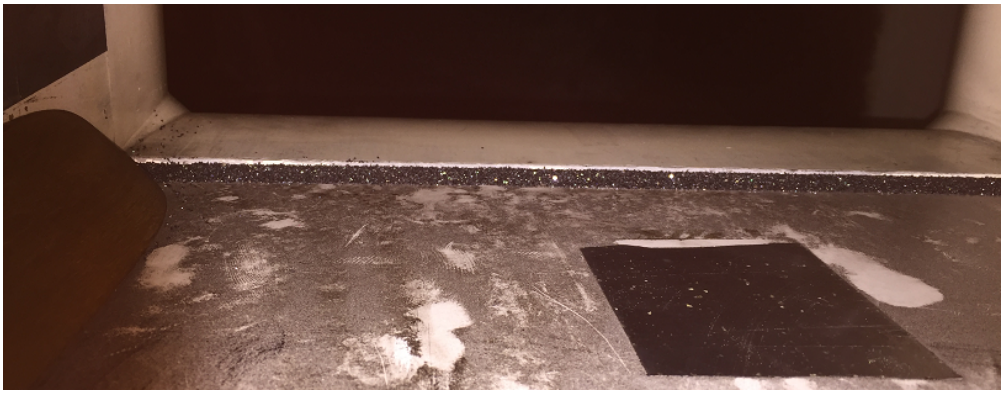

FIGURE A.2: Carborundum strip (width = 2 cm) at x = -975 mm just after the tunnel contraction to assure turbulent boundary layer.

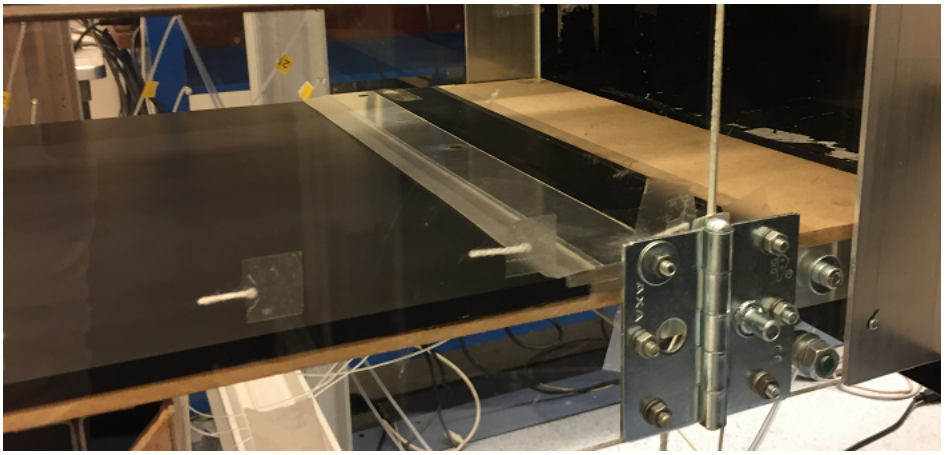

FIGURE A.3: Plastic strip between set-up and test plate to assure proper guidance of the boundary layer to the test plate.

FIGURE A.4: Tufts on each individual sliding plate contained inside the planar diffuser.

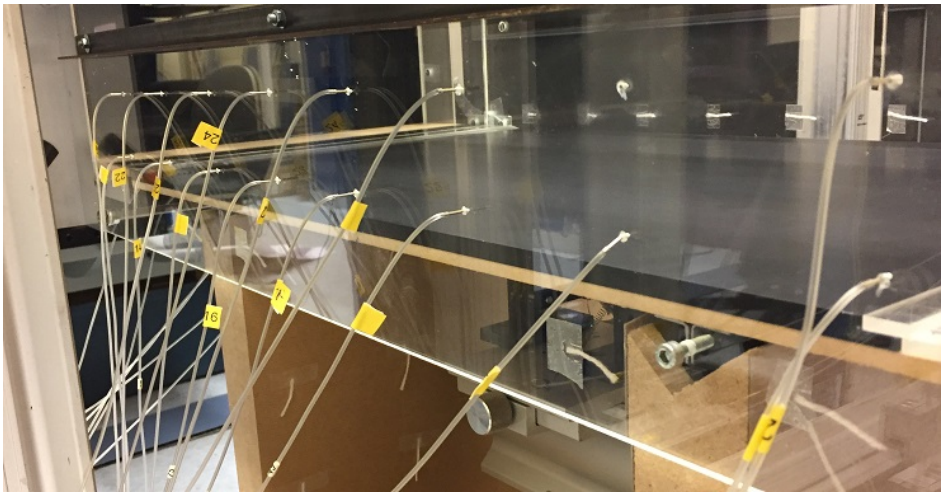

FIGURE A.5: Pressure taps on the rigid wall.

(A) Upstream. (B) Downstream.

FIGURE A.6: Spanwise pressure taps at the gaps between the test plate and the test section.

Appendix B

Experimental design

In this appendix the algorithm written for the first order estimate of the boundary layer development is explained. The structural loading of the flexure balance system and its design parameters are also discussed. The aerodynamic model is initialized from within MATLAB. An overview of the algorithm is given in B.1, and its components discussed in the subsequent sections.

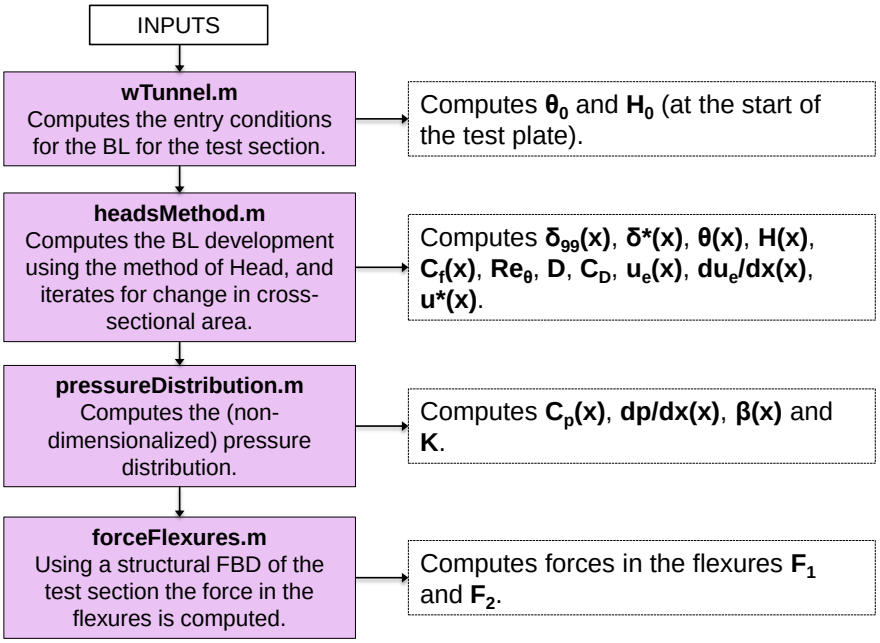

FIGURE B.1: MATLAB algorithm used to compute boundary layer development and structural properties.

B.1 Aerodynamic model

Intialization. Before computing any TBL development, some initial flow conditions that are specific for the flow problem at hand is required. In the aerodynamic model it is wanted to have some inlet conditions which are used to determine the development through the tunnel section. Luckily, Kuik (2007) performed a boundary layer study with the W-tunnel, nozzle size and extension. He placed a trip wire just after the nozzle contraction stops. The TBL was quantified at a distance somewhat behind the tunnel extension. Using the empirical boundary layer equations given in Equation B.1 the start of the boundary layer is estimated by taken the average of the three distances computed from the data of Kuik (2007). To compute the initial TBL properties for different upstream velocities U_∞ at the start of the considered flow domain this origin location is used. The inlet conditions are

computed within the `wTunnel.m` file.

$$\theta = \frac{0.037x}{\mathrm{Re}_x^{\frac{1}{5}}}, \qquad \delta_{99} = \frac{0.380x}{\mathrm{Re}_x^{\frac{1}{5}}}, \qquad \theta = \frac{0.048x}{\mathrm{Re}_x^{\frac{1}{5}}} \tag{B.1}$$

Boundary layer development. Under a pressure gradient the relations given in Equation B.1 are no longer valid, as they are defined for a ZPG. To this end the method of Head is utilized, as a velocity distribution is required due to the pressure gradient. The method of head consideres two ODEs which will be repeated from Section 2.1.2:

$$\frac{\mathrm{d}\theta}{\mathrm{d}x} = \frac{C_f}{2} - (2+H)\frac{\theta}{U_e}\frac{\mathrm{d}U_e}{\mathrm{d}x} \tag{B.2}$$

$$\frac{\mathrm{d}H_1}{\mathrm{d}x} = -H_1\left(\frac{1}{u_e}\frac{\mathrm{d}u_e}{\mathrm{d}x} + \frac{1}{\theta}\frac{\mathrm{d}\theta}{\mathrm{d}x}\right) + \frac{0.0306}{\theta}\left(H_1 - 3\right)^{-0.6169} \tag{B.3}$$

Equation B.2 is the Von Karman integral relation, in which the velocity gradient is intrinsically captured. The second relation in Equation B.3 is defined by Head (1960). Only two boundary conditions are required, H_1 and θ, which are supplied by `wTunnel.m` file. Additional closure relations are need, which were defined in Section 2.1.2. The velocity distribution and its derivative are still required. For a one dimensional incrompressible flow problem the conservation of mass between two stations in a channel can be given as:

$$U(x)A(x) = U_0 A_0 \tag{B.4}$$

where Figure 3.2 can be used as a reference. Since the plain diffuser has a simple geometry depending on the deflection angle φ, the conservation can be conveniently rewritten to determine the velocity distribution when the inlet velocity U_0 and φ are known:

$$U(x) = \frac{U_0 D_0}{D_0 - x\tan\varphi - 2\times\delta_{99}(x)} \tag{B.5}$$

where D_0 is the initial channel height, in this case for the W-tunnel 0.4 m. Note that the boundary layer thickness is included twice in Equation B.5, as the boundary layer changes the effective change of the channel (on the top and bottom of the section). For the initial calculation of the boundary layer (the first iteration) a zero-valued boundary layer thickness is used. With the velocity distribution now known, it can be used in the method of Head (1960). In the algorithm `headsMethod.m` the only variable inputs are thus the upstream velocity U_0, diffuser angle φ and the ambient temperature T_0, together with the TBL boundary condition inputs from the initialization.

A numerical ODE solver is used as to solve the equations, in this case MATLAB's `ode45` solver. After four iterations in which the velocity is updated for the boundary layer thickness a converged solution is observed. The outputs are then θ(x) and H_1(x), which can then be used with the closure relations to compute the required boundary layer properties. With the iterated velocity distribution known the pressure parameters can also be calculated, which is done subsequently in `pressureDistribution.m`.

B.2 Structural model

Load calculation. With all of the aerodynamic forces known, these can then be used in the design of the flexure drag balance. The pressure gradient p(x) induces an effective resultant force F_{res} on the test plate with an arm $\mathrm{x_r es}$. Next to the pressure force there is also the weight

of the test plate that acts on the flexures. In the streamwise direction only the aerodynamic drag force is present, which results from an integration of the skin-friction over the plate surface. With all these forces known static equilibrium can be used to calculate the effective force in the flexures. In Figure B.2 all the forces and their associated distances are given. The two distances s_1 and s_2 indicate the distance at which the flexures are placed compared to the leading edge of the test plate. Equilibrium of horizontal forces, vertical forces and moments is then given by Equation B.6:

$$\begin{bmatrix} 1 & 1 & 0 \\ 0 & 0 & -1 \\ s_1 & s_2 & L_f \end{bmatrix} \begin{pmatrix} F_1 \\ F_2 \\ F_{\text{meas}} \end{pmatrix} = \begin{pmatrix} F_{res} + W \\ -D \\ (L_f + t)D + x_{\text{cg}}W + x_{\text{res}}F_{\text{res}} \end{pmatrix} \tag{B.6}$$

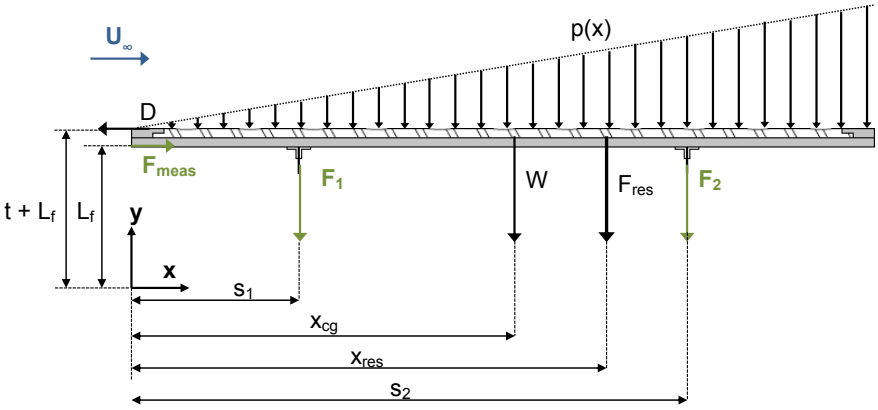

FIGURE B.2: Free body diagram of force acting on the plate.

This matrix relation can then be solved for different inputs of pressure gradient, drag force and flexure spacing, yielding the resultant force in the flexures, which is done in `forceFlexures.m`. After several user iterations as well as the flexure dimensions, a result is wanted in which the flexure efficiency is high whereas the flexures do not buckle due to the gravity and pressure forces.

Appendix C

Wind-tunnel RPM settings

Before starting the DFM campaign the velocities measured through the pitot tube are correlated to the required RPM. The values are tabulated in Table C.1.

TABLE C.1: W-tunnel required fan settings for specific free-stream velocity.

VELOCITY (m/s)	ZPG (RPM)	SFPG (RPM)	SAPG (RPM)	MAPG (RPM)	MFPG (RPM)
10	311	391	298	305	332
12	367	464	349	358	392
14	422	537	400	411	452
16	478	610	452	464	512
18	533	683	503	517	572
20	589	756	554	570	631
22	644	829	605	623	691
24	700	902	657	676	751
26	755	975	708	729	811
28	811	-	759	782	871
30	866	-	810	835	931
32	921	-	862	888	990
34	977	-	913	941	-
36	-	-	964	994	-

Appendix D

DFM checklist

TABLE D.1: Checklist for the DFM campaign, for the ZPG case.

CONSIDERED CASE:	DATE:		TIME:			
Task	**Check**	**Actual time**	**Measurements**			
Set stopwatch		**0:00**	No.	Velocity	Start	Check
Open door			1	0 (1)	33:30:00	
Insert upper wall support			2	0 (2)	34:00:00	
Remove plate			3	0 (3)	34:30:00	
Insert plate			4	0 (4)	35:00:00	
Close door			5	0 (5)	35:30:00	
Remove pin		**0:25**	6	10	36:00:00	
Update file names			7	12	36:30:00	
Temperature sensor active?			8	14	37:00:00	
Pressure sensor active?			9	16	37:30:00	
Force sensor active?			10	18	38:00:00	
Note total pressure p_{tot}			11	20	38:30:00	
Check if plate is aligned			12	22	39:00:00	
Reset delta on (all) Mensor(s)			13	24	39:30:00	
Start measuring		**0:33**	14	26	40:00:00	
Note time in logbook			15	28	40:30:00	
Adjust speed lever to initial RPM			16	30	41:00:00	
Full RUN (10-30 m/s with 2 m/s increment)		**0:35:40**	17	32	41:30:00	
End of full RUN		**0:47:10**	18	34	42:00:00	
Check if plate is aligned			19	0 (1)	42:30:00	
Check flexures			20	0 (2)	43:00:00	
Insert pin		**0:55**	21	0 (3)	43:30:00	
			22	0 (4)	44:00:00	
			23	0 (5)	44:30:00	
			24	0 (6)	45:00:00	
			25	0 (7)	45:30:00	

Appendix E

Statistical significance

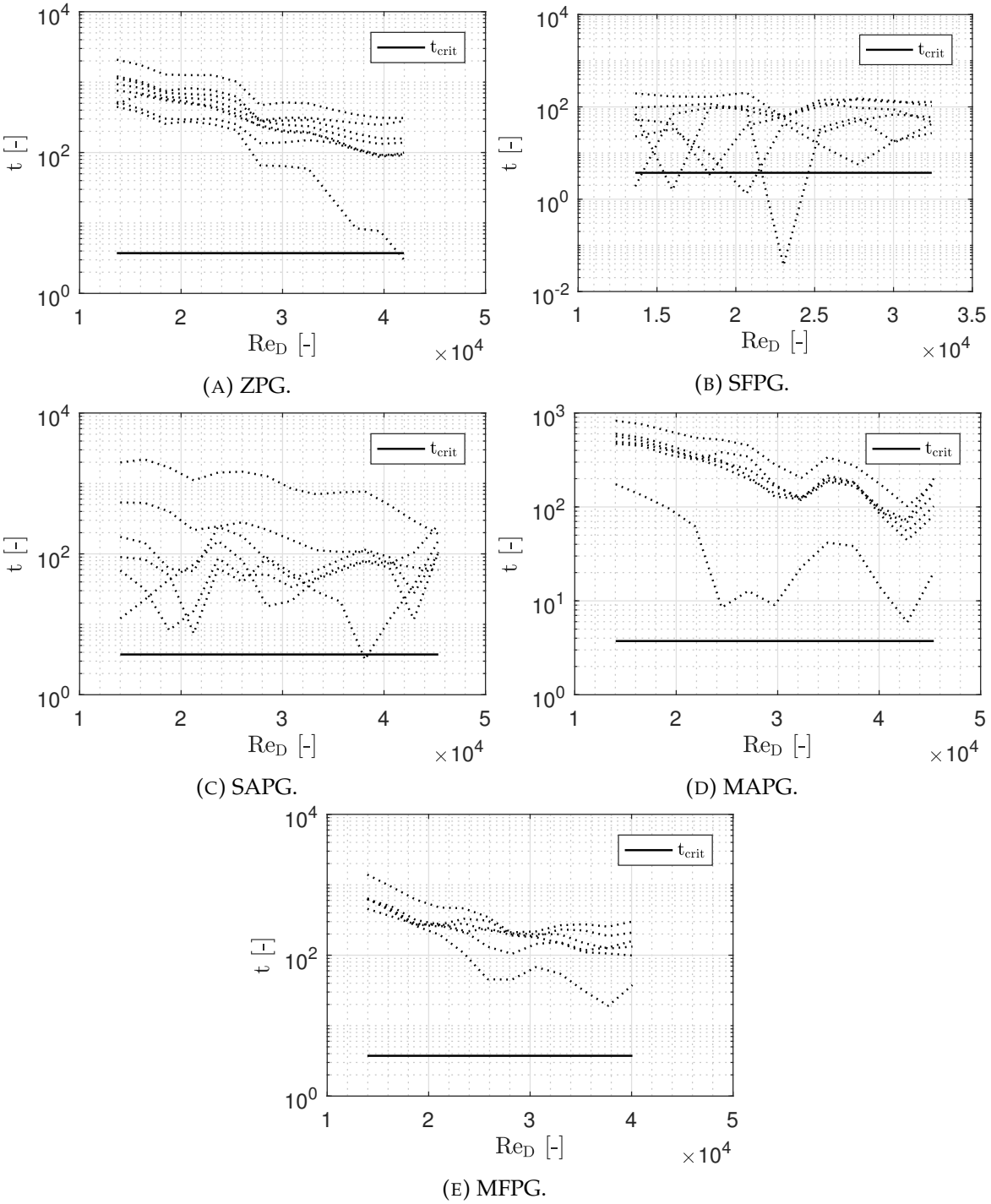

(A) ZPG.

(B) SFPG.

(C) SAPG.

(D) MAPG.

(E) MFPG.

FIGURE E.1: Statistical t-values computed for the DFM campaign.

Appendix F

Forces after corrections

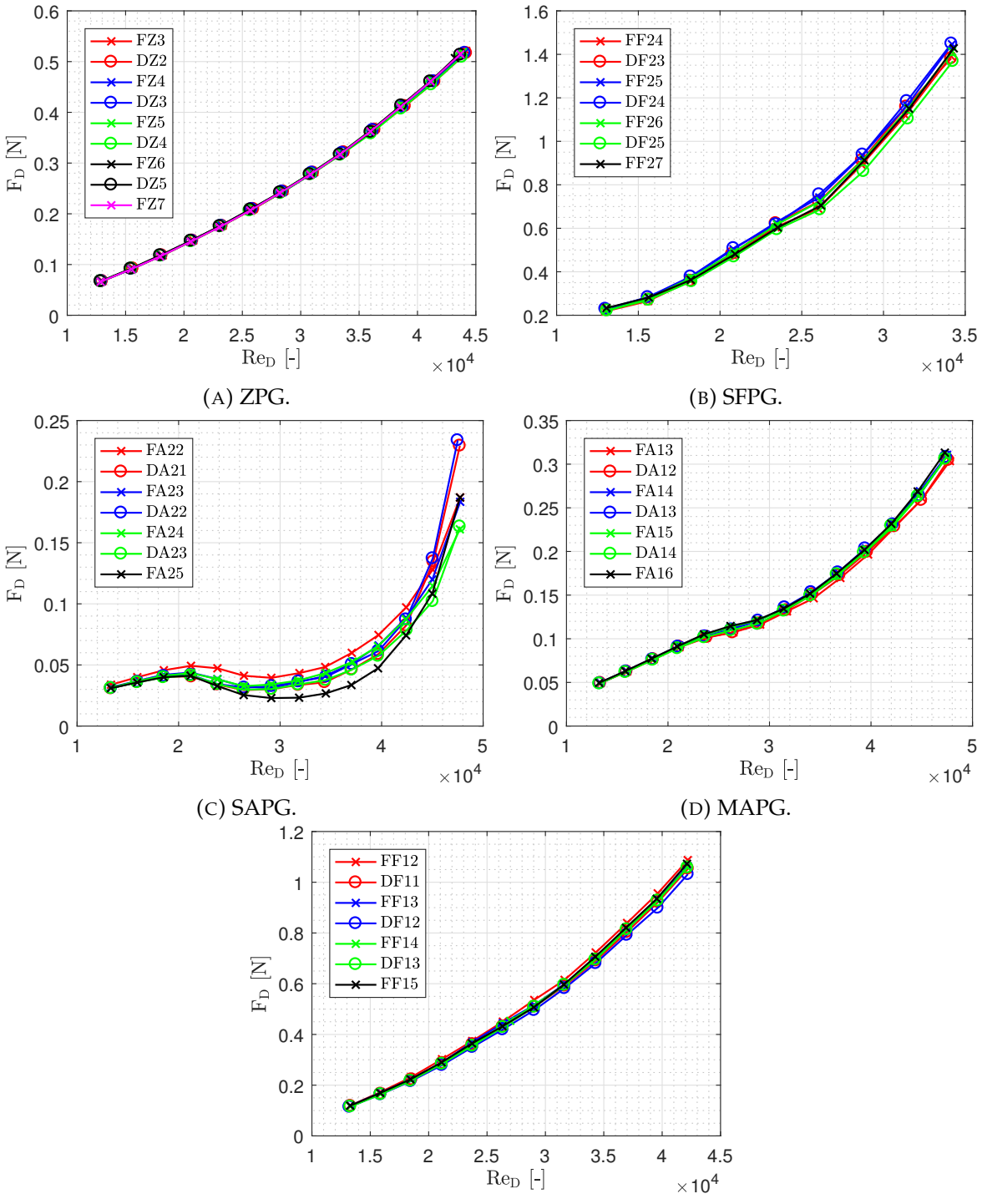

(A) ZPG.

(B) SFPG.

(C) SAPG.

(D) MAPG.

(E) MFPG.

FIGURE F.1: Corrected force signals measured during the DFM campaign.